Raman spectroscopy methods for investigating supported lipid bilayers

Claire Sue Sweetenham, MPhys (Hons)

Thesis submitted to the University of Nottingham
for the degree of Doctor of Philosophy

June 2011

Abstract

This work is centred on the development of Raman spectroscopy methods for investigating supported lipid bilayers (SLBs). These nanoscale, biological structures have found wide application as models of cellular membranes in many areas of scientific research. They consist of phospholipid molecules that self-organise into bilayer structures containing phase-separated microdomains, which play an important role in many biological processes. SLBs are well-defined and stable under a variety of conditions, allowing characterisation with a broad range of physical methods. However, many of these techniques provide purely a visualisation of the surface or disturb the bilayer with labelling. Raman spectroscopy can offer a non-invasive chemical and structural analysis of SLBs and microdomains.

A Raman microspectroscopy (RMS) system with integrated atomic force microscope (AFM) has been developed and characterised for studying SLBs. This experimental setup combines the benefits of Raman spectroscopy with the high spatial resolution of confocal microscopy. Furthermore, the incorporation of AFM makes it possible to directly correlate chemical information and spatial features. Experiments are carried out to determine the capabilities of this system for investigating SLBs. A variety of substrates are considered for this application and only prolonged expose to high laser powers is found to have any effect on the Raman spectrum of lipids. However, a single SLB cannot be detected with RMS, so focus turns to employing scattering-enhancing techniques. Surface-enhanced Raman spectroscopy (SERS) substrates formed by nanosphere lithography (NSL) are developed to be used with the combined AFM-Raman system. Simultaneous topographical imaging and high-sensitivity chemical mapping of molecular monolayers deposited across these substrates reveals the distribution and magnitude of electric field enhancement that they can provide. These measurements are supported by calculations and finite element method (FEM) simulations. Then similar experiments are performed on substrates covered with a bilayer of fatty acid molecules. Considering the close similarities between these molecules and phospholipids, this demonstrates the potential of combined AFM and SERS with NSL substrates for detecting SLBs and imaging the phase-separated microdomains they form. Finally, functionalised AFM

probes are developed for tip-enhanced Raman spectroscopy (TERS) using dielectrophoresis (DEP). This phenomenon is generated within a conductive AFM setup to guide nanoparticles towards an AFM probe to cluster and grow at its tip apex. This growth is monitored with force spectroscopy and a variety of imaging parameters. The probes are then analysed with scanning electron microscopy (SEM) and energy-dispersive x-ray spectroscopy (EDX) to confirm the accumulation of nanoparticles on the tip both physically and chemically. The TERS activity of these functionalised probes is investigated with the combined AFM-Raman system, which demonstrates an enhancement of scattering when the tip apex of the probe and the laser are aligned.

List of publications

C. S. Sweetenham and I. Notingher, **Raman spectroscopy methods for detecting and imaging supported lipid bilayers**, *Spectroscopy* **2010**, *24* (1-2), 113-117.

C. S. Sweetenham and I. Notingher, **Combined AFM-Raman mapping of electric field enhancement and SERS hot-spots for nanosphere lithography substrates**, *J. Nanophoton.* **2011**, *5*, 059504.

C. S. Sweetenham, M. Larraona-Puy and I. Notingher, **Simultaneous SERS and AFM for label-free physicochemical analysis of lipid bilayers**, *Appl. Spectrosc.* (submitted).

List of abbreviations and acronyms

2D	two-dimensional
3D	three-dimensional
AA	arachidic acid
AFM	atomic force microscopy
CARS	coherent anti-Stokes Raman spectroscopy
CCD	charge-coupled device
DEP	dielectrophoresis
DLA	diffusion-limited aggregation
DOPC	dioleoylphosphatidylcholine
DPPC	dipalmitoylphosphatidylcholine
EDX	energy-dispersive x-ray spectroscopy
FEM	finite element method
FFT	fast Fourier transform
FWHM	full width at half maximum
H_2O_2	hydrogen peroxide
H_2SO_4	sulphuric acid
HOMO	highest occupied molecular orbital
LB	Langmuir-Blodgett
LUMO	lowest unoccupied molecular orbital
$MgCl_2$	magnesium chloride
MgF_2	magnesium fluoride
NMR	nuclear magnetic resonance
NSL	nanosphere lithography
p-ATP	p-aminothiophenol
PCA	principal component analysis
PML	perfectly matched layers
PSF	point spread function
R6G	rhodamine 6G
RMS	Raman microspectroscopy
SEM	scanning electron microscopy
SERS	surface-enhanced Raman spectroscopy
SLB	supported lipid bilayer
SPM	scanning probe microscopy
STM	scanning tunnelling microscopy
SVD	singular value decomposition
TEM	tunnelling electron microscopy
TERS	tip-enhanced Raman spectroscopy
TIR	total internal reflection

List of nomenclature with units

A	area (m^2)
A_M	area of metallic surface (m^2)
a_{SL}	in-plane particle diameter (m)
c	speed of light (ms^{-1})
c_{RS}	concentration of neat solution (M)
D	minimum laser spot diameter (m)
D_0	diameter of laser beam (m)
d	diameter of objective back aperture (m)
$d_{ip,SL}$	interparticle spacing of nanostructures (m)
d_m	thickness of metal deposition (m)
$d_{x,y}$	lateral resolution (m)
d_z	axial resolution (m)
$\boldsymbol{E}$	electric field strength (Vm^{-1})
$\boldsymbol{E_0}$	vibrational amplitude of electric field (Vm^{-1})
E_0	incident electric field (Vm^{-1})
E_{local}	internal electric field (Vm^{-1})
E_{total}	total electric field (Vm^{-1})
∇E	electric field gradient (Vm^{-2})
EF	enhancement factor
e	exposure (Jm^{-2})
F'	force gradient (Nm^{-1})
F_{DEP}	DEP force (N)
f	focal length (m)
f_l	lens focal length (m)
f_{obj}	objective focal length (m)
$f/\#$	f-number
G	étendue (m^2)
$\boldsymbol{H}$	magnetic field strength (Am^{-1})
H_0	incident magnetic field (Am^{-1})
H_{eff}	effective height of scattering volume (m)
h	Planck's constant (Js)
I_0	incident radiation intensity (counts)
I_{RS}	Raman scattering intensity (counts)
I_{SERS}	SERS scattering intensity (counts)
K	proportionality constant
k	spring constant (Nm^{-1})
L	characteristic length scale (m)
M	magnification
m	effective mass (kg)
NA	numerical aperture
$\boldsymbol{n}$	interfacial normal vector

n	refractive index
$\boldsymbol{P}$	electric dipole moment (Cm)
P	laser power (W)
q	nuclear displacement (V)
q_0	vibrational amplitude (V)
r	distance (m)
t	time (s)
V	applied potential (V)
α	polarisability (Cm^2V^{-1})
α_0	polarisability at equilibrium (Cm^2V^{-1})
ΔE	energy (J)
$\Delta\omega$	resonant frequency shift (kHz)
ε	permittivity (Fm^{-1})
ε_0	permittivity of free space (Fm^{-1})
ε_m	permittivity of suspension medium (Fm^{-1})
ε_p	permittivity of particle (Fm^{-1})
θ	angular aperture
λ	wavelength (m)
λ_0	laser wavelength (nm)
λ_R	Raman scattering wavelength (nm)
μ	permeability (NA^{-2})
μ_M	surface density of nanostructures (nm^{-2})
μ_S	surface density of molecules (nm^{-2})
ν	frequency of light (Hz)
ν_0	frequency of incident light (Hz)
$\tilde{\nu}$	Raman shift (cm^{-1})
Ω	solid angle
ω_0	resonant frequency (kHz)

Acknowledgements

There are so many people who have contributed in some way to the work in this thesis either academically, socially or emotionally. Firstly, thanks must go to my supervisor Dr Ioan Notingher for his expertise and guidance throughout my PhD and to my co-supervisor Prof Philip Moriarty for the times I needed a second opinion. Thanks also to our little Raman group, especially Alina who was with me from the beginning and Marta who helped me out at the end.

The development of the experimental setup was an integral part of my studies and would not have been possible without the guys in the Workshop, so thanks must go to them for all the random but wonderful things they made me for the lab. Thanks to Matthew Brownhill for his help with making the lipid samples in the early days and to Dr Richard Woolley for the mini-postdoc and his enthusiasm for my work in the last year. Also a special thank you to Penny, Chris and the 'physics buskers' for their support through all my outreach endeavours.

I would not have survived my PhD without the coffee breaks, lunchtimes and Friday night pub trips, so thanks to Alex, Pete, Adam, Luis, Andy, James, Kevin, Julian, Nick and the rest of the Nanoscience group for these highlights. Thanks also to my squash buddy Kate, Ruth and Neil, Maria and all my other friends outside the walls of the School of Physics and Astronomy.

Finally, a special acknowledgement to my Mum, Dad, sister Emma and brother David. There is no way I would be where I am today without their continued love and support, so thanks to them for everything. Thank you to my Nanny and Grandad for their encouragement over the years. And also many thanks to Matt, who always believed in me and has helped me to achieve this PhD in too many ways to mention.

“I’ve started, so I’ll finish.”

Magnus Magnusson

Contents

Chapter 1

Introduction

Throughout the biological world, a hydrophobic film just a few nanometres thick serves as the margin between life and death for individual living cells. This film, or membrane, consists of a double layer of lipids, known as a phospholipid bilayer, that separates and protects the cell from its surrounding environment [1]. Lipids are hydrocarbon-containing organic compounds of which there are two types, saturated and unsaturated. When combined in a bilayer, these different types of lipids organise themselves into phase-separated areas known as microdomains [2]. These regions play a central role in the workings of a cell membrane; they feature in many biological processes, have been associated with membrane proteins and are possible entry points for toxins [3, 4]. It is therefore of great interest to study the properties of different lipids and learn more about the microdomains they form.

Supported lipid bilayers (SLBs) provide a biologically relevant model for cell membranes. The ability to manipulate and modify the makeup and environment of these lipid structures enables a fair representation of the cellular system being depicted. Over the past two decades SLBs have become a 'hot topic' for scientific research and have been studied with a wide variety of microscopy and spectroscopy methods. However, despite recent advances, the physical and chemical properties of lipid bilayers and microdomains are still poorly understood [5].

Investigating SLBs

One of the foremost techniques used for sample characterisation in a range of research fields is atomic force microscopy (AFM), which measures atomic forces between a probe and surface to provide high-resolution images and mechanical information at the nanoscale. AFM has been used extensively to analyse lipid bilayers [6]. It has been used to visualise the formation of SLBs from vesicles [7] and study their structure and stability [8], mechanical [9-11] and electrical properties [12]. AFM has been used to monitor the inclusion of biomolecules and proteins [13] and the effect of external agents [14]. A number of studies have also focused on the occurrence of microdomains [15]. Electron microscopy techniques such as scanning electron microscopy (SEM) and tunnelling electron microscopy (TEM) have also been used to image SLBs [16], often combined with other methods such as AFM [17]. However, these microscopy techniques offer no chemical specificity. On the other hand, mass spectrometry has been employed to analyse the chemical composition of lipid bilayers [18, 19], but this requires invasive procedures. Nuclear magnetic resonance (NMR) spectroscopy is often used to investigate the structure of lipid bilayers and also their interaction with proteins [20]. However, this is only possible with vesicles in solution, not planar bilayers, which makes it difficult to discriminate microdomains from the rest of the membrane. Similar studies have been performed with x-ray diffraction and neutron scattering [21].

Fluorescence microscopy is an optical technique that has the ability to delve deeper into the chemical structure of an SLB and provide micrometre spatial resolution [22, 23]. It has been used to study the interaction of proteins and other biomolecules within a lipid bilayer [24] and the movement of charged components across the structure [25]. The technique has also been combined with AFM to investigate the growth, shape and topology of microdomains [26]. However, fluorescence microscopy requires labelling that may disturb the structure of the bilayers and there is a limited availability of fluorescent labels such as those for cholesterol, which is an important component of cell membranes.

Raman spectroscopy studies

Raman spectroscopy is a well-established, analytical technique with great potential for studying SLBs. This optical method relies on the inelastic scattering of monochromatic light from a material, measured as an energy or frequency shift [27]. A collection of these shifts, known as a spectrum, generates a physiochemical fingerprint of a given sample, providing detailed information at the molecular level [28]. Its ability to take non-invasive, real-time measurements with little restriction on sample preparation or environment has meant that it has become a powerful tool in biophysical and medical research. Much of the work in these fields has focused on detecting the biomolecules within a cell such as proteins, peptides and nucleic acids. However, Raman spectroscopy also has the potential to provide both chemical specificity and imaging through variations and modifications of the technique. Furthermore, in recent years, the emergence of derivative methods such as coherent anti-Stokes Raman spectroscopy (CARS), surface-enhanced Raman spectroscopy (SERS) and tip-enhanced Raman spectroscopy (TERS) has provided the sensitivity and spatial resolution to investigate lipid membranes and microdomains.

Non-resonant Raman spectroscopy has been successfully used to determine the structure and chemical makeup of many different types of lipid molecules, including isomer composition [29, 30], degree of unsaturation [31] and chain length [32]. Much of this early work originates from studying lipids for the characterisation of fats and oils [33]. Today, the interpretation of certain Raman bands of lipids is still under discussion [34]. Spectral features such as Raman frequencies, peak intensities, band shapes and splittings can provide information on the isomerisation, reorientation, acyl chain interactions and phase transitions of lipid bilayers [35]. In addition, lipids have been investigated under varying physical conditions such as pressure and temperature [36, 37].

There have been a number of Raman spectroscopy studies on bilayers in single lipid vesicles, or liposomes. Most of these have been possible with a technique known as optical-trapping, in which the sample is physically held and moved in the beam of a highly focused laser [38, 39]. The bilayer itself was detected in these studies, as well as molecular species contained within the vesicle and the movement of toxins

through the membrane. Additionally, measurements have been taken of lipid bilayers in large unilamellar and multilamellar vesicles, again investigating phase transitions and coexistence of lipids [40, 41]. However, optical-trapping is not suitable for imaging microdomains, since chemical mapping is not possible with suspensions. Furthermore, these experiments have limited spatial resolution, providing only bulk spectroscopic data averaged over many lipid molecules.

The spatial resolution of a typical Raman spectroscopy setup is diffraction limited and is insufficient to study processes that occur at a scale below 100nm, such as the formation and diffusion of cellular membrane microdomains. Also, the nanoscale thickness and weak Raman scattering of a single SLB can make it difficult to discriminate the corresponding signal from the Raman background. This background scattering is produced by other biological molecules that may be present in the model or the substrate supporting the lipid structure. The development of Raman microspectroscopy (RMS) is one way of improving the spatial resolution offered by the conventional method [42], which allows the collection of scattered light from sample volumes of less than 1μm in diameter. This level of spatial resolution may be achieved by setting up a confocal system, whereby any scattered light collected from a sample and the surrounding area is directed through a pinhole that rejects any out-of-focus signal.

A small amount of work has been performed to observe SLB microdomains with the addition of a confocal system [43]. Similar studies have also been possible with a total internal reflection (TIR) geometry [44]. The combination of optical-trapping and RMS has enabled the detection of many lipid features including lipid phase transitions as a function of temperature [45]. These methods have also been used to investigate drug-membrane interactions [46]. However, without a significant enhancement of scattering, these measurements are restricted to the C–H stretching region of the spectrum where scattering is stronger but there is limited chemical contrast between different lipids [47]. CARS is a Raman spectroscopy method that has the capabilities to image biological samples alongside revealing their chemical makeup [48]. Its potential for label-free imaging of lipid microdomains in single SLB has been demonstrated [49, 50]. The technique has also been used to study the ordered orientation of water at the surface of a lipid bilayer [51]. However, the

spectral resolution of CARS is lower than conventional Raman spectroscopy and other related techniques, particularly in the fingerprint spectral region, making it difficult to reliably identify phase-separated microdomains [52, 53].

SERS and TERS

One variation of Raman spectroscopy that has been shown to provide the sensitivity and both the spatial and spectral resolution required for imaging lipid microdomains is SERS. SERS benefits from increased sensitivity by exploiting the enhancement of scattering close to rough, metallic surfaces [54, 55]. The effect arises from localised surface plasmon resonances that produce increasingly enhanced electric fields between a sample and metal nanostructures. In most cases, the technique has investigated so-called hybrid bilayers; these bilayers contain a lipid monolayer tethered to a metal substrate [56, 57], electrode [58], microprobe [59] or nanoshell [60] by a self-assembled monolayer of alkanethiols. Standard SLBs have been detected on SERS substrates combined with techniques such as resonance Raman [61, 62] and TIR [63]. These studies have revealed chemical composition, phase transitions, the ordering and orientation of lipids and the interaction of various biomolecules with model membranes. However, they have not attempted to chemically image lipid microdomains.

For this to be possible, the Raman spectroscopy setup must include an AFM to identify and confirm the location of the SLB and microdomains [64]. The combination of SERS and AFM has the potential to topographically, mechanically and chemically investigate SLBs. However, there are several further aspects of the setup to be considered. Most notably, it requires an inverted configuration with transparent substrates. These substrates must also have a roughness that is compatible with both supporting an SLB and activating enhancement that is high, consistent and uniform enough to detect spatially resolved chemical features such as lipids in a microdomain. In addition, it has long been debated whether the high temperatures that arise from the electric field enhancement responsible for the SERS effect risk damaging biological materials [65]. This is a prevalent concern and it is under discussion as to whether these raised temperatures are caused by resonance effects or laser heating. The matter has been explored by measuring anti-

Stokes/Stokes ratios [66] and cross-correlation of spectral parameters such as Raman band position, width and intensity [67]. Furthermore, it has been demonstrated that this localised heating can cause irreversible loss of SERS intensity [68].

A closely related technique to SERS is TERS [69], which uses a sharp metal tip such as a scanning probe microscopy (SPM) probe to enhance the Raman scattering from a sample rather than an underlying metallic surface [70]. As with the combination of SERS and AFM this technique allows simultaneous topographical and spectroscopic measurements, making it possible to directly correlate chemical information and spatial features [71]. TERS holds a great deal of promise for imaging biological structures such as SLBs. However, it has similar challenges to SERS, such as substrate dependence and localised heating [72].

The main aim of the work in this thesis is to detect and image a single SLB with Raman spectroscopy methods and correlate this with AFM measurements to provide a more detailed study of model cell membranes and microdomains than is currently achievable. Past research in this field has focused on studying SLBs either physically or chemically, but not both, or has detected lipid bilayers in vesicle form. Many of the current techniques for investigating SLBs risk disturbing the structure of the material or provide limited spatial or spectral resolution. Developing a combined microscopy and spectroscopy system to chemically image SLBs and their microdomains is a huge challenge. However, this work will provide scientists with a better understanding of membrane structure and function and aid investigation into important fields of medical research such as cell toxicology and drug delivery.

Thesis outline

This thesis presents the development of Raman spectroscopy methods for studying SLBs and microdomains. This work centres on a purpose-built confocal RMS system that is capable of SERS and TERS studies. When combined with AFM, these methods show great potential for providing label-free physiochemical imaging of SLBs, which is not possible with current techniques used to investigate these biological structures.

Chapter Two: In this chapter, the theory and significance of modelling cell membranes is described. This includes a discussion of the properties of phospholipids, the formation of a lipid bilayer and the occurrence of phase-separated microdomains. Also, the main techniques used to create SLBs are outlined.

Chapter Three: A description of AFM is given here, which is the surface characterisation technique used in this work. Its development is detailed, as well as the main principles, imaging modes and applications of the instrument. Particular attention is paid to the use of AFM to study biological materials in liquid.

Chapter Four: This chapter outlines the Raman spectroscopy methods employed in these studies. The background and theory of non-resonant Raman spectroscopy, SERS and TERS is described as well as the relevance of these techniques to the investigation of SLBs.

Chapter Five: The development and characterisation of an RMS setup with integrated AFM for studying SLBs is described here, which combines the benefits of Raman spectroscopy with the high spatial resolution of confocal microscopy and capabilities of AFM. All aspects of the design, purchase, alignment, calibration and optimisation of this system are detailed. This includes an assessment of its spatial resolution and how the axial resolution of the setup can be improved by the inclusion of a confocal system.

Chapter Six: In this chapter, the combination of AFM and Raman spectroscopy for investigating SLBs is discussed. Experiments are carried out to assess a variety of substrates for their suitability for both AFM and Raman spectroscopy studies. The compatibility of the substrate for supporting a single SLB must also be considered. The effect, if any, of laser power and exposure on lipids is addressed. Finally, SLBs are measured and characterised with AFM and the RMS system.

Chapter Seven: Progress towards studying an SLB with SERS is reported here. A key part of this work is the development of suitable SERS-active substrates to combine with the AFM-Raman system. NSL substrates are characterised and optimised for providing both the level of enhancement required to detect an SLB and

the uniformity of SERS signal necessary to chemically image phase-separated microdomains. SERS spectra and mappings are analysed for various molecular monolayers and a fatty acid bilayer. Supported by calculations and modelling, these experiments demonstrate the potential of the experimental setup for label-free imaging of phospholipid SLBs.

Chapter Eight: This chapter describes the development of functionalised probes for TERS. The phenomenon DEP is generated within a conductive AFM setup to grow clusters of gold nanoparticles at the tip apex of AFM probes. This growth is monitored with force spectroscopy, topographical imaging and related parameters and then analysed further with SEM and EDX. Finally, the TERS activity of these probes is explored with chemical mappings performed on the combined AFM-Raman system.

Chapter Nine: Discussions of all the main results of the thesis are given here along with suggestions for the future directions of the research.

Chapter 2

Supported lipid bilayers

In this chapter, the theory and significance of modelling cell membranes is described. This includes a discussion of the properties of phospholipids, the formation of a lipid bilayer and the occurrence of phase-separated microdomains. Also, the main techniques used to create SLBs are outlined.

2.1 The living cell, phospholipids and microdomains

All living cells are surrounded by a membrane that physically separates the interior components of the cell from its environment (Figure 2.1). It acts as a protective barrier that is selectively-permeable to ions and certain organic molecules, controlling the movement of substances in and out of the cell. Cell membranes consist of numerous biological molecules that are involved in a variety of cellular processes such as cell adhesion, ion conductivity and cell signalling. These molecules diffuse more or less freely in a high fluidity system, known as the liquid-mosaic model [1].

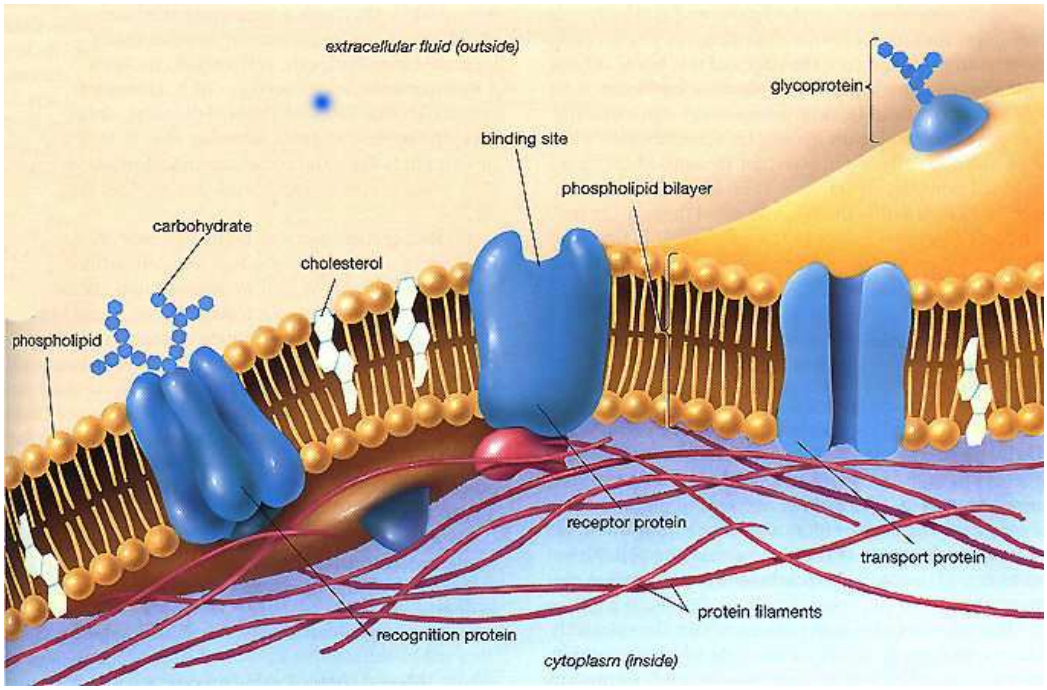

Figure 2.1: Cell membrane [73].

The main structure of a cell membrane is made up of globular molecules such as proteins that are partially embedded in a bilayer of phospholipids. Phospholipids are a type of lipid molecule. Lipids are organic compounds that consist of a 'tail' of long fatty acid hydrocarbon chains and a carboxyl 'head'. In the case of phospholipids, the 'head' contains a negatively-charged phosphate group making it highly polar and hydrophilic. Conversely, the 'tail' is very hydrophobic. Therefore when placed in water, phospholipids spontaneously arrange to point their 'tails' inwards towards each other and their 'heads' outwards towards the water, forming a membrane. In cellular membranes this takes the shape of a bilayer; however, lipids can group together to form a variety of structures depending on their concentration, chemical structure and experimental conditions (Figure 2.2):

(a) Monolayer – a single layer film of lipids at an air-water interface formed by compression in a Langmuir-Blodgett (LB) trough;
(b) Micelle – a colloid of lipids in an aqueous suspension that is hydrophilic on the outside and hydrophobic on the inside;
(c) Bilayer – the natural, energetically-favoured form that lipids take in an aqueous environment;
(d) Liposome, or vesicle – the spherical form of a bilayer with an aqueous core.

Forces such as van der Waals and electrostatic, hydrogen bonds and non-covalent interactions all contribute to the formation of a lipid bilayer. However, hydrophobic interactions are the major driving force in this process. The assembly of a lipid bilayer under these interactions gives the cellular membrane its protective nature. The arrangement of hydrophilic 'heads' and hydrophobic 'tails' in a lipid bilayer means that it has very low permeability for ions and most polar molecules. It prevents many polar solutes such as amino acids, nucleic acids, carbohydrates, proteins and ions from diffusing across the membrane, whilst allowing the passive diffusion of small hydrophobic molecules. This gives the cell the ability to regulate the movement of these substances via transmembrane protein complexes such as pores and gates; the fluidity of the bilayer means that these structures are free to move about laterally.

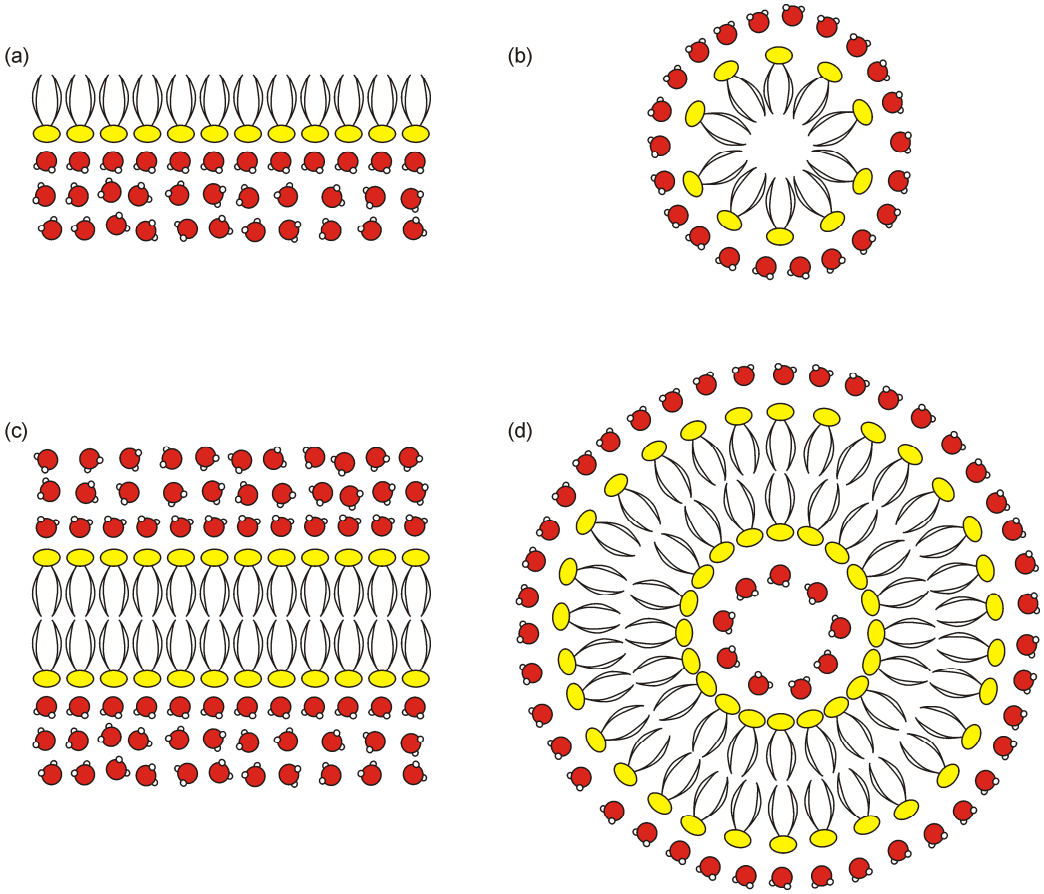

Figure 2.2: Different arrangements that phospholipids can form, showing positions of lipid molecules and water molecules (a) Monolayer (b) Micelle (c) Bilayer (d) Liposome, or vesicle (not to scale).

Phospholipids can be saturated or unsaturated, distinguishable by the absence or presence respectively of a carbon-carbon double bond within their 'tail' (Figure 2.3).

This difference in saturation can cause variations in the thermodynamic properties of lipids that are otherwise structurally and chemically identical. One property that differs greatly between saturated and unsaturated phospholipids is their phase transition temperature [74]. This temperature is the point at which a molecule moves from one phase to another; in the case of lipids this is the transition from being in a gel state to a liquid-crystalline state. In general, unsaturated phospholipids tend to have a much lower phase transition temperature than saturated phospholipids. This is due to the disorder that arises from the presence of a carbon-carbon double bond in the molecule; the repulsion of electrons within the bond causes the hydrogen atoms to move outwards and produces a kink in the lipid 'tail'. The level of this disorder and consequently the temperature at which an unsaturated phospholipid changes phase depends on the number and position of these carbon-carbon double bonds.

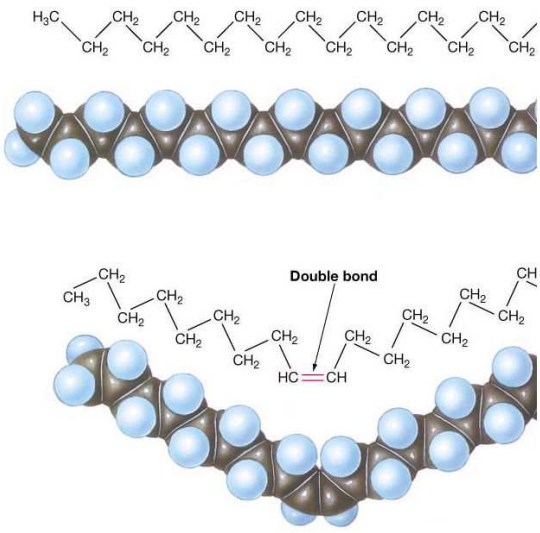

Figure 2.3: Hydrophobic 'tails' of saturated and unsaturated lipids [73].

This property is particularly significant when saturated and unsaturated phospholipids are combined in a bilayer structure. At a wide range of temperatures, these phospholipids are in different phases that separate out across the membrane and then cluster together to form regions known as microdomains. These microdomains are regions of tightly-packed saturated lipids in an ordered gel state that protrude from the fluidity of the loose unsaturated "kinked" lipids in a disordered liquid-crystalline state. These regions vary in size and height depending on the type and concentration of the lipids and the ambient temperature of the membrane. Phase

transitions in phospholipids and the formation of microdomains can occur for many reasons other than degree of saturation, such as hydrocarbon chain length, asymmetry and branching, as well as the type and position of chain attachment to the glycerol backbone [75].

The membrane of a living cell effectively defines it morphologically and functionally and microdomains are thought to play a central role in this [3]. They are important in a wide range of biological processes, including signal transduction, membrane trafficking and sorting, as well as cell death. A large number of membrane proteins have been associated with lipid microdomains and they have been suggested as entry points for viruses, bacteria or other toxins [76].

2.2 Modelling cell membranes

Naturally-occurring phospholipids are available commercially. When prepared correctly under the appropriate conditions, these phospholipids will self-organise to form a bilayer structure, supported by a solid surface. This is known as a supported lipid bilayer (SLB), a nanoscale structure that is used in scientific research to mimic cell membranes. All aspects of an SLB can be manipulated and modified to give a fairly good representation of the cellular system being depicted. An ideal SLB should have a composition that matches the lipid content of the membrane under investigation. It should also be highly hydrated (ideally immersed in an aqueous environment), open to interactions with other biomolecules present and free enough to allow for a certain amount of movement. This includes both in-plane and out-of-plane, since the position of the bilayer in a cell membrane fluctuates whilst molecules freely diffuse within it. In practice, compromises are often made to accommodate for experimental difficulties and scientific choices, but generally SLBs provide a simple and biologically relevant model of the real system [77].

Since an SLB is a planar structure on a solid support, only the top surface of the bilayer is exposed to the environment. This layout has many advantages over the other arrangements of phospholipids for the study of cellular membranes. One of the greatest advantages of SLBs is that they are well-defined and stable. Their structure will remain largely intact under a variety of conditions and environments and can be

studied *in situ*. SLBs can contain small defects without it affecting the overall structure of the bilayer. In fact these defects, known as holes, can be used to confirm the presence of an SLB (Figure 2.4a). The stability of this arrangement also means that experiments lasting weeks and even months are possible. Another advantage of SLBs is that they are suitable for a wide range of characterisation techniques, since they are formed on a hard, flat surface. This is not true for freely floating samples such as lipid vesicles. On the other hand, one limitation of SLBs is the possibility of unwanted interactions with the substrate supporting the structure. Also, the substrate must have a high level of cleanliness and flatness. SLBs generally do not directly touch the surface of the substrate, but they are separated by only a very thin stretch of water (commonly around 1nm deep). Therefore the choice of substrate is an important consideration when preparing SLBs.

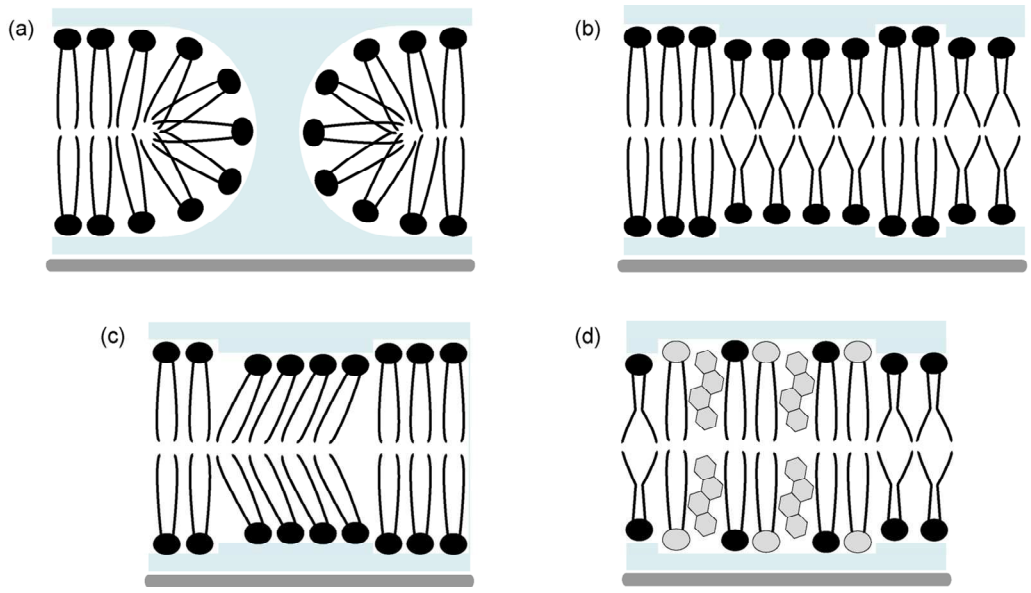

Figure 2.4: Illustration of phases of an SLB (a) Ordered gel state SLB containing a hole (b) Mixed SLB consisting of areas of both ordered gel phase lipids and disordered liquid-crystalline phase lipids (c) Ordered gel phase SLB with microdomains of disordered tilted lipids (d) SLB containing cholesterol and sphingomyelin, creating lipid rafts.

An SLB can be created with all the features of a real cell membrane. This includes phase-separated microdomains, which can be formed by combining appropriate saturated and unsaturated phospholipids in an SLB (Figure 2.4b). Microdomains can also occur in single phospholipid SLBs, in which some of the lipid molecules are in a disordered tilted phase (Figure 2.4c) [26]. A specific type of microdomain known as

lipid rafts form when cholesterol and sphingomyelin are added to a phospholipid SLB (Figure 2.4d) [78].

2.3 SLB synthesis methods

2.3.1 Lipid vesicle fusion

The lipids used in the work described in this thesis are dioleoylphosphatidylcholine (DOPC) and dipalmitoylphosphatidylcholine (DPPC) with molecular formulae $C_{44}H_{84}NO_8P$ and $C_{40}H_{80}NO_8P$ respectively (Figure 2.5). These molecules have the same chemical structure, apart from the length of their hydrocarbon 'tails' and the presence of carbon-carbon double bonds in the 'tail' of DOPC making it unsaturated. Consequently, these phospholipids are widely used in scientific research to model the cellular membrane as they readily form bilayers and phase-separated microdomains at room temperature [79-82].

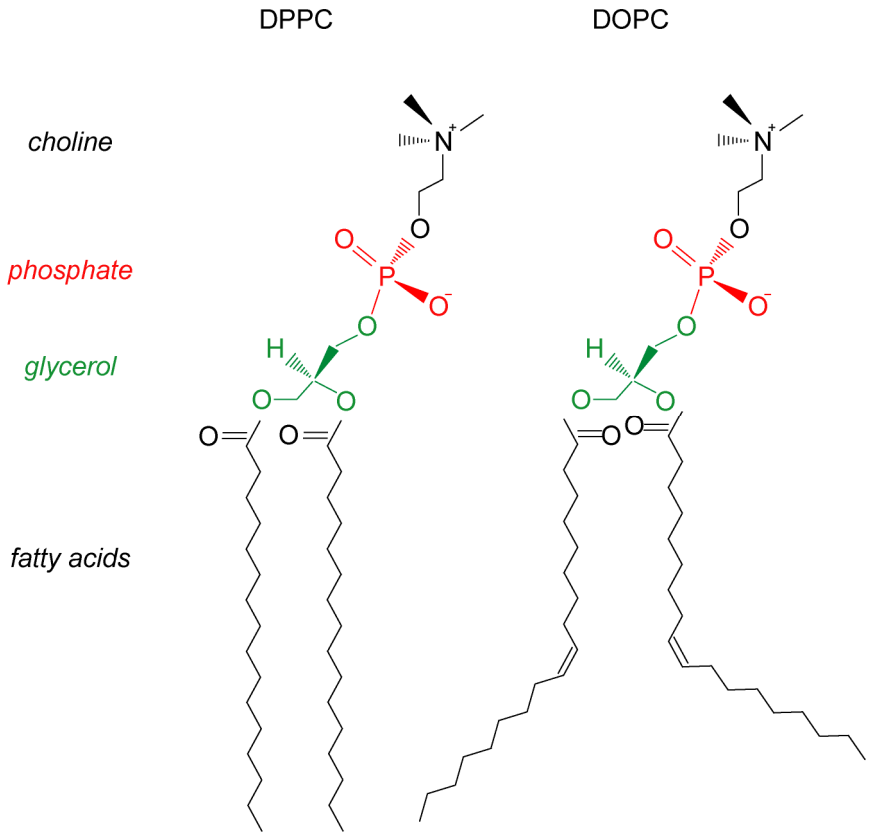

Figure 2.5: Chemical structure of phospholipids DPPC and DOPC.

DPPC and DOPC are bought as semi-synthetic lipids derived from egg lecithin (Lipid Products, UK). They come as a white powder, which is dissolved in a 5:1 mixture of chloroform and methanol to give a 50mg/ml lipid solution that can be stored long-term in the freezer.

The most common way to prepare an SLB of phospholipids is by lipid vesicle fusion. In this method, thin lipid films are hydrated to form stacks of liquid crystalline bilayers that become fluid and swell. These bilayers detach through agitation and self-close to form large, multilamellar vesicles that are reduced in size and fused to a solid support. Firstly, all equipment is cleaned thoroughly with a variety of solvents. Around 250µl of the 50mg/ml lipid solution is placed in a small round-bottomed flask and dried under a stream of nitrogen until a thin lipid film is formed. The dried lipid film is rehydrated with at least 1ml of water to give a milky solution known as a lipid cake. The lipid cake is frozen in liquid nitrogen and thawed several times. Finally, the suspension is extruded 11 times through a 19mm diameter polycarbonate filter with 100nm diameter pores (Avanti Polar Lipids), to produce a monodisperse, unilamellar suspension of 100nm diameter lipid vesicles (Figure 2.6) [83].

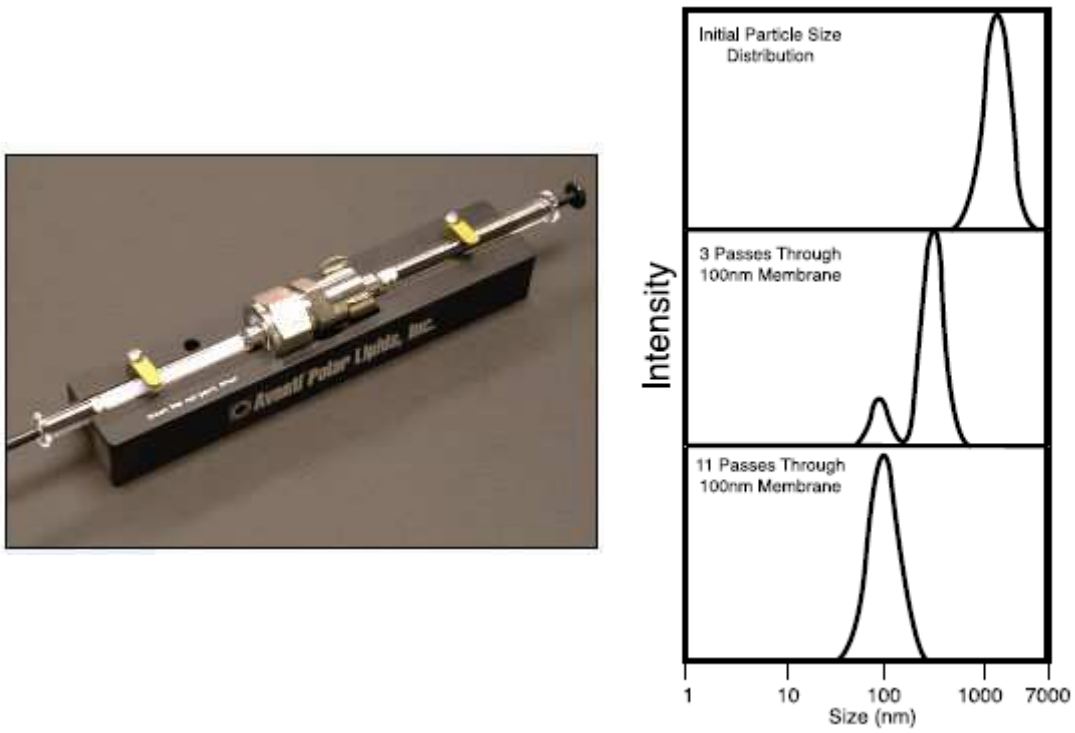

Figure 2.6: Mini-extruder for filtering lipid suspension and lipid vesicle size distribution during filtering [84].

The standard substrate for SLBs is mica, since it can be easily cleaved with adhesive tape to produce a clean, atomically-flat surface that lipid vesicles can attach to and spread across to form an SLB [85]. 50µl of the lipid vesicle suspension is diluted in 500µl of water. This solution is deposited on a $1cm^2$ piece of freshly-cleaved mica that has been previously treated with 50µl of 10mM magnesium chloride ($MgCl_2$) to encourage fusion of the lipid vesicles into a bilayer. The sample is left for around 3hrs, in which time the vesicles spontaneously adsorb onto the hydrophilic surface of the mica, rupture and spread across the substrate (Figure 2.7). Following this, the sample is washed with water several times to remove any vesicles that remain unfused to the mica. This results in a unilamellar SLB formed between two layers of water, which must be kept hydrated to remain stable.

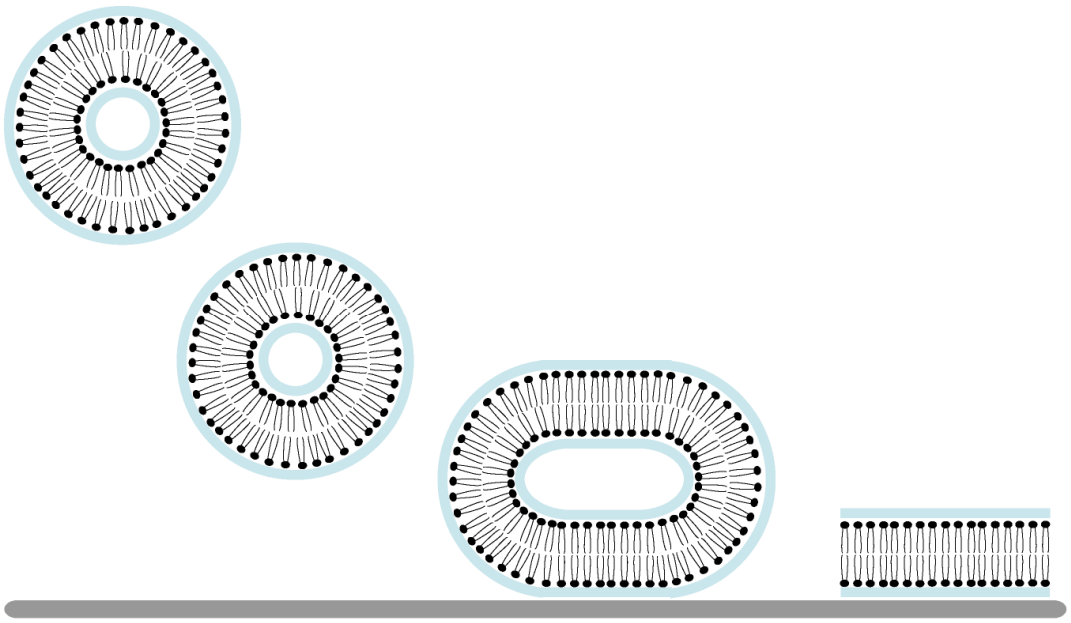

Figure 2.7: Fusion of lipid vesicles into an SLB across a prepared substrate.

2.3.2 Langmuir-Blodgett technique

A second but slightly less common way to produce SLBs is by the LB technique [86, 87]. This method uses an LB trough, which consists of a rectangular Teflon bath equipped with moveable barriers (Nima Technology) that compress a monolayer of amphiphilic molecules on an air-water interface and transfer it onto a solid support (Figure 2.8).

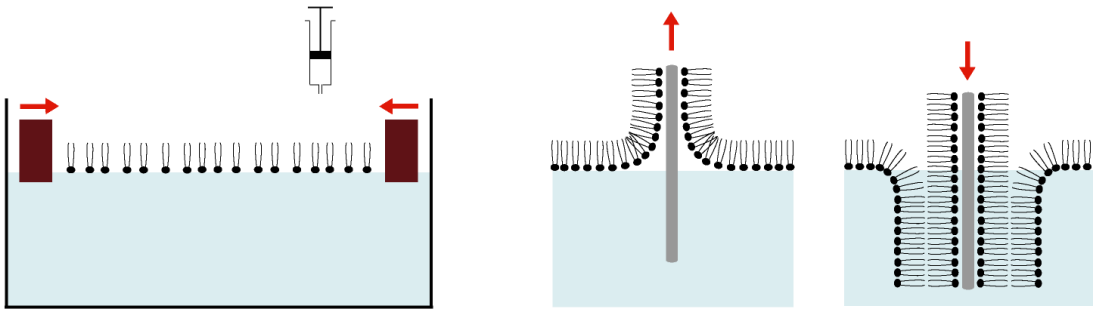

Figure 2.8: Formation of an SLB onto a prepared substrate from an LB trough.

Firstly, the trough and all equipment is cleaned with lint-free tissues and chloroform. Then the trough is filled with ultra-pure water; this is the subphase. The barriers are closed whilst a surface pressure-area isotherm is recorded by the Wilhelmy plate, which is a small piece of chromatography paper that is submerged into the subphase. If this returns a flat isotherm, the surface of the water is clean enough to continue.

The barriers are re-opened, ready for the deposition of phospholipids. Around 250µl of the 50mg/ml lipid solution (stored in chloroform and methanol) is placed in a small round-bottomed flask and dried under a stream of nitrogen until a thin lipid film is formed. The dried lipid film is resuspended in chloroform to result in a 2mg/ml milky solution. This solution is slowly dropped onto the subphase and left for around 15mins for the lipid molecules to spread and the solvent to evaporate. Then the barriers are closed at a rate of 100cm^2/min to form a solid monolayer of lipids, whilst the isotherm is recorded to monitor packing and organisation of the molecules (Figure 2.9). The monolayers are transferred onto a 1cm^2 piece of freshly-cleaved mica that has been previously treated with 50µl of 10mM $MgCl_2$. The mica is drawn upwards through the LB trough at a dipping speed of 10mm/min; the lipid molecules interact with the mica through their polar 'heads', exposing their hydrophobic 'tails' to the environment. The mica is then immersed a second time through the interface to obtain an SLB. Again, this structure must be kept hydrated to remain stable.

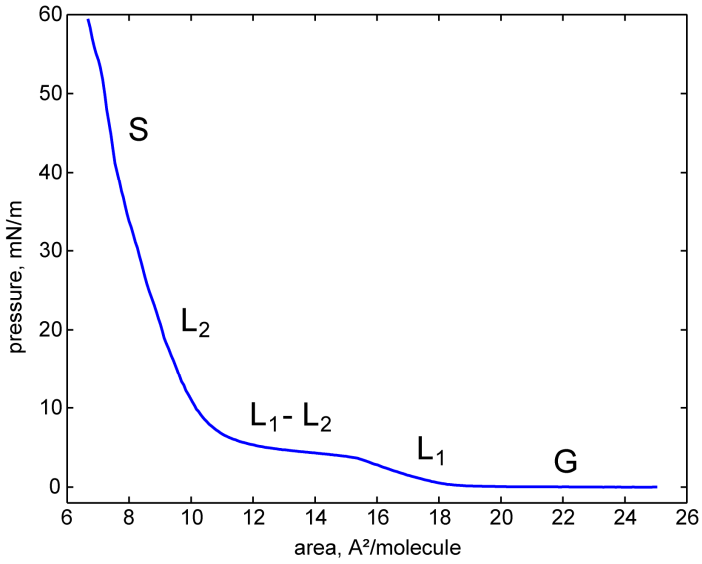

Figure 2.9: Surface pressure-area isotherm from the compression of a monolayer of DPPC on water (four distinct regions of gaseous (G), liquid (L_1 and L_2) and solid (S) phase are indicated, as well as a horizontal transition phase (L_1-L_2) between the two different liquid phases).

Chapter 3

Atomic force microscopy

A description of AFM is given here, which is the surface characterisation technique used in this work. Its development is detailed, as well as the main principles, imaging modes and applications of the instrument. Particular attention is paid to the use of AFM to study biological materials in liquid.

3.1 Development

Atomic force microscopy (AFM) is a non-destructive characterisation method that is widely used in science and technology to analyse all types of materials and surfaces. It is one of the many scanning probe microscopy (SPM) techniques to evolve over the past three decades, stemming from the initial development of the scanning tunnelling microscope (STM) in 1982 [88]. The principle of all SPM techniques is to measure a specific property of a material by bringing a probe in close proximity with its surface and scanning across it in a raster pattern. The interaction between the probe and the surface of the material that arises from measuring this property is used in a feedback loop to build up a high-resolution image of the scanned area, pixel by pixel. Across the variety of SPM instruments now available, a broad range of physical properties can be investigated including chemical structure, charge distribution, capacitance and conductance [89]. The properties used as the basis for AFM are the long-range attractive van der Waals interactions between the probe and the surface and the short-range repulsive forces due to overlap of electronic orbitals.

Since van der Waals interactions are present between the atoms of any material, AFM has no limitations with regards to the electronic nature of samples that it can study. This is a major advantage of AFM over the other predominant SPM technique STM, which requires that the sample being studied is conducting. AFM also has a number of advantages over scanning electron microscopy (SEM), a popular surface analysis technique that images the surface of a material by scanning it with a high-energy beam of electrons. Firstly, AFM provides a three-dimensional (3D) profile of a surface, without the need for any special sample preparation or treatment. It works perfectly well in air or liquid, whereas SEM requires a vacuum environment to operate properly. Also, in principle, AFM can provide higher resolution than SEM.

3.2 Basic principles of the instrument

3.2.1 The probe

The probe of an AFM is essential to its performance, since it is the force between this and the surface of a material that is used to create topographical images of the surface as well as collecting a huge amount of mechanical information about the material. The AFM probe can be thought of simply as a spring, oscillating up and down as it is moved across the surface. As it scans, the forces between its tip and the material cause the spring to deform; it is these deformations that are measured to produce a mapping of the surface. The forces detected by AFM are generally on the order of 10^{-6}-10^{-12}N. In order to show a measurable reaction to forces on this scale, the probe must be highly sensitive. However, at the same time, mechanical vibrations must be minimised. Therefore the spring system must be as soft as possible to allow maximum deflection with a resonant frequency high enough to reduce the effects of noise. The balance of these two factors arises from the equation for a spring,

$$\omega_0 = \left(\frac{k}{m}\right)^{1/2} \tag{3.1}$$

where ω_0 is the resonant frequency of the system, k is its spring constant and m is the effective mass. This demonstrates that for a system to have high sensitivity to small forces a small value of k is required, whilst to achieve minimal noise a large value of

ω_0 is necessary. Therefore it is apparent from the above expression that this system must have a minimum value of m. In the case of AFM, this necessitates the probe being as small as possible.

An AFM probe consists of a cantilever with a tiny, and preferably very sharp, tip (Figure 3.1). The forces between this tip and the surface of a material cause the cantilever to bend and it is this deflection that is measured and converted into a topographical image of the surface.

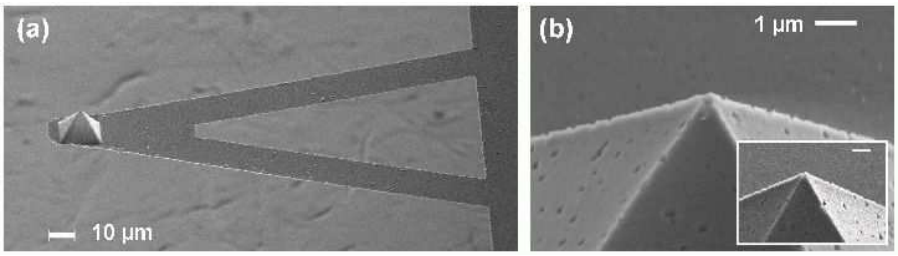

Figure 3.1: Electron micrographs of (a) a typical AFM cantilever and (b) its tip.

3.2.2 Detection methods and feedback

A variety of different methods have been employed to detect the deflection of the cantilever in AFM systems. In the original setup it was measured by the change in tunnel current of an STM, which was mounted at the rear of the cantilever [90]. This particular arrangement presents numerous difficulties and has since been replaced with techniques such as optical interferometry and capacitive sensing. However, the easiest detection method to implement and consequently the most commonly used in modern AFM is laser beam deflection (Figure 3.2).

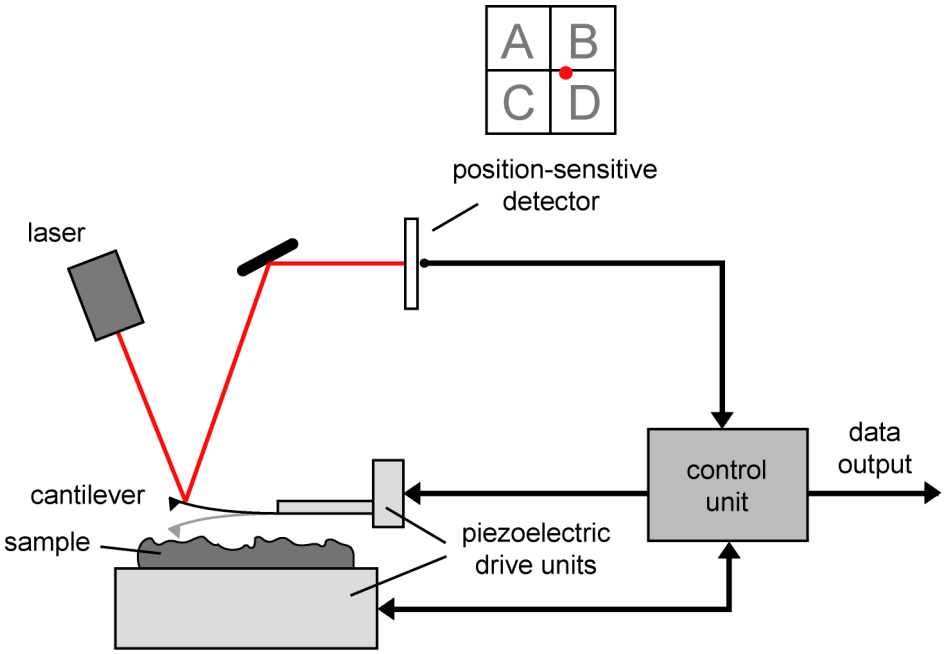

Figure 3.2: Schematic of a typical AFM operating system.

In this detection method the rear side of the cantilever has a reflective coating onto which a laser beam is focused and then reflected back onto a position-sensitive detector. Any deflection of the cantilever causes a movement in the reflected laser beam and its position is shifted on the detector. It is this change in position of the signal recorded by the detector that can be used to measure the deflection of the cantilever. Laser beam deflection has many distinct advantages over other detection methods, including its extreme simplicity and high sensitivity. Additionally, the force exerted on the cantilever by the laser beam is negligible. This means that the motion of the cantilever is not affected by the detection method, which would contaminate the AFM signal.

The positioning of the sample with respect to the tip is controlled by a combination of piezoelectric crystals, typically one set in the sample stage and another in the cantilever holder. The piezoelectric crystals in the cantilever holder are used to oscillate the cantilever when the AFM is used in dynamic mode, which is discussed in the following section. The piezoelectric crystals in the sample stage are used to produce the scanning motion of the sample relative to the tip and to change the probe-surface distance in response to changes in the deflection of the cantilever. In almost all SPM techniques, these piezoelectric drive units are accompanied by a

feedback mechanism. In AFM, this mechanism works to adjust the probe-surface distance in order to maintain a constant force between the tip and the sample. It is established before scanning commences, when a reference value for the deflection of the cantilever is given. This is known as the setpoint voltage and is chosen to be just below the 'free air' amplitude voltage of the cantilever, which is the point at which the cantilever begins to feel the presence of the surface (Figure 3.3). During scanning, changes in the structure of the surface cause the deflection of the cantilever to vary. In response to this the piezoelectric crystals in the sample stage raise or lower the sample in an effort to return the deflection to its setpoint value. The amount that the piezoelectric crystal has to raise or lower the stage to accomplish this is used as a direct measurement of the surface topography.

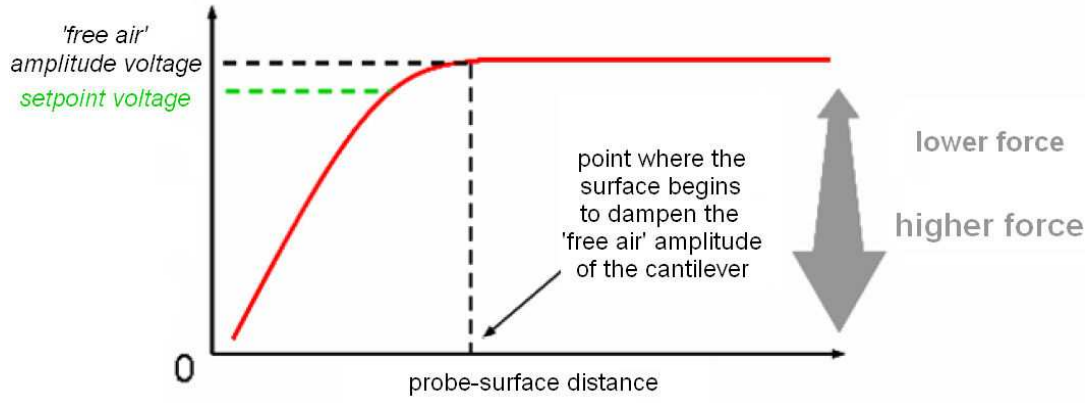

Figure 3.3: A qualitative, conceptual sketch of amplitude voltage vs. distance, illustrating the choice of setpoint voltage.

3.2.3 Modes of operation

AFM has two principal imaging modes known as contact and non-contact mode. As the names suggest, this is where the probe is respectively in and out of contact with the surface of the material being studied. These two modes of operation use different regions of the probe-surface interaction to build up a topographical mapping of the surface (Figure 3.4). Non-contact mode AFM measures the long-range van der Waals interactions between the tip and the surface. This mode is performed at least 10nm above the surface, below which point the interactions are strong enough to cause the tip to "snap" to the surface. Contact mode measures the short-range repulsive forces that arise between the tip and the surface when they are in contact.

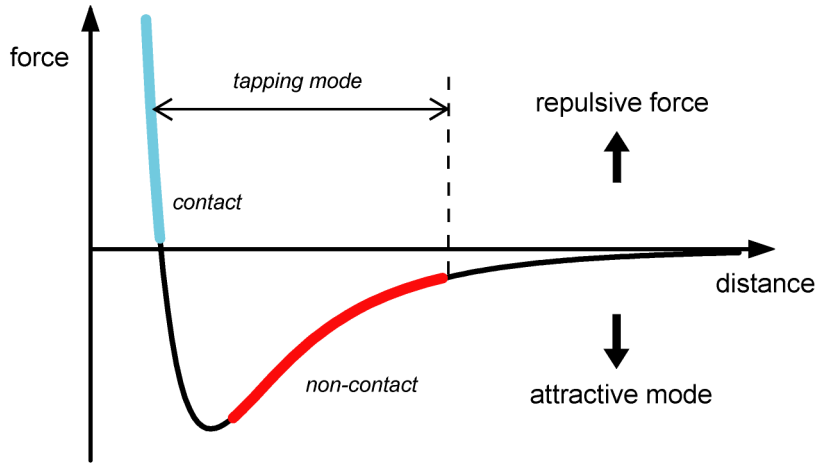

Figure 3.4: Graphical representation of a typical force-distance relationship between an AFM probe and a surface (the regions that correspond to contact, non-contact and tapping mode operation are highlighted).

However, there are several disadvantages to these static modes of operation. Contact mode AFM can suffer from probe or sample degradation effects, since it involves large lateral forces that are exerted by the probe on the surface of the sample. This is particularly critical when imaging soft samples such as biological materials, which could be altered or even damaged by these forces. Non-contact mode removes the risk of destroying the sample. However, this is at the expense of resolution. The relatively large distances between the tip of the probe and the surface greatly reduce the magnitude of forces that act on the cantilever and this in turn reduces the ability of the probe to resolve small surface features. The probe-surface distances involved in non-contact mode also create a problem when studying samples in liquid, since the movement of fluid surrounding the system makes it difficult to stabilise imaging.

In response to the shortfalls of contact and non-contact mode, development of the technique focused on increasing the sensitivity and resolution of non-contact mode. One of the most important outcomes of this work was the introduction of oscillating cantilevers [90]. This brought about a dynamic mode of operation, in which the cantilever is driven to oscillate at its resonance frequency by a piezoelectric drive unit. As the tip approaches the surface, the cantilever experiences a force gradient F', which induces a shift in the resonant frequency of the cantilever,

$$\Delta\omega \approx -\frac{F'}{2k} \tag{3.2}$$

The minimum detectable frequency shift of an oscillating cantilever corresponds to a much smaller applied force than the minimum detectable cantilever deflection in the case of a static cantilever (as in contact and non-contact mode), which increases the vertical resolution of the probe. This change in the resonant frequency is monitored by either amplitude or frequency detection. Amplitude detection measures changes in the amplitude of oscillation of the cantilever and uses a feedback loop to adjust the probe-surface distance to maintain this amplitude at a fixed value. Similarly, frequency detection measures the frequency of oscillation of the cantilever and uses a feedback loop to maintain this frequency at a setpoint value.

Further improvements came with the development of a hybrid mode of AFM between that of contact and non-contact mode, known as tapping mode (Figure 3.4) [91]. This mode uses an oscillating cantilever, but positions it much closer to the surface than before so that the probe gently taps the surface at the "bottom end" of its oscillation. This tapping of the surface reduces the amplitude of oscillation of the cantilever from its 'free air' value and induces a shift in its resonant frequency. Again, the reduced amplitude of oscillation is maintained at a fixed value by a feedback mechanism. Tapping mode AFM seemingly combines the benefits of the original two modes; short contact times between the tip and the surface eliminate the destructive lateral forces present in contact mode, whilst retaining its excellent resolution. For this reason, tapping mode is a popular choice for imaging in modern AFM and is essential for a number of key applications.

3.3 Imaging in liquids

In the physical sciences, AFM is predominantly used to study hard, solid samples in air. However, it has also become an invaluable research tool for studying materials of a biological nature. These materials present new challenges for the technique, since in most cases they are very soft and must be kept hydrated at all times. This requires the use of liquid AFM, whereby both the sample and probe are totally immersed in fluid. This variation on the traditional setup introduces new forces and effects that arise from the presence of liquid around the system. Therefore extra consideration must be given to many aspects of setting up the AFM, including the

mode of operation, the choice of cantilever and the values of most imaging parameters.

Tapping mode AFM is always chosen when studying samples in liquid [92]. Contact mode risks altering or even damaging soft, biological materials due to the large forces the probe exerts on the surface it is scanning. This can be avoided by using non-contact mode, as the tip is scanned at relatively large distances above the surface. However, the movements in the fluid within this space would make it almost impossible to obtain good sensitivity and resolution. Tapping mode can achieve the resolution of contact mode alongside the gentleness of non-contact mode, making it ideal for studying biological materials.

An oscillating cantilever is always required when imaging with tapping mode; however, when working in liquid the choice of cantilever is especially important. Typically, long triangular silicon nitride cantilevers with low spring constants are used in liquid AFM, because they are soft and flexible and can tolerate the fluid dynamics in the system. However, to be able to use this setup successfully, most imaging parameters need to be chosen very carefully and treated differently than they are when operating in air. First and foremost, the cantilever requires special tuning to determine its resonance frequency. In liquid AFM, a thermal tune is required in order to identify the region in which the resonant frequency of the cantilever lies, as it can be difficult to locate amongst the random resonances of the cavity of liquid surrounding it (Figure 3.5). Before approaching the surface a setpoint voltage is chosen that is very close to the 'free air' amplitude of the cantilever, so that there is minimum force experienced between the tip and the sample. This value can then be slowly decreased whilst imaging to obtain good resolution. It is also optimal to scan at a slower rate than in air, to reduce movements in the fluid surrounding the system.

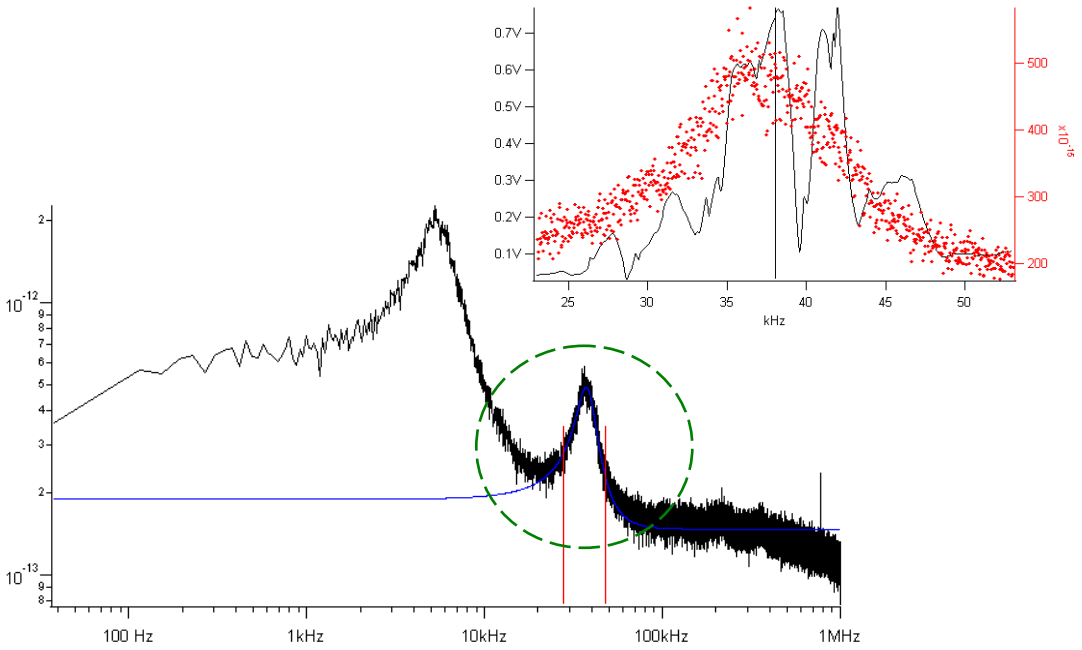

Figure 3.5: Experimental data demonstrating the combination of thermal and cantilever tuning used in liquid AFM to isolate the resonance frequency of the cantilever from cavity resonances (black trace in bottom plot is overlaid in red in top plot).

3.4 Force spectroscopy

Besides imaging, there are a wide variety of applications of AFM. One of these is force spectroscopy, which provides a direct measurement of probe-surface interaction forces as a function of the distance between the tip and sample. These forces are determined by the deflection of the cantilever, which is monitored as the AFM probe is extended towards and retracted from the surface by the piezoelectric drive units. Over this approach and retract cycle, variations in the cantilever deflection arise due to elastic properties of the sample and interactions between the tip and the surface such as binding, adhesion and rupture.

Force spectroscopy measurements are observed as a force curve (Figure 3.6). Typically, force curves consist of an approach and a retract trace, which each have a diagonal region where the probe is in contact with the surface and a flat region where the probe is away from the surface. Force curves also contain a number of key features that are specific to a particular sample and reveal a wealth of mechanical information about it. A significant aspect of the approach trace is the point at which the tip first comes into contact with the sample. This is where the tip is close enough

to the surface of the sample to experience attractive van der Waals forces, which cause the tip to 'snap' to the surface. This is denoted as a sudden decrease in the deflection of the cantilever as it bends towards the sample. After this point, the piezoelectric crystal driving the cantilever is extended further to move the cantilever into the surface, causing its deflection to increase. Then at full extension of this crystal it begins to retract. The retract trace of a force curve initially follows the same path as the approach trace. However, the point at which the tip eventually leaves the surface of the sample diverts from this trace and is of great interest. In many cases there is some adhesion experienced between the tip and the sample due to the nature of the sample. Additionally, in ambient conditions many surfaces are covered in a layer of water, which exerts a strong, attractive capillary force. Therefore as the tip is pulled away from the surface, the cantilever is bent as the tip is held in contact with the surface. At some point, depending upon the adhesive quality of the sample or the thickness of the water layer, the probe is retracted enough that the tip jumps free and moves away from the surface.

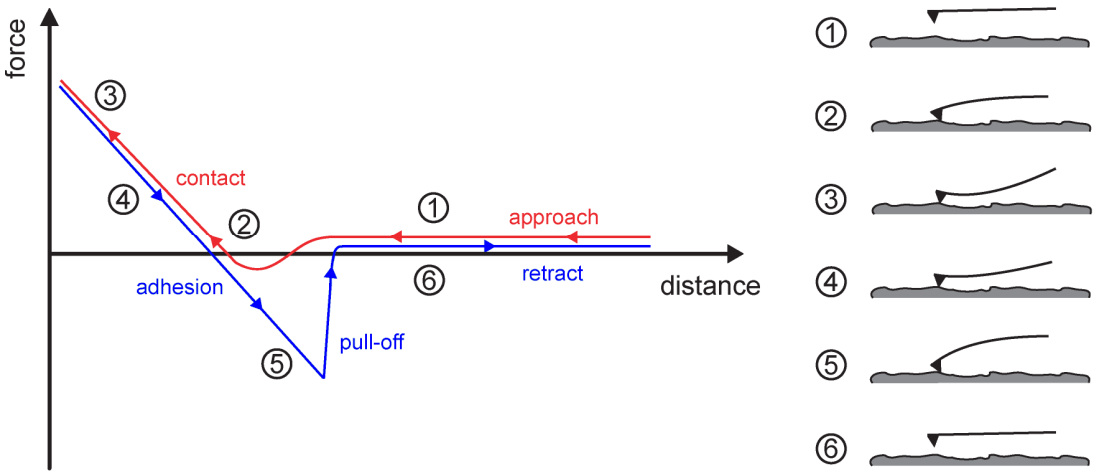

Figure 3.6: A typical approach and retract cycle, or force curve (numbered points on the curve and corresponding illustrations highlight key interactions between an AFM probe and a surface).

Force spectroscopy is used in a broad range of research areas to investigate the physical properties of surfaces. However, in recent years it has been employed extensively for the study and manipulation of single molecules. One main application of the technique is the study of the mechanical resistance of chemical bonds, in which the tip of an AFM probe is functionalised with a molecule that binds to a molecule on a surface. Work in this field has included the study of many

biological systems such as antibody-antigen, protein-protein and protein-cell interactions [93-95]. Force spectroscopy has also been used to study the elasticity of materials, which are adsorbed to a surface and then stretched by the AFM probe. Much of this work has focused on biopolymers such as DNA, RNA and proteins [96-98].

Chapter 4

Raman spectroscopy methods

This chapter outlines the Raman spectroscopy methods employed in these studies. The background and theory of non-resonant Raman spectroscopy, SERS and TERS is described as well as the relevance of these methods to the investigation of SLBs.

4.1 Raman spectroscopy

4.1.1 The Raman Effect

Raman spectroscopy is an optical analysis technique based on an effect discovered by Chandrasekhara Venkata Raman (Figure 4.1). Raman was a self-made scientist who was known for his outrageous ideas, simple experimental design and in-depth observations. An interest in optical phenomena led him to demonstrate in 1921 that the scattering of light is responsible for the colour of the ocean rather than sky reflection or absorption as previously thought [99]. Then in 1928 he discovered the inelastic scattering of light, or Raman Effect, which won him the Nobel Prize two years later [100]. These experiments used a narrow band photographic filter to produce a monochromatic light source from sunlight, a "crossed" filter to block scattered light and the human eye as a detector. Raman and his co-worker Krishnan found that when a benzene sample was irradiated by this intense monochromatic light source, light of a different frequency passed through the "crossed" filter.

Figure 4.1: A commemorative stamp of Chandrasekhara Venkata Raman, issued in India for National Science Day 1972.

Since these early days of crude instrumentation, Raman spectroscopy has gradually developed to become a well-established scientific tool. The effect was subject to intensive research in the first decade after its discovery. However, during the Second World War it became overshadowed by infrared spectroscopy, a technique that was enhanced by the development of sensitive detectors and advances in electronics. The popularity of Raman spectroscopy was not restored until the invention of the laser in the early 1960s and has grown steadily since. In recent years, instrumentation has progressed with the availability of durable and affordable lasers and increasing accessibility of high-powered computer technology. Nowadays Raman spectroscopy is widely used to analyse materials well beyond the capabilities of other methods, with the ability to obtain a detailed account of the physical and chemical makeup of a material at the molecular level.

The fundamental process of the Raman Effect is the transfer of energy between light and matter. Raman spectroscopy employs this effect by measuring the scattering of light from molecules in different vibrational states of a material and the consequent energy exchange between the incoming light and the molecules [27]. When a beam of monochromatic electromagnetic radiation impinges on a material, it can be either scattered or absorbed (Figure 4.2). If light is scattered from an atom or molecule within the material, most photons are elastically scattered. This is known as Rayleigh scattering, in which the scattered photons have the same energy E as the incident photons given by

$$E = h\nu_0 \tag{4.1}$$

where h is Plank's constant and v_0 is the frequency of the incident light. However, a small fraction of scattered light (approximately 1 in every billion photons) undergoes what is known as inelastic or Raman scattering. In this case light is scattered from molecules with frequencies of oscillation that vary from the frequency of the incident photons. It is this difference in frequency, or energy between the incoming and outgoing light that is the measurable quantity used as the basis of Raman spectroscopy.

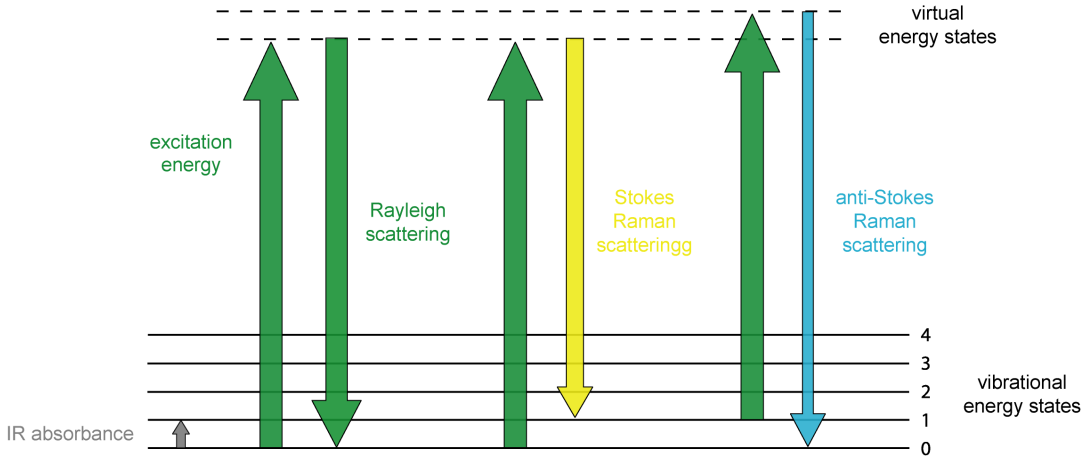

Figure 4.2: The absorbance and scattering of light from matter.

4.1.2 Stokes and anti-Stokes Raman scattering

The Raman Effect comprises of two distinct types of scattering, known as Stokes and anti-Stokes scattering (Figure 4.2). The most likely to occur is Stokes scattering, in which the incident light interacts with a molecule that absorbs energy from it. This molecule is excited from its ground state to the "virtual state" and then relaxes back down to finish in a vibrational excited state. In this case photons are scattered that are lower in energy and frequency than the incoming photons and therefore longer in wavelength. Anti-Stokes scattering is the less probable and weaker effect, which occurs when light interacts with a molecule that is already in a vibrational excited state. After being excited up to the "virtual state" this molecule falls down to the ground state, causing the incident photons to gain energy and scatter at a higher frequency and shorter wavelength.

A classical treatment of Raman scattering demonstrates the occurrence of these two effects mathematically [28]. The electric field strength $\boldsymbol{E}$ of the incoming electromagnetic radiation is given by

$$\boldsymbol{E} = \boldsymbol{E}_0 \cos(2\pi\nu_0 t) \tag{4.2}$$

where t is time, $\boldsymbol{E_0}$ is the vibrational amplitude of the electric field and ν_0 is the frequency of the radiation. When this light interacts with a molecule, it induces an electric dipole moment

$$\boldsymbol{P} = \alpha\boldsymbol{E} = \alpha\boldsymbol{E}_0 \cos(2\pi\nu_0 t) \tag{4.3}$$

where α is known as polarisability. Molecular polarisability can be interpreted as the deformability of the electron cloud by the external electric field. In general, α is a tensor that depends on $\boldsymbol{E}$. However, for simplicity the tensor properties of polarisability are neglected here. The above oscillatory dipole moment allows scattering to occur, as the molecule moves to an excited state. The charge distribution in the material is then vibrating with a frequency ν and nuclear displacement

$$q = q_0 \cos(2\pi\nu t) \tag{4.4}$$

where q_0 is the vibrational amplitude. These oscillations may induce a change in the polarisability of the molecule. When q is small, polarisability varies linearly with displacement and can be approximated by a Taylor series expansion of α resulting in

$$\alpha = \alpha_0 + \left(\frac{\partial\alpha}{\partial q}\right)_0 q_0 + \ldots \tag{4.5}$$

where α_0 is the polarisability at equilibrium and produces elastic scattering, whilst $(\partial\alpha/\partial q)_0$ is the rate of change of α with respect to q at this point and is the origin of inelastic scattering. Combining the previous three equations, making substitutions and simplifying gives

$$\boldsymbol{P} = \alpha_0 \boldsymbol{E}_0 \cos(2\pi\nu_0 t) + \frac{1}{2}\left(\frac{\partial\alpha}{\partial q}\right)_0 q_0 \boldsymbol{E}_0 \left[\cos\{2\pi(\nu_0 - \nu)t\} + \cos\{2\pi(\nu_0 + \nu)t\}\right] \quad (4.6)$$

The result is an expression consisting of two terms. The first term represents the outgoing light that remains unchanged from when it enters the material, possessing the frequency of the incident light ν_0. This is Rayleigh scattering. The second term represents the inelastically scattered light and contains two frequency shifts $(\nu_0 - \nu)$ and $(\nu_0 + \nu)$ arising from Stokes and anti-Stokes Raman scattering respectively.

4.1.3 Measurement and interpretation of a Raman spectrum

The key to using Raman scattering to investigate the physiochemical makeup of a material is the change in photon energy between the incident and scattered light, measured as the shifts in frequency derived previously. As shown in Figure 4.3, light exits a material at a number of different energies that are shifted from the original energy of the incoming photons E. In this case the more probable Stokes scattering is demonstrated, in which there is a loss in energy and therefore a decrease in frequency. These different energy changes, ΔE_1 etc, correspond to light scattering from molecules being excited to a number of distinct vibrational energy levels. The frequency shifts corresponding to these different molecular vibrational modes, $(\nu_0 - \nu_1)$ etc, are displayed as a spectrum of peaks. The position and intensity of each peak relates to a specific type of molecular vibration such as the stretching, bending, torsion or deformation of a bond, combining to form a spectrum that represents the chemical fingerprint of a material.

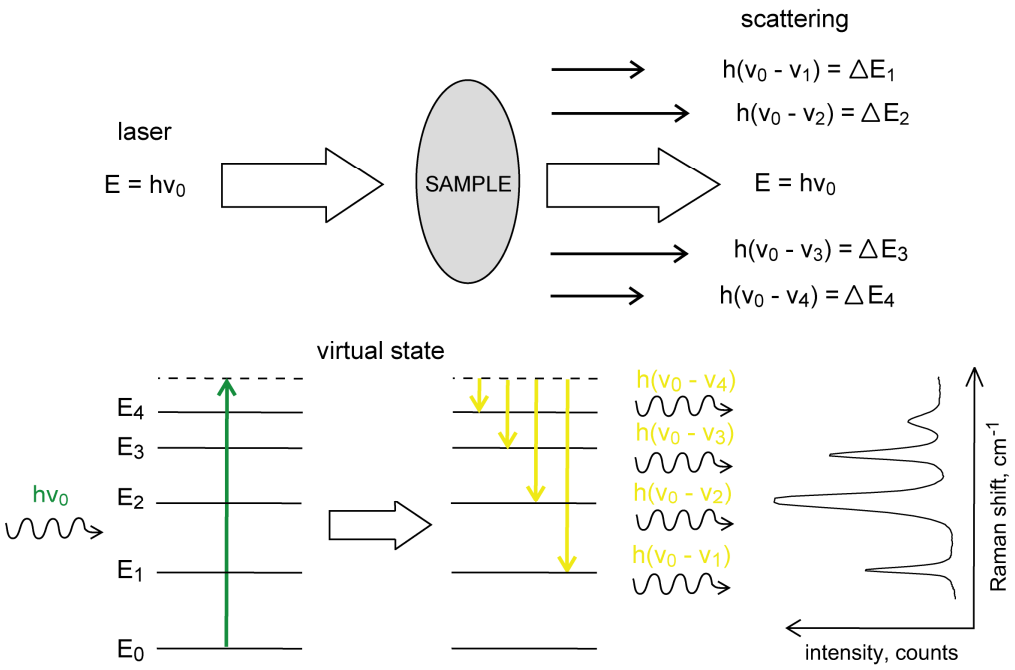

Figure 4.3: Schematic representation of Raman scattering (notation explained in text).

A full Raman spectrum is made up of Rayleigh, Stokes and anti-Stokes peaks (Figure 4.4). The Stokes and anti-Stokes Raman bands are much weaker than the Rayleigh line and occur symmetrically on either side of it, corresponding to the same amount of energy lost and gained respectively by the incident photons. The Boltzmann distribution indicates that within a system at thermal equilibrium, the lower energy state is more populated than the higher energy state. For a material, this translates to a larger number of molecules in lower energy states than in higher energy states. Therefore in a Raman spectrum the bands relating to Stokes scattering are more intense than those corresponding to anti-Stokes scattering. These peaks have a magnitude of light intensity, or counts, and are usually displayed as a Raman shift $\tilde{\nu}$. This parameter is common to vibrational spectroscopy. It is essentially wavenumber with units of cm^{-1} and is related to wavelength λ and frequency ν via

$$\tilde{\nu} = \frac{\nu}{c} = \frac{1}{\lambda} \tag{4.7}$$

where c is the speed of light. In Raman spectroscopy, the unit of wavenumber is used simply for convenience. If wavelength or frequency were used, the position of peaks in a spectrum would be determined by the wavelength of the excitation light

that they originated from. Instead spectra are displayed in Raman shifts from the Rayleigh peak, which is always set to 0cm^{-1}. This means that the positions of peaks for a particular material are independent of the excitation wavelength. Experimentally, a Raman shift can be determined from

$$\tilde{\nu}\left(cm^{-1}\right) = 10^7\left(\frac{1}{\lambda_0} - \frac{1}{\lambda_R}\right) \tag{4.8}$$

where λ_0 and λ_R are the laser wavelength and Raman scattering wavelength respectively, both in nanometres.

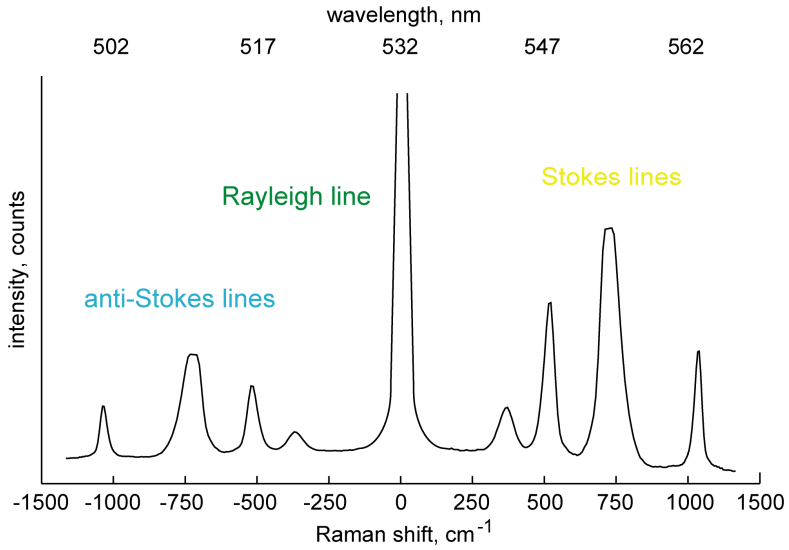

Figure 4.4: Schematic Raman spectrum consisting of Rayleigh, Stokes and anti-Stokes scattering.

An example of a typical Raman spectrum is shown in Figure 4.5. It is the spectrum of paracetamol, a widely used drug for relieving pain and reducing fever. It has the chemical formula $C_8H_9NO_2$ and consists of a benzene ring core, substituted by one hydroxyl group and the nitrogen atom of an amide group. The Raman spectrum of paracetamol contains many bands, each representing a distinct molecular vibration. Over the range of Raman shifts shown, characteristic peaks include those representing amide carbonyl group vibrations around 1200cm^{-1} and stretching of aromatic C–O and C–N bonds around 1500-1600cm^{-1}.

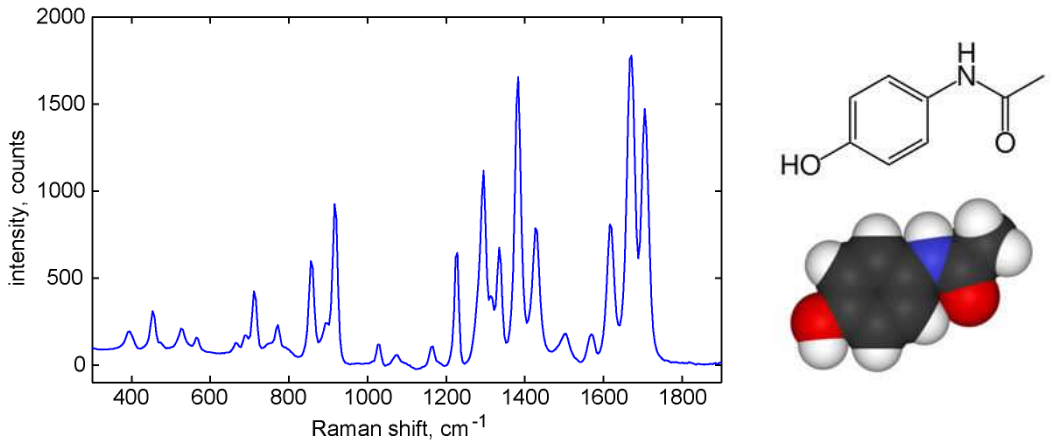

Figure 4.5: Raman spectrum and molecular structure of paracetamol.

4.1.4 Vibrational spectroscopy selection rules

All transitions between energy states of a molecule are governed by certain conditions known as selection rules. These rules restrict the physical properties of the initial and final state of a molecule that are necessary for a transition to occur with a non-zero probability. In terms of Raman spectroscopy, this concerns the polarisability derivative introduced in Equation 4.5. The distortion of a molecule in an electric field, and therefore the likelihood of light being scattered from it (scattering cross-section), is determined by its polarisability. The molecular transition from which a Raman shift occurs can only be activated optically when the corresponding vibration of the molecule changes polarisability, that is

$$\left(\frac{\partial \alpha}{\partial q}\right) \neq 0 \tag{4.9}$$

The polarisability of a molecule depends on how tightly the electrons are bound to its nucleus. For instance, in the symmetric stretch of the carbon dioxide molecule the strength of electron binding is different between the minimum and maximum inter-nuclear distances. Therefore the polarisability changes during this vibrational mode and it is Raman-active. In the asymmetric stretch the electrons are more easily polarised in the expansion of the bond than in the compression. There is no overall change in polarisability, so no Raman scattering arises from this stretching vibration.

Polarisability is also a function of the shape and size of a molecule and is expressed as a scalar or tensor depending on its spatial direction.

The polarisability of a molecule also determines the intensity of Raman bands, alongside the power and frequency of the incident light source [27, 28]. The Raman scattering intensity is given by

$$I_R = KI_0(\nu_0 - \nu)^4 \left(\frac{\partial \alpha}{\partial q} \right)^2 \tag{4.10}$$

where K is a proportionality constant, I_0 is the incident radiation intensity and ν is the frequency of vibration of the molecule. The value of K is dependent on the efficiency of the collection of Raman scattering and a number of other factors. The frequencies of molecular vibrations are very small in comparison to the frequency of the excitation light, therefore the term $(\nu_0 - \nu)^4$ can be approximated as ν_0^4 or λ_0^{-4}. This means that the intensity of the Raman signal depends inversely on the wavelength of the incident light to the power of four, therefore lasers with shorter wavelengths provide much stronger Raman scattering. In addition, the intensity of Raman bands varies with the polarity of molecules. The vibrations of highly polar functional groups, such as the O–H bond, are usually weak. This is the reason that water does not interfere with Raman spectroscopy studies of biological samples measured in aqueous solutions. Conversely, molecules that contain functional groups with well distributed electron clouds, such as carbon-carbon double bonds, are very Raman-active. Bending or stretching deformations of these bonds changes the distribution of electron density substantially and causes a large change in the induced dipole moment.

Under certain conditions, the selection rules of Raman spectroscopy may be modified. One of the most common ways that this can occur is for the collection of scattering from molecules that are adsorbed on a surface. Depending on the orientation that the molecule is attached to the surface its symmetry can vary, which in turn changes the vibrational modes of the molecule that are Raman-active. This is significant for surface-enhanced Raman spectroscopy (SERS) [101, 102]. The name

of this technique implies that it provides the same information as conventional Raman spectroscopy, but with enhanced signal. However, the interactions between the material being studied and the metallic surface that activates SERS causes differences in the Raman bands detected as compared with those detected by the conventional non-resonant method. The SERS spectrum of a molecule often contains peaks that are slightly shifted in frequency from those in the Raman spectrum of that molecule, or even absent. SERS spectra can also contain extra peaks. Additionally, in most cases different Raman bands exhibit different levels of enhancement. This is also true for studies using tip-enhanced Raman spectroscopy (TERS) to enhance scattering, in which the presence of a metallic tip modifies the Raman spectroscopy selection rules [103-105].

4.1.5 Advantages and disadvantages

Raman spectroscopy has long been used in many areas of physics, chemistry and materials science [106]. However, more recent applications of the technique have been in biological and medical research, both *in vitro* and *in vivo* [107, 108]. Raman spectroscopy offers many benefits to work in these fields:

(1) It is non-invasive, requiring no labelling or other preparation of the sample;
(2) As long as suitable laser wavelengths, powers and exposure times are used, it does not cause significant damage to biological cells and tissue;
(3) It can be used under a wide range of conditions such as varying temperature or pressure;
(4) Typical "background" species such as carbon dioxide and water do not significantly interfere with spectra, as they have weak Raman scattering;
(5) It allows the investigation of samples in physiological conditions, therefore lengthening the time period for measurements and making it possible to experiment in real-time.

For any application, the lack of sample preparation needed prior to analysis with Raman spectroscopy is one of the greatest advantages of the technique. This allows it to be a very rapid analytical technique, leading to high quality data in very short periods of time. Furthermore, Raman scattering originates from the surface of a

sample (typically no deeper than several hundred microns), so there is no concern with sample thickness, size or shape.

Raman spectroscopy can be used for a variety of purposes. The technique is often used as a qualitative or identification tool, as it provides exceptional chemical specificity. A Raman spectrum contains a wealth of analytical information and no two molecules will give the same one. Raman spectroscopy also has a greater sensitivity to chemical functional groups not seen strongly by other similar methods; as discussed in the previous section the selection rules governing the technique require a change in the polarisability of a molecule in order to be Raman-active, a condition that is unique to Raman spectroscopy. In addition, the intensity of scattered light is related to the amount of material present, allowing Raman spectroscopy to be used in quantitative applications.

As with any scientific technique, Raman spectroscopy also has its limitations. The most significant disadvantage of Raman spectroscopy is the interference it suffers from fluorescence. This phenomenon originates from different mechanisms to Raman scattering; however, they can occur together. Fluorescence is broad and more intense than Raman scattering, often overwhelming it. There are ways to avoid such interferences, as discussed in the following chapter, but the potential for fluorescence must always be considered during applications of Raman spectroscopy. Other disadvantages of Raman spectroscopy include equipment cost and the sensitivity of the technique. The Raman Effect is very weak, therefore efficient collection and detection of scattering requires sensitive and highly optimised instrumentation.

4.2 Surface-enhanced Raman spectroscopy

4.2.1 Discovery and recognition

Despite its many advantages over other methods of material characterisation, Raman spectroscopy is a fairly inefficient technique with small scattering cross-sections and diffraction-limited spatial resolution. These issues can be overcome by a more sensitive Raman spectroscopy method called SERS, which has great potential as an analytical tool for scientific research.

The effect that underlies SERS was discovered in 1974 by Fleischmann *et al.* [54], who detected enhanced Raman scattering from pyridine adsorbed on electrochemically roughened silver. However, the large signal was attributed to the number of molecules on the surface and not recognised as a major enhancement effect. It was not until 1977 that the effect was explained correctly, when two groups independently noted that the concentration of scattering species could not account for the increase in signal. In addition, each group suggested a mechanism for the effect. Jeanmarie and Van Duyne observed scattering of about 5 to 6 orders of magnitude greater than that achieved previously by conventional Raman spectroscopy and attributed this to an electromagnetic effect [55]. Meanwhile, Albrecht and Creighton proposed a charge-transfer effect for the enhancement they detected [109]. These scientists were the pioneers of SERS and their theories are still accepted today as the explanation for the technique.

4.2.2 Enhancement of Raman scattering

SERS exploits the enhancement of Raman scattering that occurs when a material is in close proximity with a rough, metallic surface (Figure 4.6). Molecules adsorbed on metal surfaces can have an unusually large scattering cross-section depending on the chemical nature of adsorbed molecules and the type, structure and morphology of the metal surface. For the effect to work efficiently, it requires a surface with a high curvature. This has led to the development of a variety of metallic nanoparticles and nanostructured surfaces for activating SERS [110-112].

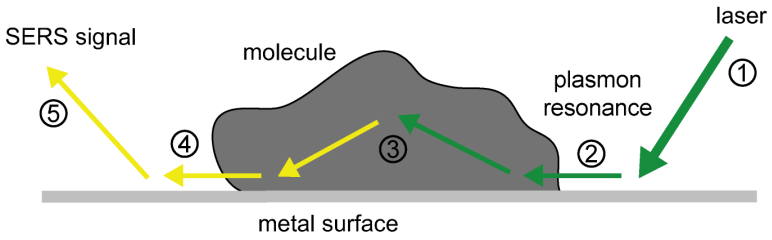

Figure 4.6: SERS process (1) laser light incident on the metallic substrate (2) excitation of surface plasmon resonance (3) light scattered by the molecule (4) Raman scattered light transferred back to plasmons and (5) scattered into air.

The magnitude of electric field enhancement depends significantly on the optical properties of the metallic surface and how these properties vary as a function of

wavelength. To optimise the SERS effect, the excitation and Raman-shifted wavelengths should coincide with the localised surface plasmon resonance of the metal structures employed to activate the enhancement [113]. Surface plasmons are collective electronic excitations that occur at the surface of metals and it is the coupling of the excitation light with these plasmons that leads to the high intensity of scattering obtained with SERS. Therefore maximum enhancement occurs when both the excitation and scattered electric fields are in resonance with the surface plasmons of the metal.

Most SERS studies employ gold, silver or copper, as the excitation of the localised surface plasmons of these metals occur in the visible region of the electromagnetic spectrum. For instance, silver is known to provide the greatest enhancement at mid-visible wavelengths as this is where its localised surface plasmon resonance lies, whilst gold and copper provide enhancement at red and near-infrared wavelengths for the same reason. Furthermore, the exact position of plasmon resonances can be tuned to achieve maximum enhancement with a certain setup by varying the shape and size of the metallic surface (Figure 4.7) [114].

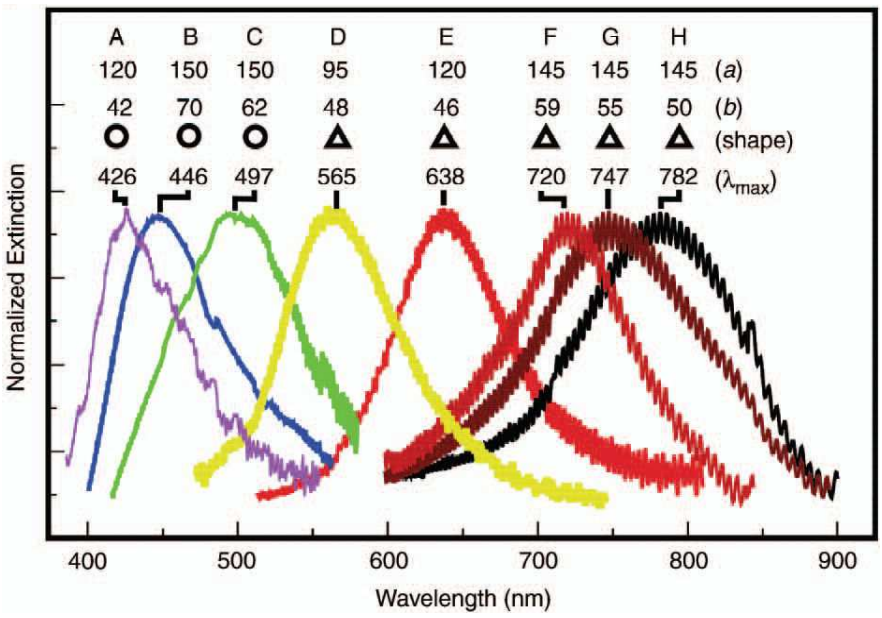

Figure 4.7: Size- and shape-tunable localised surface plasmon resonance spectra of various silver nanoparticles (labelled A–H). The wavelength of maximum extinction λ_{max} is changed by varying the in-plane width *a* and out-of-plane height *b* of the nanoparticles [113].

SERS has great potential for ultrasensitive detection and characterisation of molecules, especially for samples that are small or have weak Raman scattering. Often the enhancement gained with SERS is not distributed uniformly over the metallic surface providing the effect but tends to be spatially localised into so-called "hot-spots" [115-117]. At these locations unexpectedly large scattering cross-sections occur, corresponding to enhancements up to about 10^{14} [118]. In some cases this is a limitation to the technique, most notably for chemical imaging of non-uniform samples such as lipid microdomains. However, this level of enhancement is great enough to allow the detection of single molecules [119, 120]. In addition, SERS can provide lateral resolutions better than 10nm [121, 122], which is around two orders of magnitude below the diffraction limit. The technique is also known to strongly quench fluorescence, arising from the adsorption of molecules on a metallic surface.

4.2.3 Electromagnetic or Chemical?

There is still much debate over the origin of SERS enhancement. Most literature points towards an electromagnetic effect being responsible [123, 124]. In this case, the belief is that the enhancement of Raman scattering from a material occurs due to a local electromagnetic field enhancement that is provided by a nearby optically active metallic nanoparticle (Figure 4.8). As opposed to a dielectric particle that will reduce the electric field around itself, a metallic particle is capable of increasing it. This particle has free electrons. Therefore in an electric field it will polarise in the direction of the incident field to produce an internal electric field E_{local} that is additive to the incident electric field E_0. This is due to the electronic structure of the particle and the roughness of the metallic surface; conduction electrons in the surface of the particle are excited by the incoming light, generating a surface plasmon resonance. The result is a total electric field E_{total} near the surface of the particle that is larger than the incident field. The key to SERS, however, is not this initial enhanced field near the particle. The crucial step is that this large field on the surface of the particle induces an even greater field inside the particle, which in turn amplifies the external field further. This effect does not require direct contact between the molecule and metallic surface and occurs over a distance of nanometres; the dipole field induced in

a metallic particle varies as the inverse cube of the distance to the centre of the particle r, given by

$$E_{local} = E_0 + \frac{P}{2\pi\varepsilon_0 r^3} \tag{4.11}$$

where ε_0 is the permittivity of free space.

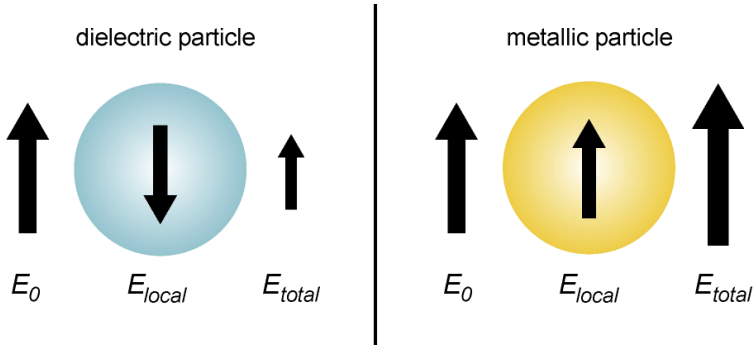

Figure 4.8: Illustration of the effect dielectric and metallic particles have on an incident electric field.

This is a relatively long-range effect compared to the other theory put forward to explain SERS enhancement. This is known as chemical enhancement, for which there is much less experimental evidence and thus fewer believers [123, 125]. The mechanism underlying this theory associates the scattering process with a chemical interaction between the molecule and the metal surface (Figure 4.9). It is described in terms of an overlap of the metal and adsorbate electronic wavefunctions; the enhancement of Raman scattering originates from a heightened molecular polarisability that is a result of charge-transfer or bond formation between the metallic surface and the adsorbate material. It is a very short-range effect that depends on the geometry of the absorption site and the energy levels of the adsorbate molecules.

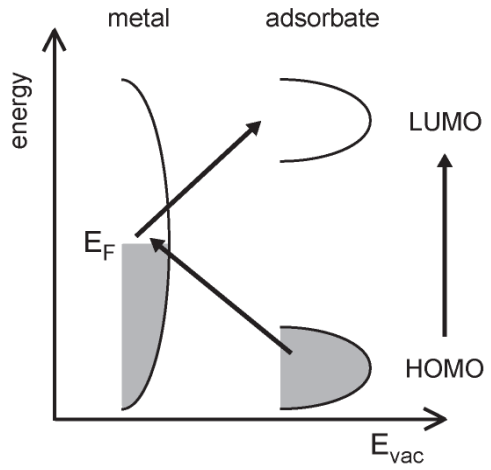

Figure 4.9: Typical energy level diagram for a molecule adsorbed on a metal surface. The occupied and unoccupied molecular orbitals are broadened into resonances by their interaction with the metal states; orbital occupancy is determined by the Fermi level E_F (possible charge transfer excitations are shown).

Mathematically, the possibility of both electromagnetic and chemical enhancement is evident from the relationship in Equation 4.3, which demonstrates that the induced electric dipole moment of a metallic nanoparticle is directly proportionally to both its polarisability and the incident electric field. In addition, the intensity of scattering is known to vary proportionally with the square of the electric dipole moment. Therefore either of the suggested theories could correctly explain the huge enhancement of scattering obtained with SERS. Consequently, there has been some recognition that they both play a part in the overall effect, with electromagnetic enhancement being the more dominant mechanism and chemical enhancement only contributing around an order or two of magnitude [126].

4.3 Tip-enhanced Raman spectroscopy

Alongside the numerous benefits of SERS, the technique has its disadvantages. Firstly, the requirement of a rough, high curvature surface may cause compatibility problems with some samples. Secondly, the technique is restricted to the coinage metals when working at visible wavelengths. Finally, the ability of SERS to chemically image a sample is hindered by the possible variation in enhancement across the structure of the metallic surface. All these limitations can be overcome with TERS, a slightly modified version of SERS.

In TERS, a sharp metal tip is employed as the metallic surface that activates the enhancement of Raman scattering (Figure 4.10). This tip is usually a scanning probe microscopy (SPM) tip coated in silver or gold, onto which the excitation light is focused as it is brought into close proximity with the sample under investigation. The technique is based on the same mechanism as SERS; localised surface plasmons are excited in the apex of the tip to produce enhanced electric fields between the tip and the sample. Only the molecules situated directly underneath the tip in the enhanced field give rise to intense Raman scattering. The tip acts as an amplifying antenna for the incoming and outgoing electromagnetic waves, the enhancement reducing to nothing as the tip is retracted.

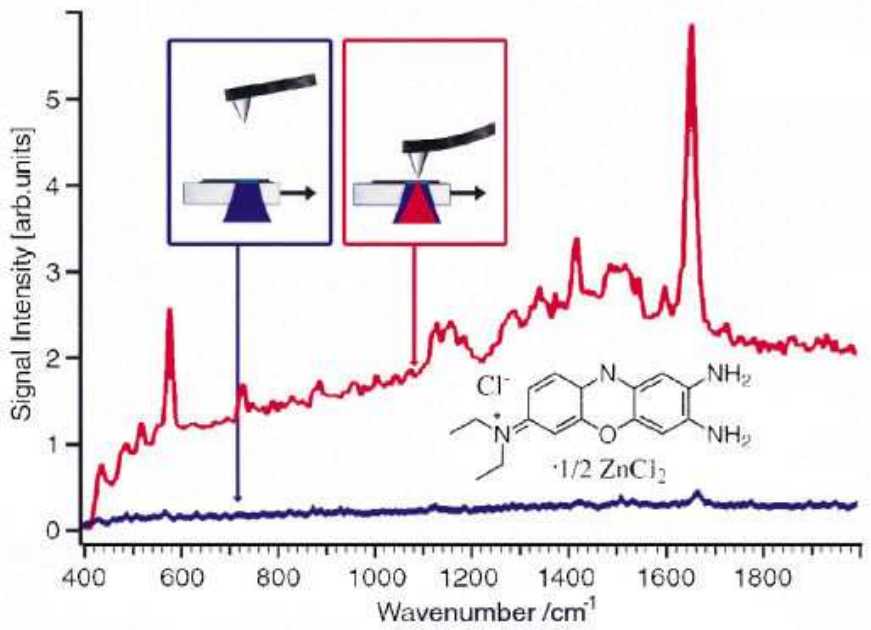

Figure 4.10: TERS spectra of brilliant cresyl blue dispersed on a glass support measured with the tip of a silver-coated AFM probe in contact with and retracted from the sample [69].

The technique originates from 1985, when Wessel had the idea to scan the surface of a sample with a silver nanoparticle controlled by piezoelectric crystals [127]. However, it was difficult to control the distance between particle and sample with this setup and it was suggested that much easier control could be achieved by employing a metal scanning tunnelling microscopy (STM) tip for electric field enhancement. This prediction was realised 15 years later in 2000, when Zenobi *et al.* combined a Raman spectroscopy system with an atomic force microscope (AFM) to form the first TERS setup [69]. In an inverted configuration, a silver AFM tip was

aligned over a thin layer of dye dispersed on a glass coverslip and illuminated from below (as shown in Figure 4.10). This arrangement is still in common use today; however, it only allows transparent samples to be studied. Therefore one major development in TERS has been the modification of the experimental setup to illuminate the sample at 60° to the AFM or STM tip [128].

TERS is one of the most significant advances in nanoscale chemical analysis of all time. The combination of SPM techniques and Raman spectroscopy allows the correlation of topographical and chemical information of the same region of a sample, achieving one of the long-awaited goals of surface science. Theoretical studies have predicted enhancements on the order of 10^8 [70] and the technique has demonstrated great potential for imaging biological materials [71]. However, as with any experimental method, TERS has its limitations. These include issues with the reproducibility of data due to the high variability of probes and also contamination of spectra from other materials on the probe.

Chapter 5

Development and characterisation of an RMS setup with integrated AFM

The development and characterisation of an RMS setup with integrated AFM for studying SLBs is described here, which combines the benefits of Raman spectroscopy with the high spatial resolution of confocal microscopy and capabilities of AFM. All aspects of the design, purchase, alignment, calibration and optimisation of this system are detailed. This includes an assessment of its spatial resolution and how the axial resolution of the setup can be improved by the inclusion of a confocal system.

5.1 Introduction

Raman spectroscopy allows the characterisation and identification of materials with high chemical specificity. It provides extensive information at the molecular level based on vibrational fluctuations of components within a material to reveal its physiochemical makeup. Optical microscopy techniques such as confocal microscopy are used extensively in scientific research to image materials and

processes on the micro- and nanoscale, beyond what is visible with the naked eye. The combination of these two methods is Raman microspectroscopy (RMS), which makes it possible to investigate the molecular structure and chemical composition of a material that is too small to be studied using conventional Raman spectroscopy.

In the past, the adoption of Raman spectroscopy methods for routine analysis of materials, biological or otherwise, has been hindered by the high cost and complexity of the instrumentation required. However, in recent years this situation has changed with the production of pieces of equipment such as dielectric edge filters, holographic gratings, long-wavelength excitation lasers and highly sensitive charge-coupled devices (CCDs). These technological advances are making the technique more accessible than ever before and have led to major developments in its efficiency, sensitivity and applications.

5.2 Aims

A Raman spectroscopy system has been built in-house. This involved the design, purchase, alignment and calibration of all the optical, electrical and mechanical components of the system. The experimental setup has been continually developed to optimise what can be achieved with the instrumentation, the overall aim being to gain a high level of sensitivity.

The first step in developing a high sensitivity optical system is to ensure it can detect the correct level of signal necessary to carry out successful Raman spectroscopy. Raman scattering is a very weak effect and is often drowned out by a large background, particularly in the case of small or biological samples that have minimal scattering. Another issue to be addressed is noise, random interference that causes extra fluctuations to appear in a spectrum alongside the Raman signal. Therefore, the focus in this part of the development work has been to collect the maximum amount of Raman scattering possible with the system whilst minimising any background and noise. This balancing of Raman scattering and unwanted signal results in a quantity known as signal-to-noise ratio, which should be high for an optimised Raman spectroscopy system.

The collection of useful signal is limited by the number of detected Raman photons. This is determined by:

(1) Transmission of light, which is the fraction of light intensity collected at the input of an optical system that successfully reaches the output. Ideally this is the product of the optical efficiencies of all components in the optical path. However, in reality the fraction is less than this due to blocked or lost light, such as light that falls outside the acceptance aperture of an optical element.
(2) Etendue or optical throughput G, which characterises the ability of an optical system to accept light. It is the combined measure of the area of the emitting source (i.e. the sampling size) A and the solid angle into which light is emitted from the sample Ω, given by

$$G = A\Omega \tag{5.1}$$

This is a limiting factor. Sample image area and solid angle vary throughout an optical system as the collected light is magnified and focused. However, the étendue of an entire optimised optical system remains constant, as it cannot exceed the minimum $A\Omega$ product of the system.

Once the Raman scattering has been collected, there is the risk of it being totally hidden by background signal. Saturation can arise from numerous factors:

(1) Light of wavelengths outside the spectral range of interest can fall onto the detector, adding a broad background or structured artefacts to the spectra. This is known as stray light and can be in the form of random scattering originating from misaligned optical elements or directional light such as reflections from overfilled optical elements and grating ruling defects.
(2) The excitation light of an optical system can totally overwhelm any useful signal if it is not filtered out efficiently, since it can be 10^4-10^{12} times more intense than Raman scattering.
(3) Fluorescence is a phenomenon that occurs alongside Raman scattering, but competes with and often overwhelms any useful signal. It is an absorption emission process in which an incoming photon is absorbed by an excited

molecule, causing the molecule to relax back to the fundamental electronic state and emit a photon with a longer wavelength from the lowest vibrational level of an excited electronic state. If the excitation photon does not provide sufficient energy to the molecule, the required electronic transition to produce fluorescence will not take place. However, if fluorescence is successfully generated from this mechanism, it is broad and often more efficient and intense than Raman scattering.

The second step in developing a high sensitivity optical system is to obtain good spatial and spectral resolution. The optimisation of these aspects of the setup enables the detection of Raman scattering from a very small sample volume and the accurate separation of adjacent peaks in its spectrum. The spatial resolution of an optical system is diffraction limited by the microscope objective, which determines the collection volume of light from a sample. This can be greatly improved by the addition of a confocal system, upgrading a conventional Raman spectroscopy setup to an RMS setup. Spectral resolution is limited by the focal length of the spectrometer and the dimensions of the diffraction grating and detector. Ideally, a sample emitting a photon at a particular wavelength should appear on the emission spectrum as a sharp line at precisely that wavelength. However, in reality spectrometers produce an apparent spectral broadening of light, even the monochromatic light of a laser. Depending on the extent of this broadening, there is a limit to how close two Raman bands can be before they cannot be differentiated from each other and are just seen as one large peak. Both spatial and spectral resolution involve a trade-off between sensitivity and signal intensity, since resolution is improved at the expense of spectral range and signal strength.

Further improvement to the overall sensitivity of a Raman spectroscopy setup, in terms of both signal intensity and resolution, can be made by introducing scattering enhancing techniques such as surface-enhanced Raman spectroscopy (SERS) and tip-enhanced Raman spectroscopy (TERS). However, initially the focus is on optimising the fundamental instrumentation and experimental setup.

5.3 Instrumentation and experimental setup

5.3.1 Excitation source and Rayleigh filters

A major component of a Raman spectroscopy setup is the excitation source. Commonly this is a continuous wave laser, which provides a highly monochromatic and linearly polarised beam of light often with a bandwidth of just 0.1cm^{-1}. These lasers are ideal for use in an RMS setup, since a single focused beam of a specific wavelength can provide a high amount of power to a small sample area.

The laser used in the work described in this thesis is a diode-pumped solid state laser, operating at a wavelength of 532nm and a maximum power of 20mW (Laser 2000). It is a class 3B, continuous wave laser that is compact, stable and efficient, with a spectral line width of less than 0.0001nm and a beam divergence of less than 1.5mrad. A schematic of this type of laser is shown in Figure 5.1. Firstly, a powerful 808nm wavelength infrared diode laser pumps a neodymium-doped yttrium orthvanadate crystal to produce 1064nm wavelength light. This light is frequency doubled using a non-linear optical process in a potassium titanyl phosphate crystal to produce 532nm wavelength light, which is then expanded and filtered to provide the resultant laser beam.

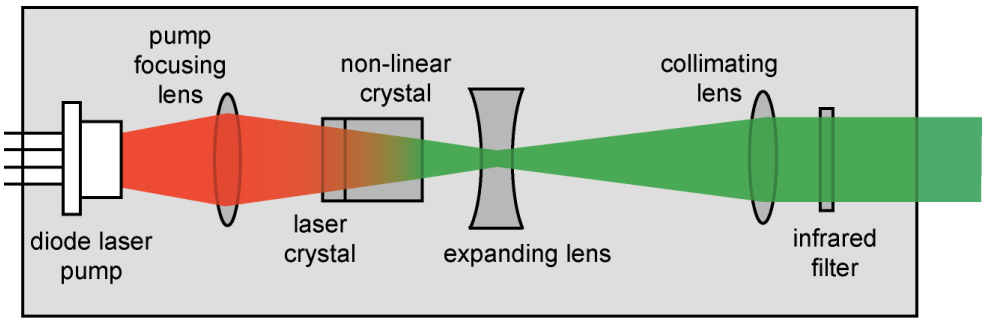

Figure 5.1: Schematic of a typical diode-pumped sold state laser.

An important safety consideration when using a laser is its maximum permissible exposure *MPE* [129]. This is the level of laser radiation that a person can be exposed to without hazardous effects or biological changes in the eye; exposure to laser energy above the maximum permissible exposure can result in tissue damage. Maximum permissible exposure levels are determined as a function of laser

wavelength, exposure time and pulse repetition (if any). Generally, the longer the laser wavelength and the shorter the exposure time, the higher the *MPE*.

For an exposure time t of between 5×10^{-5} and 10s,

$$MPE = 18t^{0.75} Jm^{-2} \tag{5.2}$$

Assuming the human blinking mechanism to be about 0.25s, this gives a maximum permissible exposure of $6.36 Jm^{-2}$. The associated energy of a laser is given by

$$E = Pt \tag{5.3}$$

For a laser power P of 20mW, this expression provides a value of 5mJ for E. Finally, the exposure of a laser e can be calculated from

$$e = \frac{E}{A} \tag{5.4}$$

The human eye has a pupil diameter of up to 7mm. However, the laser used in this work has a beam diameter of only 4mm, so this provides the area of exposure A. Therefore the expression above gives an exposure of $398 Jm^{-2}$. This means that this laser exceeds the maximum permissible exposure by a factor of almost 63, demonstrating that it falls into laser class 3B. A class 3B laser is hazardous if the eye is exposed directly, but diffuse reflections such as from paper or other matte surfaces are not harmful. Therefore protective eyewear is required at times when accidental direct viewing of the laser beam may occur and the laser must be equipped with a key switch and a safety interlock.

Laser power and wavelength of light are two important properties to consider when choosing a laser for a Raman spectroscopy system. Firstly, the intensity of Raman scattering is governed by the v^4 rule as demonstrated in Equation 4.10. It is evident from this expression that a lower wavelength laser is capable of exciting light of a higher intensity than a high wavelength laser of the same power. Secondly, a laser operating in the visible range of the electromagnetic spectrum means that

fluorescence could be a problem, even at relatively low laser power. Raman scattering is inherently weak and difficult to distinguish if it occurs alongside a large fluorescent background. Fluorescence is difficult to avoid with some samples; however, its effect can be reduced by proper filtering, alignment and focusing of the laser beam. The laser beam itself must also be filtered, as it is much higher in intensity than any Raman scattering it excites. Numerous optical elements were placed in the system for this purpose.

The laser is initially directed through a line filter (Semrock). This filter is a narrow bandpass filter centred on the resonance of the laser, which passes the 532nm laser line whilst blocking any surrounding noise such as background plasma and secondary emissions (Figure 5.2a). Then following irradiation of the sample, a notch filter (Semrock) is placed in the optical path. This filter is required to remove any laser light that has been reflected back from the sample towards the spectrometer, occurring alongside the Raman scattering. A notch filter cuts light either side of the laser wavelength in a way that allows simultaneous measurement of Stokes and anti-Stokes scattering (Figure 5.2b). It can be thought of as a bandstop filter rather than a bandpass filter, which provides extremely high blocking of the laser line with excellent tunability and a bandwidth for accommodating variable laser lines.

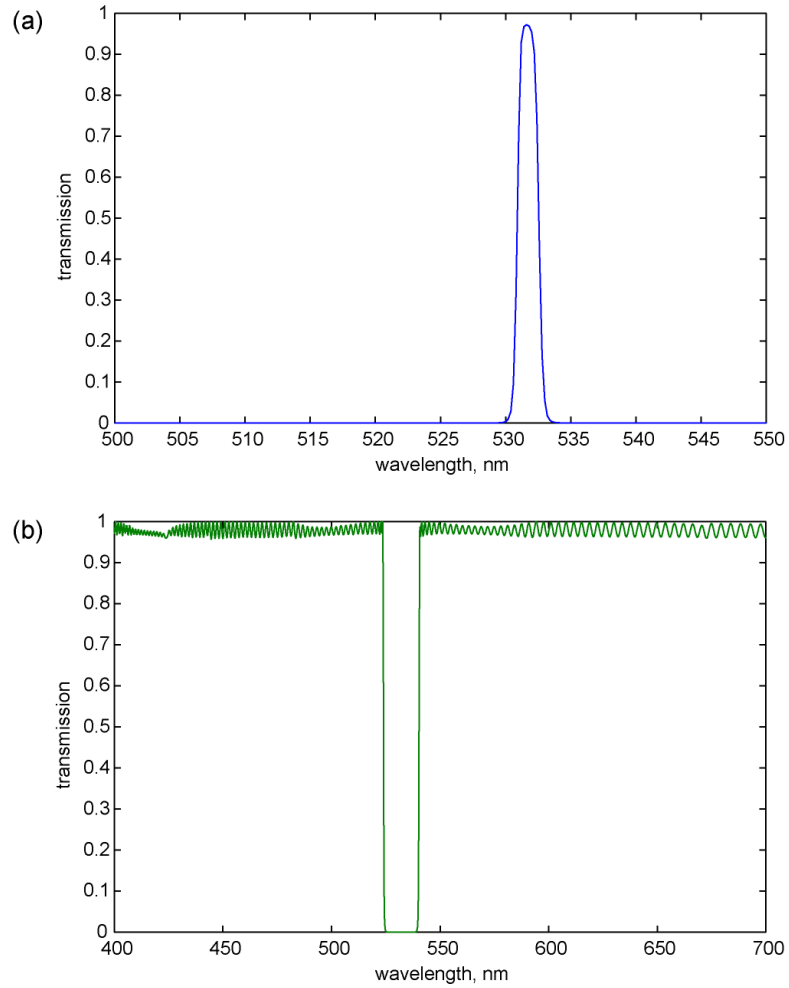

Figure 5.2: Transmission curves of the (a) line filter and (b) notch filter for 532nm excitation (data from Semrock).

The positioning of the notch filter within this setup means that it is also required to act as a mirror, directing the laser beam towards the sample. This is possible due to the tunability of the filter. Notch filters are optimised for use with light at or near normal incidence. At large angles of incidence the position of 0% transmission shifts to shorter wavelengths. However, at angles of incidence below about 5° the filter still provides ~100% reflection at the laser wavelength.

5.3.2 Microscope and objective

The microscope used in this Raman spectroscopy setup is an inverted compound microscope (IX71, Olympus). This microscope provides the optimal arrangement for a Raman spectroscopy setup, since it enables the measurement of Raman scattering from biological samples that are immersed in liquid.

The microscope contains a mirror mounted in a cube directly below the objective that simultaneously sends the laser up towards the sample and directs the resultant scattering out of the microscope towards the spectrometer. This mirror is an enhanced silver reflective mirror (Chroma Technology). It reflects incoming light at a 45° angle of incidence with an efficiency of around 99% over the spectral range of interest. This allows a small amount of laser light to pass through the mirror from the sample to an optical camera for alignment purposes (Figure 5.3). In order to obtain an image of the sample at this camera, the mirror can be temporarily shifted out of position.

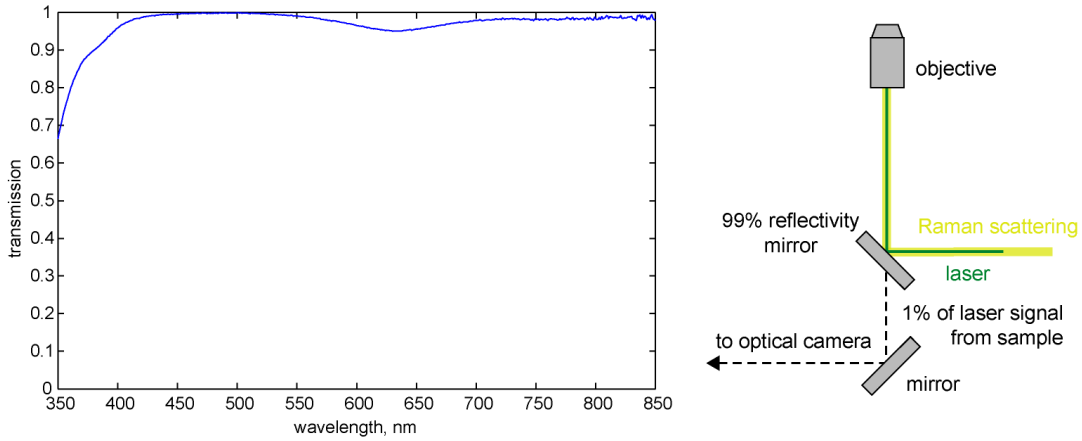

Figure 5.3: Transmission curve of the enhanced silver reflective mirror, with an illustration of its placement in the microscope and function (data from Chroma Technology).

For Raman spectroscopy, the most important part of the microscope is the objective. After alignment of the laser into the microscope, the objective focuses the laser beam onto the sample and then collects the resultant Raman scattered light. Efficient alignment and focusing of the laser beam is essential in exciting a small area of the sample with the maximum power possible from that laser. Similarly, it is desirable to collect all the Raman scattering from this area of the sample in order to obtain high intensity, high resolution signal.

The most important aspect of the objective is the angular aperture of the light cone captured by it. This determines the amount of light that can be collected from the sample, which is especially important in Raman spectroscopy since Raman scattering is such a weak effect. There are two factors that have an impact on the amount of

light collected by the objective; the numerical aperture of the objective and the refractive index of the medium between the sample and the objective.

The numerical aperture of an objective *NA* defines its light-gathering ability and is given by

$$NA = n \sin\theta \tag{5.5}$$

where n is the refractive index of the medium between the sample and the objective and θ is the angular aperture. From this expression, it can be seen that the numerical aperture of an objective varies proportionally with both n and $\sin\theta$. In terms of Raman spectroscopy, these two values should be optimised to allow as much scattered light as possible to be collected from the sample in order to provide a high signal-to-noise ratio Raman spectrum.

Most objectives have relatively low numerical apertures and are designed to be used dry with only air as the medium between the objective front lens and the sample. The maximum theoretical numerical aperture obtainable with air is 1.0. However, in practice it is virtually impossible to produce a dry objective with a numerical aperture above 0.95. In addition, these objectives do not allow for the sample to be supported on a substrate such as a glass coverslip. The presence of this material introduces a new refractive index between the objective and sample and variation in its thickness can degrade the performance of an objective. This effect is negligible for dry objectives that have a numerical aperture of less than 0.4. However, it becomes significant at numerical apertures exceeding 0.65, for which fluctuations in the substrate thickness as small as 0.01mm can introduce spherical aberrations. Many objectives are now available with a correction collar that allows adjustment of the central lens group position to coincide with changes in substrate thickness. However, a more effective solution to this problem is to introduce a medium other than air between the objective and sample that is closer in refractive index to the support material. This is known as an immersion medium and many objectives are now made to be used with either water or oil at the objective front lens. These immersion media practically eliminate spherical aberrations and image degradation from the presence of a substrate, whereby light approaching the objective at wide angles no

longer undergoes refraction and is more readily collected. Consequently, the numerical aperture of water- and oil-immersion objectives is dramatically increased from that of dry objectives. The objective used in this Raman spectroscopy setup is a 60× water-immersion objective, with a correction collar and high numerical aperture of 1.2 (UPlanSApo60X/1.2W, Olympus) (Figure 5.4).

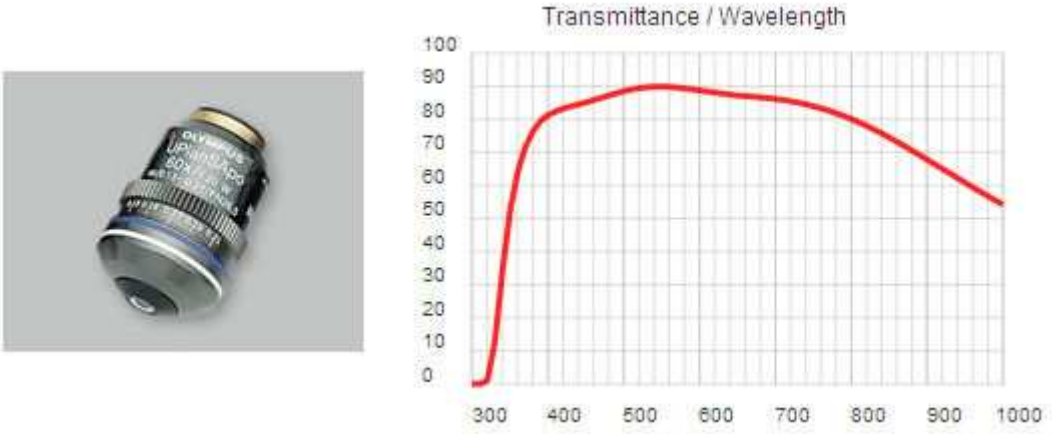

Figure 5.4: Image of the objective used in this setup and its transmission curve (both from Olympus).

The high numerical aperture of this objective not only determines its capabilities for collecting scattering from the sample, but also for illuminating the sample with the excitation source. It means that the objective is able to provide a small, high energy laser spot at the sample, optimising the intensity of Raman scattering that can be obtained. In Equation 5.5, θ can also be thought of as the divergence of the laser beam from the objective to its focus. As the laser beam has a Gaussian profile, numerical aperture can be related to its minimum spot diameter D by [28],

$$NA = \frac{2\lambda_0}{\pi D} \tag{5.6}$$

where λ_0 is the wavelength of the laser light. However, if the objective is underfilled, its numerical aperture is effectively reduced. For this reason, the equation above can also be expressed in terms of the diameter of the laser beam D_0 entering the objective to provide a more realistic value for the minimum spot size, given by

$$D = \frac{4\lambda_0 f_{obj}}{\pi n D_0} \tag{5.7}$$

where f_{obj} is the focal length of the objective, which is the ratio of the microscope tube length to its magnification. The microscope chosen for this setup has a tube length of 180mm and the objective has a magnification of 60×, therefore its focal length is 3mm. This means that for a laser beam diameter of 4mm, the objective can produce a spot size of 382nm in diameter. This translates to an area of about 1×10^5nm^2. Therefore at full power, the laser can provide an energy density of around 10^{11}W/m^2 or 10^{-4}mW/nm^2 to the sample.

5.3.3 Collection lens, spectrometer and detector

A lens is placed after the microscope to focus the Raman scattering from the sample into the spectrometer and onto the detector (Figure 5.5). The lens is positioned in front of the entrance slit of the spectrometer, collecting the light from the sample and focusing it though the slit without overfilling the optics inside the spectrometer. A factor to be considered when choosing this lens is f-number *f/#*, which expresses the diameter of the lens *D* in terms of its focal length *f* and is given by

$$f/\# = \frac{f}{D} \tag{5.8}$$

The microscope and spectrometer are placed as far away as possible in this setup, so that the light from the microscope is always essentially parallel when it reaches the collection lens. This means that for efficient focusing of Raman scattering into the spectrometer and onto the detector the lens is required to have the same f-number as the spectrometer, which in this case is f/4.

Figure 5.5: Focusing light from the microscope into the spectrometer.

A variety of collection lenses were positioned in the setup and assessed for their compatibility with the spectrometer, in terms of their focusing capabilities and the intensity of Raman scattering detected at the end of the system. By monitoring these experimental aspects, a lens with a diameter of 12.7mm and focal length of 30mm was found to be most suitable for the setup (Thorlabs, UK). However, its suitability can also be determined theoretically by considering the light approaching the lens from the microscope. The objective used in this setup has a focal length of 3mm, previously calculated from its tube length and magnification. Therefore the beam diameter of light coming from the microscope is 5.4mm, determined by the diameter of the back aperture of the objective,

$$d = \frac{2 f_{obj} NA}{n} \tag{5.9}$$

From Equation 5.8 the collection lens chosen for this setup has an f-number of 5.54, fairly close to that of the spectrometer.

The spectrometer is a vital part of a Raman spectroscopy setup, as it converts the scattering from a sample into a measurable mechanically-selectable narrow band of wavelengths of light. The spectrometer used in this setup is a double Czerny-Turner spectrometer with a focal length of 303mm (Shamrock, Andor Technologies) (Figure 5.6). Focused light enters the spectrometer through an entrance slit, which is capable of widths from 10µm to 2.5mm. The ideal slit width for Raman spectroscopy measurements with this setup was found to be around 50-100µm, which provided a good compromise between collecting a large amount of scattering from the sample whilst minimising background signal.

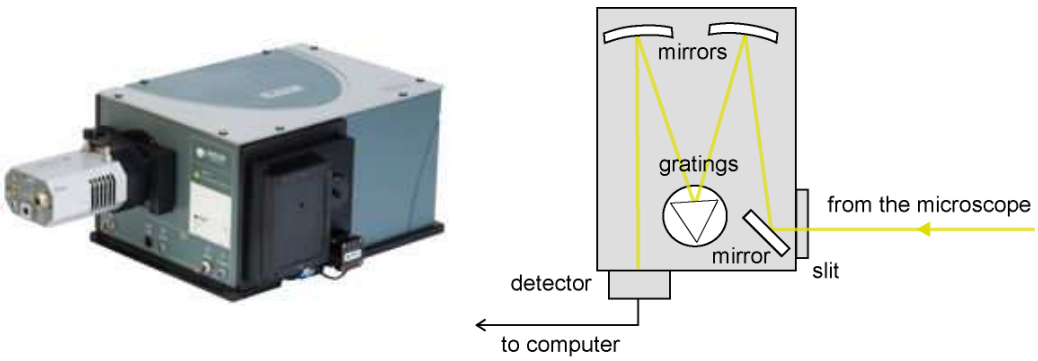

Figure 5.6: Image and schematic of the spectrometer.

The light is then directed by two mirrors from the entrance slit onto a grating. The spectrometer contains two diffraction gratings on a turret (Figure 5.7). These gratings act as a dispersing element, spatially spreading the light scattered from the sample as a function of wavelength. The gratings are ruled and blazed and concentrate a limited region of the spectrum into any order other than the zero order. They are manufactured to produce maximum efficiency at a designated wavelength known as the blaze wavelength. This wavelength is dependant on the groove geometry of the ruling and is the point at which the angle of reflection from the groove face of the grating is the same as the diffraction angle. The efficiency of the grating decreases significantly away from this wavelength, necessitating the need for multiple gratings with different blazes to cover a wide wavelength range. The two gratings in this setup also have different rulings, which contribute to the spectral resolution of the system. There is a 600l/mm grating for times when it is necessary to detect a broad range of wavelengths but spectral resolution is not so important and an 1800l/mm grating for providing a much higher spectral resolution over a shorter wavelength range.

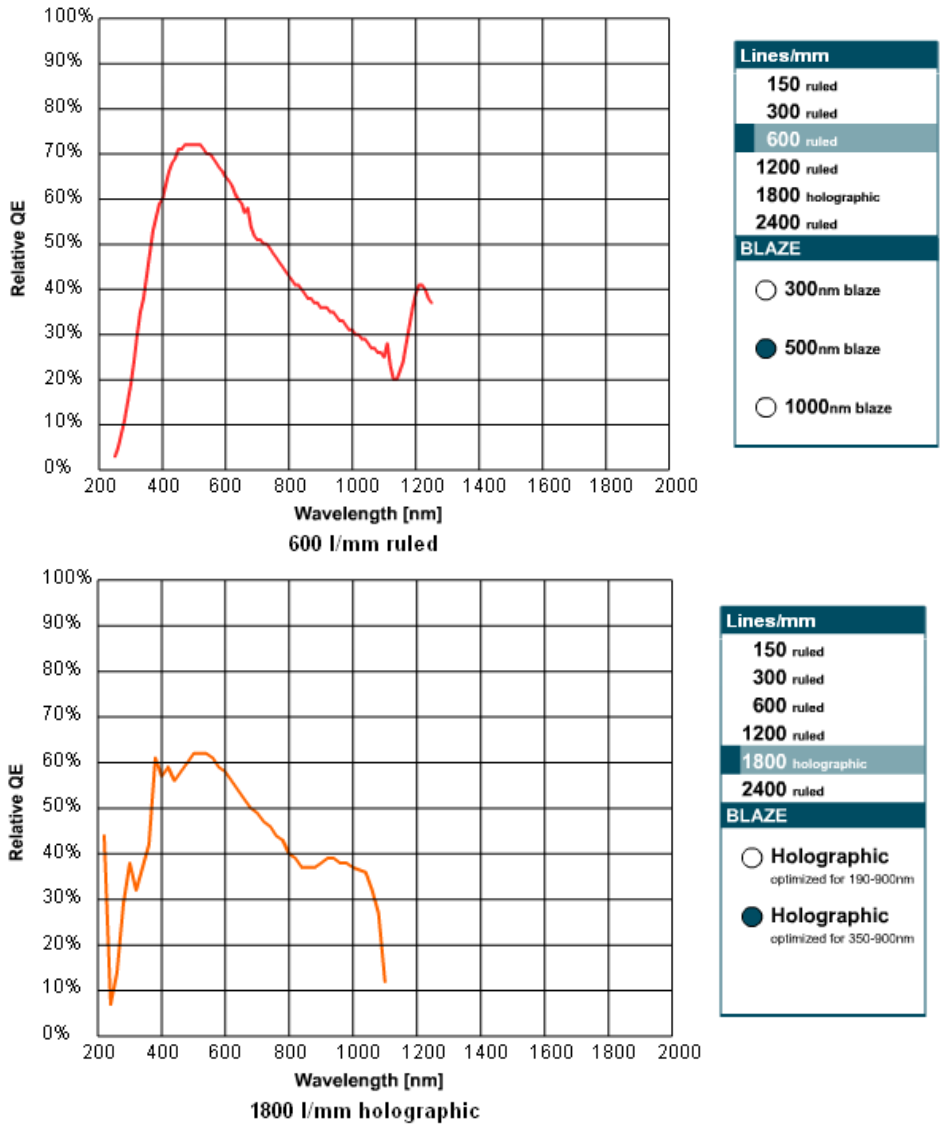

Figure 5.7: Efficiency curves of the two gratings used in this setup (from Andor Technologies).

Following the grating, the selected wavelengths of light are directed by another mirror onto the exit of the spectrometer in order to be detected. The detector used in this setup is a back-illuminated CCD (Andor Technologies) (Figure 5.8a). This device collects the light dispersed by the grating onto a 1024×128 array of 26×26µm pixels that are calibrated to transform the incoming time-domain waveform into a frequency, or Raman spectrum. The sensitivity of the CCD is measured in quantum efficiency, a value that varies over all wavelengths of light (Figure 5.8b). The sensitivity of the detector in this setup is particularly high, since the back of the chip is coated in thinned silicon that is etched to allow back-illumination. This is a popular choice in Raman spectroscopy systems, as the arrangement increases the

amount of light captured and therefore improves low-light performance. The CCD contains wavelength-conversion phosphors that absorb photon energy in the spectral range of interest and emit light within the spectral sensitivity region of the CCD. Ideally, a CCD would have 100% quantum efficiency over the entire spectrum. However, in reality a CCD is chosen that has maximum sensitivity over the desired range of wavelengths and gradually declines outside this range. In addition, CCDs do not have the same sensitivity from pixel to pixel nor across the whole chip.

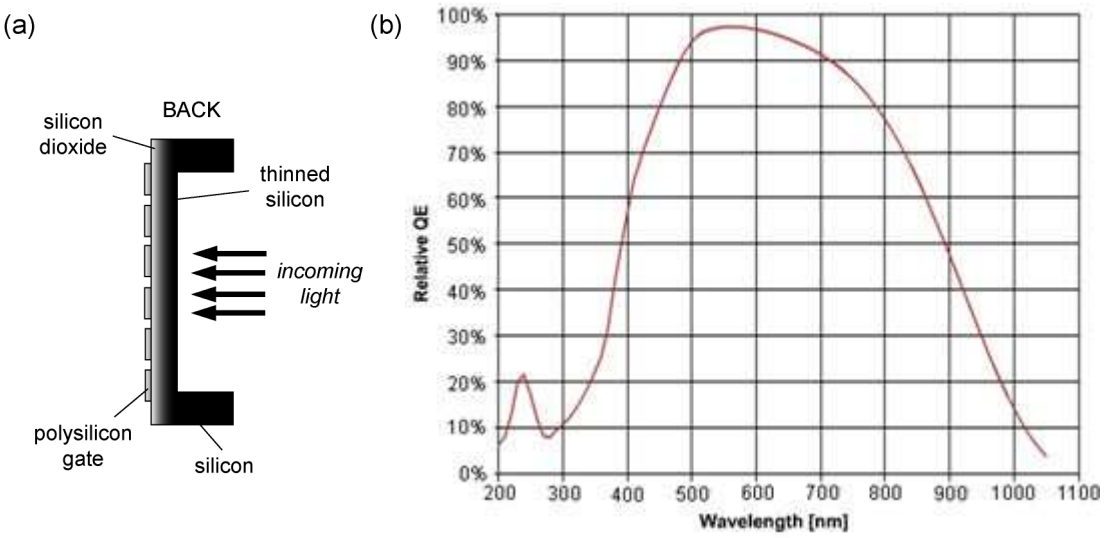

Figure 5.8: (a) Schematic and (b) efficiency curve of the CCD (curve from Andor Technologies).

As previously mentioned, a major focus of developing a Raman spectroscopy setup is obtaining spectra with good signal-to-noise ratio and the CCD plays a significant part in this. A CCD collects noise as well as useful signal, which is easier to prevent before recording spectra rather than trying to remove it after. Low readout noise as well as high quantum efficiency and sensitivity in a wide wavelength range allow detection of low levels of light. Background signal and noise can be reduced by using longer exposure time and multiple acquisitions. It is also optimal to not use the entire CCD chip. Proper focusing of the signal into the spectrometer and onto the detector makes it is possible to use as little as 10 tracks of the chip (Figure 5.9).

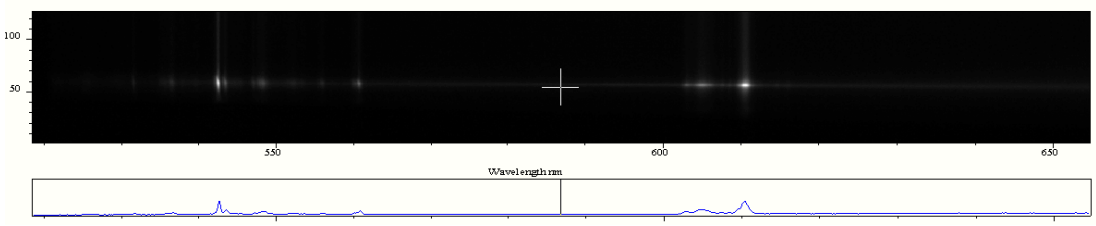

Figure 5.9: Raman signal from polystyrene focused onto less than 10 CCD tracks.

The CCD itself produces noise known as dark current, a slow and steady growth of unwanted signal generated by the heat inside the CCD. It can be lowered by thermodynamically cooling the chip via the Peltier effect, in which heat is transferred from the CCD chip to a heat sink through alternating layers of p-type and n-type semiconductor. In addition to keeping the temperature of the detector at around -70°C, it must be kept constant. Fluctuations in this value can cause Raman band positions to vary by as much as $3cm^{-1}$.

The CCD is connected to a computer for spectral acquisition. Data is collected by an accompanying piece of software, which also allows detailed control over all aspects of the spectrometer.

5.3.4 Alignment, focusing and calibration

Careful alignment and focusing is essential with any optical system, but particularly when dealing with such a weak process as Raman scattering. The alignment and focusing of the system is required in terms of the excitation of the sample and the collection of resultant signal from it. Good alignment of the laser into the microscope and onto the sample ensures that the maximum power available from that laser is focused into the smallest area possible. This will ensure the greatest excitation of the sample and in turn efficient collection of Raman scattering. Then good alignment of this scattering into the spectrometer and onto the CCD is important for focusing and collecting the entire signal whilst restricting background and noise.

Alignment is possible by following either the laser beam or an image from the microscope around the optical system and appropriately positioning and securing

each piece of optical equipment in the light path. This includes the laser, microscope, spectrometer, detector and every mirror, filter and lens. Firstly, the laser is aligned into the microscope through a system of mirrors onto the sample. The laser is aligned directly through the centre of the objective, so that when the focusing of the objective is varied the laser appears as concentric circles and is in focus when the sample is in focus (Figure 5.10). Alignment of the resultant scattering into the spectrometer, focused at the entrance slit and similarly on the CCD, is achieved by following an image from the microscope along this path (Figure 5.11). Proper alignment of this image makes it possible to focus the image onto a single pixel of the CCD chip with the collection lens. Finally, with the laser exciting the sample, this lens is finely tuned to position and focus the Raman scattering onto the CCD, eventually maximising signal.

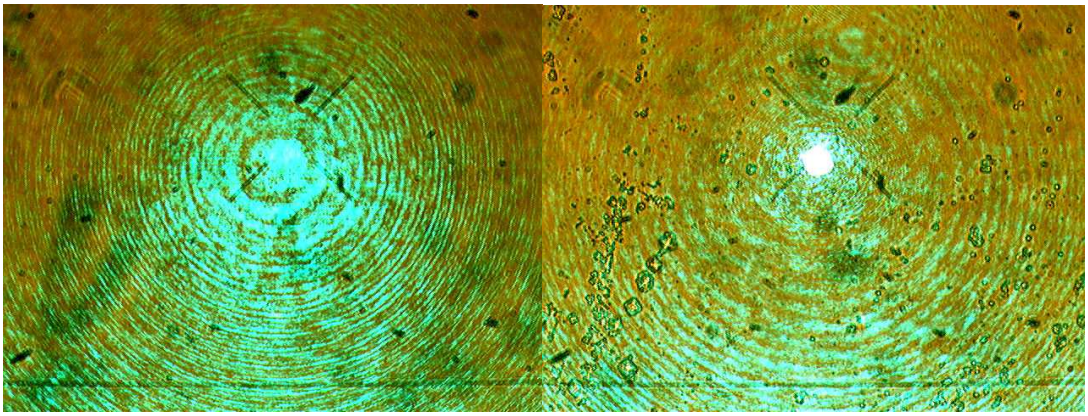

Figure 5.10: Optical images showing the focusing of the laser spot on the sample.

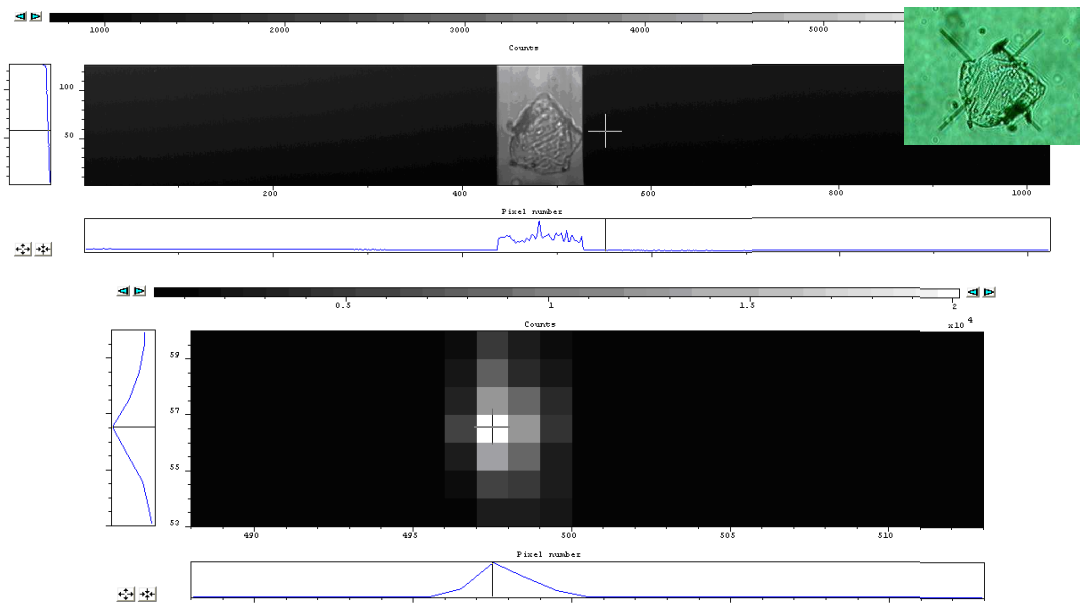

Figure 5.11: Aligning an image from the microscope (inset) through the entrance slit of the spectrometer onto the centre of the CCD, which can then be focused by the collection lens onto a single pixel.

Calibration is required to ensure that the light scattered from the sample is correctly represented on the detector. Samples with known Raman spectra that contain many peaks, such as polystyrene, are used to calibrate the grating and detector of the spectrometer. The spectrum of this standard sample is recorded, the pixels on which each Raman band occurs are assigned to the correct wavelengths and this spectrum is repeated to verify the calibration.

All Raman spectroscopy measurements are processed and analysed with Matlab (Mathworks, UK). Spectra are created from ASCII files imported into the Nova IN 1.1 Toolbox, software written by Dr Ioan Notingher for analysis of Raman spectroscopy data.

5.4 Combined AFM-Raman system

Further development of the setup involved the inclusion of an atomic force microscope (AFM) with tip-assisted optics module (Nanowizard II, JPK Instruments) (Figure 5.12) [42]. Previously an AFM was used alongside the setup to image and characterise samples before moving them to the Raman spectroscopy system. However, integrating an AFM into this system allows simultaneous measurement and

direct correlation of topographical, mechanical and chemical information about a sample. This is also important for investigating supported lipid bilayers (SLBs) in terms of confirming their presence and identifying regions of lipid microdomains.

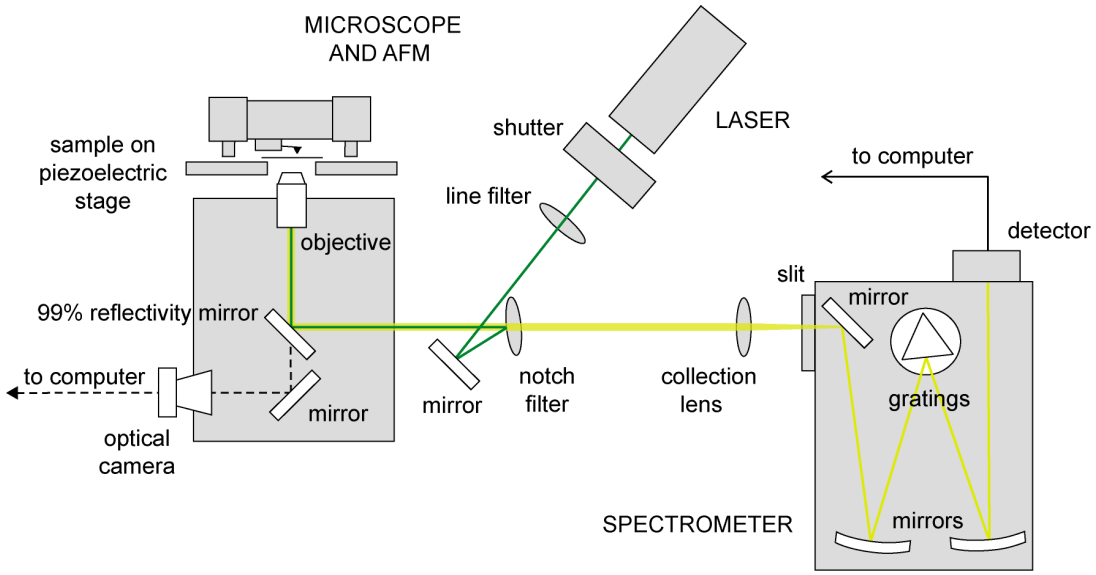

Figure 5.12: Schematic of combined AFM and Raman spectroscopy system.

This development is made possible by the inverted configuration of the setup and a piezoelectric xy-stage, which allows precise control over movement of the sample with respect to the laser beam and the AFM probe. This stage provides the ability to record real-time, chemical mappings that can be processed to produce reproducible images of the Raman scattering across a sample (Figure 5.13). The integration of an AFM also provides the experimental setup required for performing scattering-enhancing technique TERS.

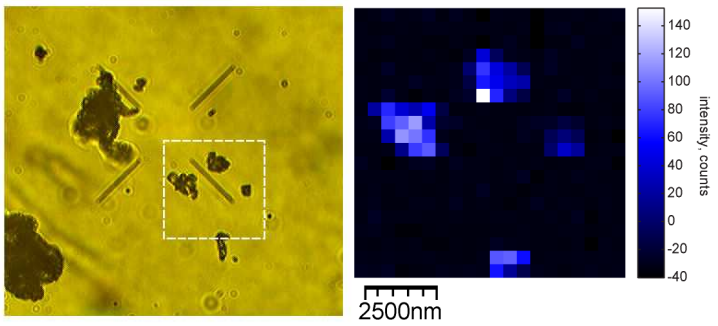

Figure 5.13: Chemical mapping of a crushed paracetamol tablet constructed from its Raman scattering, which is highly reproducible from the optical image (mapped area highlighted).

5.5 Characterising the spatial resolution of the setup

5.5.1 Spatial resolution

The capabilities of Raman spectroscopy for chemical mapping and imaging has advanced rapidly in recent years with the production of faster detectors, advanced spectral imaging software and motorised stages that can step with nanometric precision and reproducibility. However, there are still a number of restrictions to the technique for microscopic analysis. One of these is spatial resolution, which is predominantly limited by the microscope objective.

As light passes through a microscope objective it diffracts depending on the wavelength of light and the finite size of the objective lenses. A result of this diffraction is the apparent broadening of very small objects when observed with a microscope, a phenomenon first described by Abbe in 1873 [130]. The intensity distribution of a microscope image of a very small object is called the response curve, line profile or point spread function (PSF). The PSF of an image usually has a radial symmetry in-plane and a larger broadening along the optical axis. Based on the commonly used Rayleigh criterion, the width of a PSF is approximately equal to the minimum distance between two points at which the points can be resolved.

According to the Rayleigh criterion, the lateral (in-plane) resolution $d_{x,y}$ and the axial (along the optical axis) resolution d_z of a conventional microscope are given by,

$$d_{x,y} = \frac{1.22\lambda}{NA} \tag{5.10}$$

$$d_z = \frac{4\lambda}{(NA)^2} \tag{5.11}$$

where λ is the wavelength of light and NA is the numerical aperture of the objective lens, given by Equation 5.5. These expressions are known collectively as the diffraction limit and form the starting point for the struggle to improve spatial resolution. The ultimate aim is for the PSF of a system to be as narrow as possible, equating to the best spatial resolution that can be achieved with that system.

Most microscope objectives used in Raman spectroscopy are designed to examine the surface of a sample in ambient conditions. These objectives can also be used to obtain spectra below the surface of a sample. However, for this purpose spherical aberrations arise that enlarge the size of the sample volume, particularly along the optical axis [131]. This is due to the effect of refraction at the sample-air interface that occurs with dry metallurgical objectives, which causes the point of focus to shift much deeper into the sample than would otherwise be the case. The use of water- or oil-immersion objectives greatly reduces the severity of aberrations, due to the change in refractive index through the interface being reduced (Figure 5.14). This allows the size of the sample volume to approach the diffraction limit.

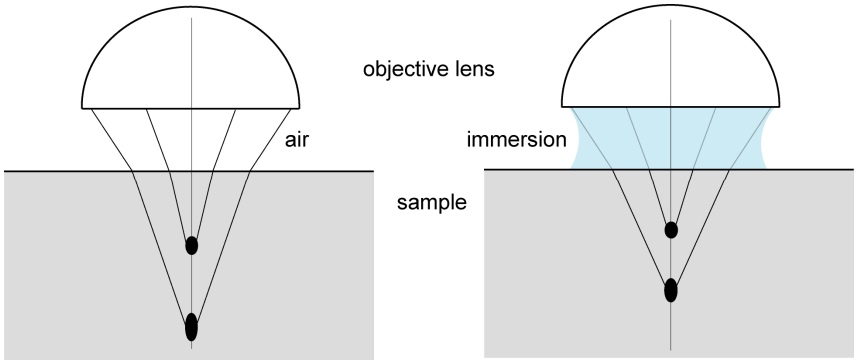

Figure 5.14: Comparison of refraction effects with dry metallurgic and immersion objectives.

5.5.2 Measuring the lateral resolution

Commonly, the spatial resolution of a Raman spectroscopy system is characterised by recording line profiles across polystyrene spheres. This method was combined with chemical mappings to assess the spatial resolution in the xy-direction of the experimental setup described in this chapter. Determining this aspect of the system is particularly important for studying SLBs, in which features of interest such as microdomains are beyond the typical spatial resolution capabilities of Raman spectroscopy.

Samples were made from monodisperse polystyrene spheres with a diameter of 1002nm, 10wt.% in water (Varian, Inc). These spheres were diluted further and deposited onto a quartz coverslip (PI-KEM, UK), previously cleaned with a variety of solvents. The spheres were dispersed thinly across the coverslip, making it

possible to locate isolated spheres. Line profiles and chemical mappings of these polystyrene spheres were constructed as the sample was moved laterally across the laser beam, step by step (Figure 5.15). A Raman spectrum was acquired at each position; the area of a significant Raman band in each spectrum was calculated after subtraction of a local linear baseline and used to build a response curve or mapping. In the case of the polystyrene sphere, the Raman band selected for this purpose occurs at 1001cm^{-1} (aromatic C–C stretching) (Figure 5.16). Assuming a point source or a perfect planar interface, the spatial resolution of the system is defined as the distance across the sample that the signal intensity decreases to half its maximum value, indicated by the full width at half maximum (FWHM) of the response curve.

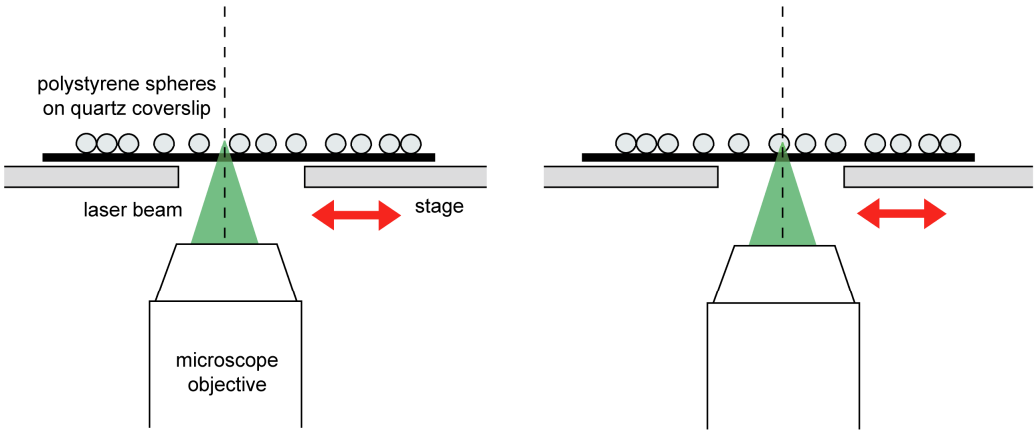

Figure 5.15: Determining the lateral resolution of the setup by measuring the Raman scattering from a polystyrene sphere as it is moved across the focus of the laser beam.

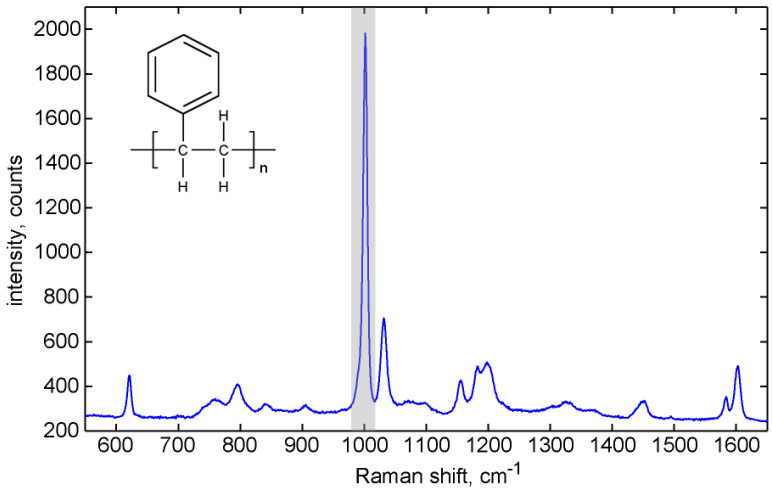

Figure 5.16: Raman spectrum of polystyrene (Raman band used for response curves and chemical mappings are highlighted).

Mappings of single polystyrene spheres were measured with high chemical contrast between the polystyrene sphere and quartz coverslip (Figure 5.17). Single line profiles across the spheres were then extracted from the chemical mappings to obtain the FWHM and spatial resolution. These line profiles exhibit the expected shape and size. As the sphere was moved across the laser beam the intensity of the 1001cm^{-1} Raman band increased up to a maximum value, indicating the point at which the laser was focused on the centre of the polystyrene sphere. Then as the sphere was moved out of the focus of the laser the signal drops back down to the instrumental background level. The width of the response curve indicates a broadening of the 1002nm diameter sphere, demonstrating the diffraction limit of the setup. Finally, the FWHM of these measurements reveals a lateral resolution of 0.965±0.09µm in the x-direction and 0.805±0.03µm in the y-direction.

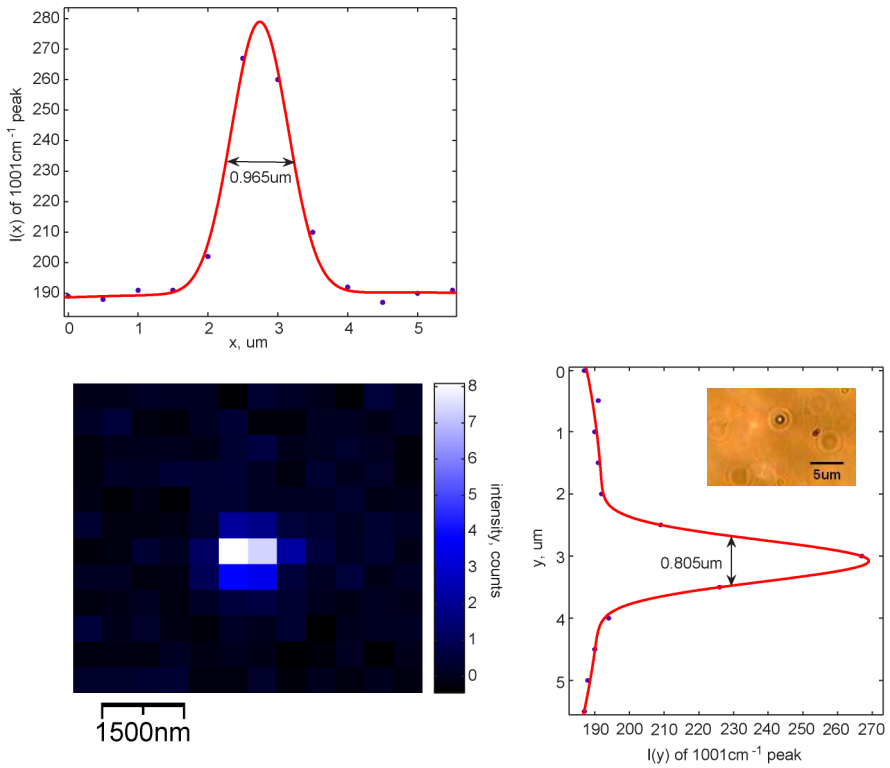

Figure 5.17: Chemical mapping and corresponding response curves measured from a single polystyrene sphere (inset) moving across the focus of the laser beam.

In addition to studying the PSF of a single object with dimensions on the order of the diffraction limit, the lateral resolution of a setup can be determined from its ability to resolve two small objects in close proximity. In the same way as for the isolated spheres, chemical mappings of two neighbouring polystyrene spheres were recorded

from which line profiles were extracted (Figure 5.18). The spheres are easily distinguishable from their response curve. A brief decrease of about 40% in intensity at the midpoint of this curve is an indication of the ability of the microscope objective to resolve these spheres and ultimately the resolution of the setup. It also suggests that spheres even closer together would be resolvable with this setup, as this is not at the limit of the Rayleigh criterion.

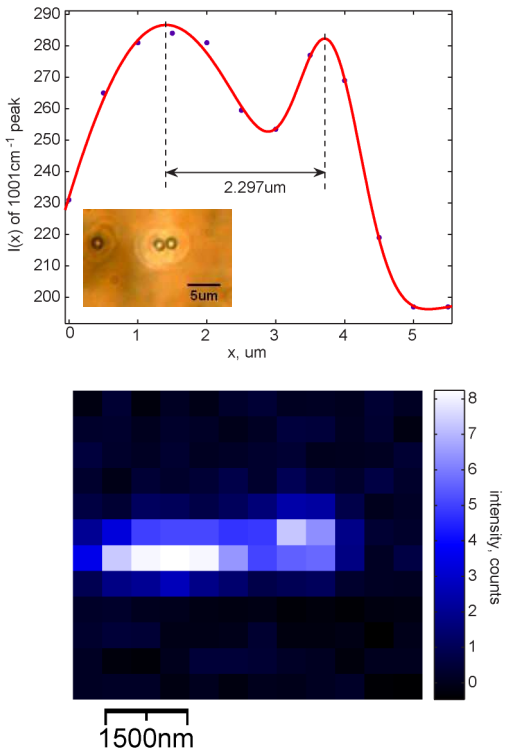

Figure 5.18: Chemical mapping and corresponding response curve measured from two polystyrene spheres (inset) moving across the focus of the laser beam.

The Rayleigh criterion described previously gives a theoretical lateral resolution of 0.541µm for an excitation wavelength of 532nm and numerical aperture of 1.20. The theoretical value is expected to be less than the value determined experimentally, since the Rayleigh criterion provides an ideal in-plane resolution at the diffraction limit that is only achievable with a system that is 100% efficient. In practice, this is not possible. One reason for this is that there is often a mismatch between the diameter of the laser beam and the objective lenses. In this setup the objective is known to be underfilled, meaning that the numerical aperture of the objective is effectively reduced. The objective chosen for this setup has a back aperture diameter of 5.4mm, calculated from Equation 5.9. Replacing this value in the equation with

the diameter of the laser beam, which is just 4mm, gives a numerical aperture of 0.89. This revised value is almost half the actual numerical aperture of the objective and gives a lateral resolution of 0.732μm, which is closer to the value obtained experimentally.

5.5.3 Measuring the axial resolution

Similarly, the spatial resolution in the z-direction can be obtained from line profiles recorded through polystyrene spheres or thin planar materials. For many applications of Raman spectroscopy it is important to have good spatial resolution along the optical axis of the microscope as well as in-plane. Axial resolution is particularly important for samples supported on substrates that may have Raman scattering that could interfere with or overwhelm the desired signal from the sample. This is even more significant for small samples with very weak Raman scattering such as SLBs.

In most cases, the axial resolution of a system is worse than the lateral resolution. This is mainly due to the shape of the laser beam as it passes through the microscope objective (Figure 5.14). Ideally the laser beam would be a perfect sphere at the point of focus. However, even the best objective lenses have limited aperture angle, so the PSF of a microscope is considerably elongated in the z-direction. Additionally, underfilling the objective and general spherical aberrations in the system tend to lengthen the sample volume more along the optical axis.

Polystyrene sphere samples were made as before, whilst line profiles of these polystyrene spheres were constructed as the laser beam was moved vertically through the sample (Figure 5.19). Again, a Raman spectrum was acquired at each position and the intensity of the Raman band at 1001cm^{-1} in each spectrum was used to build a response curve. The FWHM of this curve provided a value for the axial resolution.

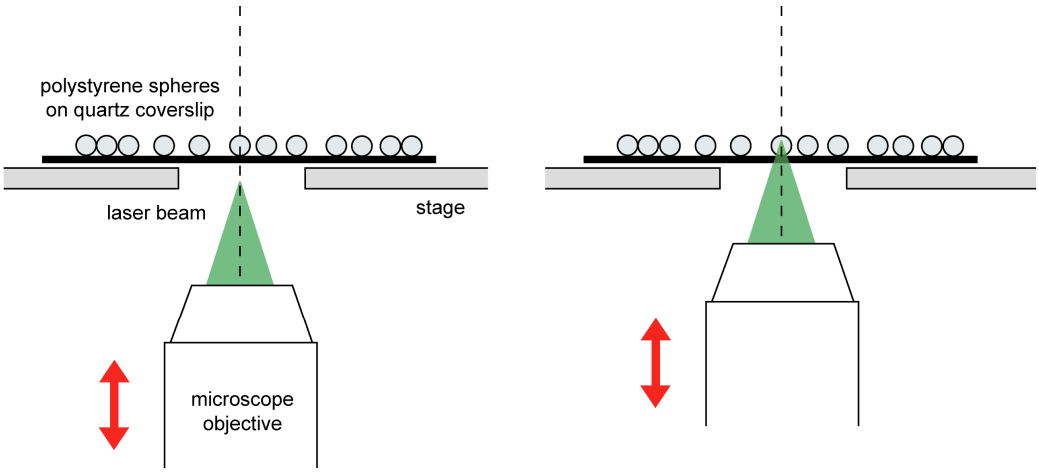

Figure 5.19: Determining the axial resolution of the setup by measuring the Raman scattering from a polystyrene sphere as the focus of the laser beam it is moved through it.

The line profiles of single polystyrene spheres measured along the optical axis of the system exhibit the same shape as those measured in the xy-direction (Figure 5.20a). They are broader, but this is expected as discussed previously. The FWHM of these response curves indicates an axial resolution of 7.095±0.4μm, which is a reasonable value for this system. As with the lateral resolution, the Rayleigh criterion described above gives a theoretical axial resolution of 1.478μm for an excitation wavelength of 532nm and numerical aperture of 1.20, which is less than the value found experimentally. Taking into account the underfilled objective and its reduced numerical aperture, the axial resolution becomes 2.707μm, closer to the value obtained experimentally.

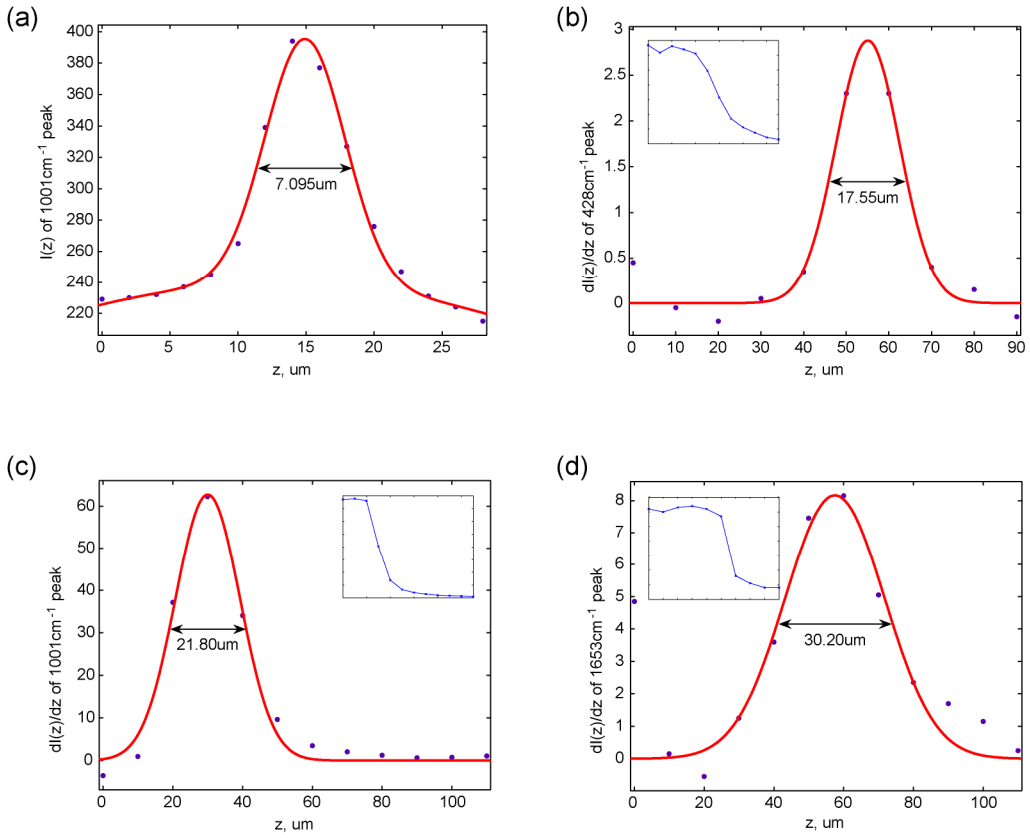

Figure 5.20: (a) Response curve measured from a single polystyrene sphere as the focus of the laser beam is moved through it. The first derivatives of response curves (insets) measured from (b) a quartz coverslip, (c) a piece of polystyrene and (d) a thin layer of oil on a quartz coverslip as the focus of the laser beam is moved through each sample.

Unlike the lateral resolution, there is still no consensus on how best to measure the resolution along the optical axis of a Raman spectroscopy setup. The method of using a single polystyrene sphere to characterise the axial resolution of the system is fairly unrealistic, since the sample is so small. Also, a sphere is fairly complex in terms of the reflection and refraction of light from its surface. A simpler and more reliable measure of axial resolution can be gained from larger samples such as planar surfaces [132]. Therefore the axial resolution was also assessed from several other samples (Figure 5.20b, c and d). These samples were a quartz coverslip, a piece of polystyrene and a thin layer of oil on a quartz coverslip, which provided values for the axial resolution of 17.55±3μm, 21.80±1μm and 30.20±8μm respectively from the FWHM of the first derivative of their response curves. This range of samples determines very different values for the axial resolution of this system. The response curves of these materials were recorded under the same conditions as the polystyrene

spheres, therefore the differences in axial resolution can only be attributed to physical and optical properties of the samples.

The dimensions of the sample, the presence of a substrate and the difference in refractive index between the sample and the objective immersion influence the collection of Raman scattering. The variation in these factors across the range of samples used for the above measurements changes the effect of refraction at the surface of the sample and the spherical aberrations that arise from this (Figure 5.14). This in turn varies the degree of elongation of the laser beam at the point of focus, resulting in a range of values for the axial resolution of the system.

5.6 Improving the axial resolution with a confocal system

5.6.1 Confocal microscopy

The spatial resolution of a Raman spectroscopy setup can be greatly improved by the inclusion of a confocal system [133-135]. Confocal microscopy was one of the earliest methods developed for improving spatial resolution and is now a well established and widely used technique. It is implemented by single point illumination with a laser and selective detection through a pinhole by rejection of any out-of-focus signal. This provides excellent depth discrimination, allowing only a very small effective volume of the sample to be investigated.

To achieve this within a Raman spectroscopy setup, the pinhole is surrounded by a system of lenses and placed between the collection and detection of Raman scattering (Figure 5.21). Conventionally, one lens focuses the scattering from the microscope to a point, at which the pinhole is positioned. This is followed by a second lens that commonly has the same parameters as the first, which collects the scattering passing through the pinhole and directs it towards the spectrometer as a parallel beam. The result is an RMS system that, whilst possessing all the advantages of a conventional Raman spectroscopy setup, has the ability to collect Raman scattering from a sample volume smaller than 1μm in diameter [136, 137]. The depth discrimination capability of a confocal system means that Raman scattering from any surrounding material, such as a substrate that could interfere with or totally hide the weaker

Raman scattering of a sample, can be reduced or even eliminated. Furthermore, the use of confocal microscopy enables the numerical aperture of the objective and consequently the collection angle of the scattered photons to be significantly enlarged. This technique has many advantages over purely using a high numerical aperture objective. There is a limit to the numerical aperture that a microscope objective can have; a maximum numerical aperture of about 1.4 can be achieved with oil immersion. Additionally, high numerical aperture objectives tend to have small working distances and be very expensive.

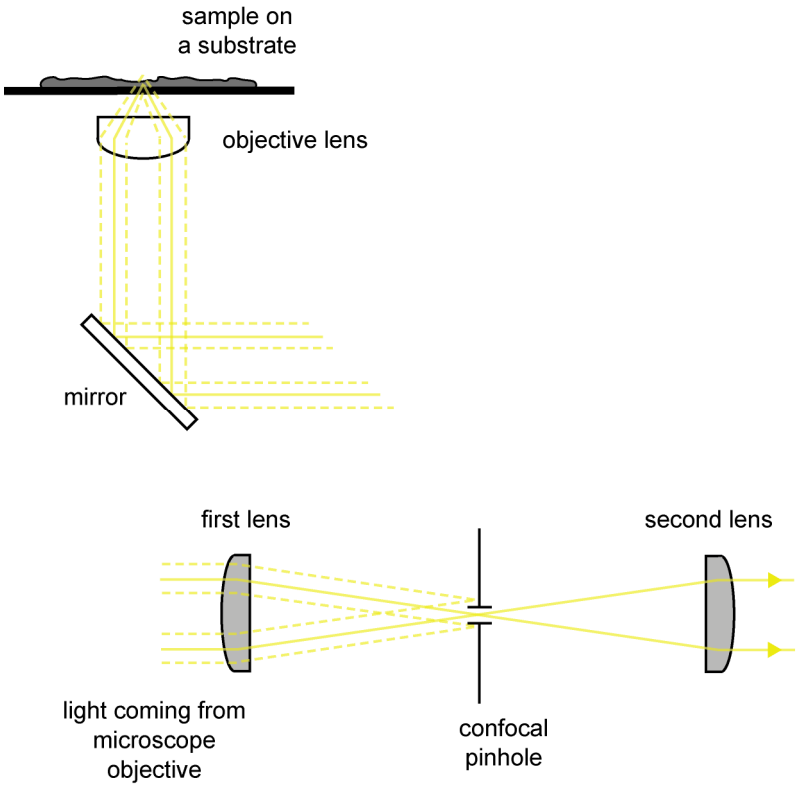

Figure 5.21: Conventional confocal system of two lenses and a pinhole, filtering out any out-of-focus signal from the light coming from the microscope.

The key feature of a confocal system is the pinhole, or aperture. The choice of pinhole size is an important one and depends on the desired resolution and signal intensity. For instance, if a pinhole is chosen to obtain optimal resolution, the signal intensity may be too low. Alternatively, a larger pinhole will allow more signal to be detected but at the expense of spatial resolution. Therefore, when setting up a confocal system there is a compromise between resolution and signal intensity. This balance is particularly significant when experimenting on biological structures such

as SLBs, which are small enough to require good spatial resolution as well as having weak Raman scattering. Furthermore, the process of positioning a confocal system in the setup and optimising the alignment of the pinhole in the optical path is essential to the success of the technique. However, it is not straightforward and can be very time-consuming. Therefore it is beneficial to investigate the impact that a confocal system could have on the spatial resolution of the setup beforehand. It is possible to create a confocal system using the spectrometer already in place, in which the function of the pinhole is achieved by using the combination of the entrance slit of the spectrometer and the vertical binning of the CCD to act as an aperture [138].

5.6.2 Investigating the potential of a confocal pinhole

The potential of including a confocal system in the setup described in this chapter has been assessed over a range of pinhole diameters, provided by the combination of spectrometer entrance slit widths of 20, 50, 80 and 100μm and detector vertical binning of 1, 2, 3 and 4 pixels respectively. Measurements with these pinhole diameters were compared to having no pinhole at all, which was implemented by having the entrance slit fully opened to 2.5mm and using the entire CCD chip. The spatial resolution of these different confocal systems was measured as before, collecting spectra of a 1002nm diameter polystyrene sphere on a quartz coverslip as the laser beam was moved through it and transforming these spectra into response curves with FWHM.

The spectra recorded from this process at the point of maximum signal intensity are shown in Figure 5.22. It is evident from these spectra that the presence of a pinhole in the setup greatly reduces any unwanted background signal. For the case in which there was no pinhole present there is a large amount of Raman scattering collected from the polystyrene sphere, but there is also a significant signal from the quartz coverslip and the entire spectrum is sitting on a large instrumental background. The rest of the spectra demonstrate a loss in signal from the sphere as the pinhole is introduced and gradually reduced in diameter. However, this is to be expected from a confocal system and cannot be avoided completely. More importantly, the reduction in scattering from the coverslip and general background is greater.

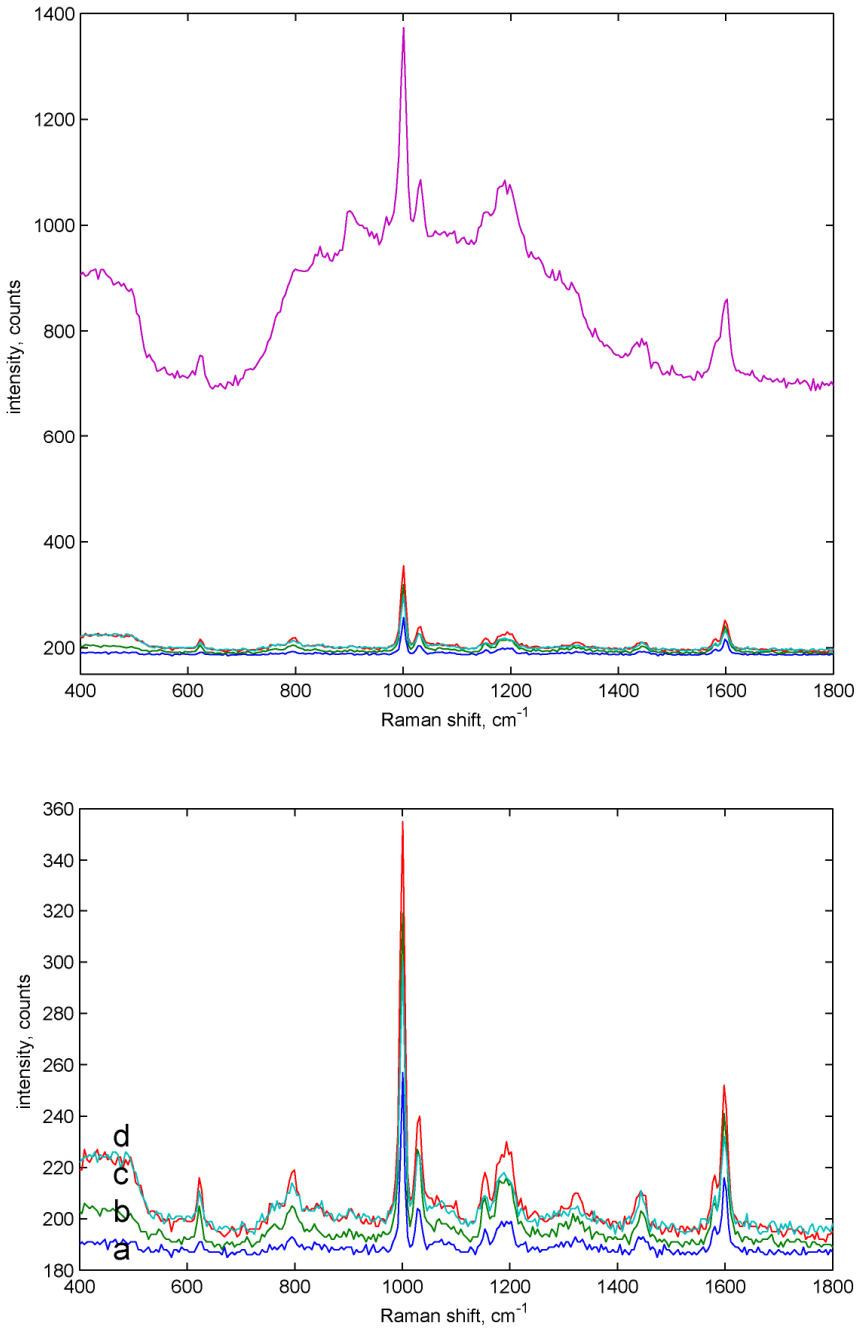

Figure 5.22: Raman spectra of a single polystyrene sphere on a quartz coverslip recorded with pinhole diameters of (a) 20µm, (b) 50µm, (c) 80µm and (d) 100µm (top image includes Raman spectrum recorded with no pinhole).

The key to optimising a confocal system is the balance of signal intensity to spatial resolution, as some Raman scattering from the sample is always blocked by the pinhole at the expense of removing unwanted signal. This balance can be investigated by comparing the intensity of Raman scattering from the sample and substrate and the spatial resolution achieved over the range of pinhole diameters (Figure 5.23). For each spectrum in Figure 5.22 the area of the Raman bands at

1001cm^{-1} and 428cm^{-1} was calculated after subtraction of a local linear baseline, corresponding to the intensity of scattering from the polystyrene sphere and quartz coverslip respectively. Firstly, the ratio of these intensities is considered, which allows for the inevitable reduction in signal collected from the polystyrene sphere when a pinhole is in place (Figure 5.23a). For instance, the setup with no pinhole has high signal intensity from the polystyrene sphere. However, in this case the ratio of intensities is low, as it also has a much greater background signal than the other setups. Then as smaller pinholes are introduced this ratio increases. This parameter and the relative intensities of sample and substrate suggest that a good pinhole diameter for this setup is around 60-70µm, for which there is a reasonable level of Raman scattering collected from the polystyrene sphere whilst the signal intensity from the quartz coverslip is still low. A pinhole diameter in this range would provide a spatial resolution of about 6.9µm in the z-direction (Figure 5.23b), which is an improvement on the equivalent value obtained from the conventional setup.

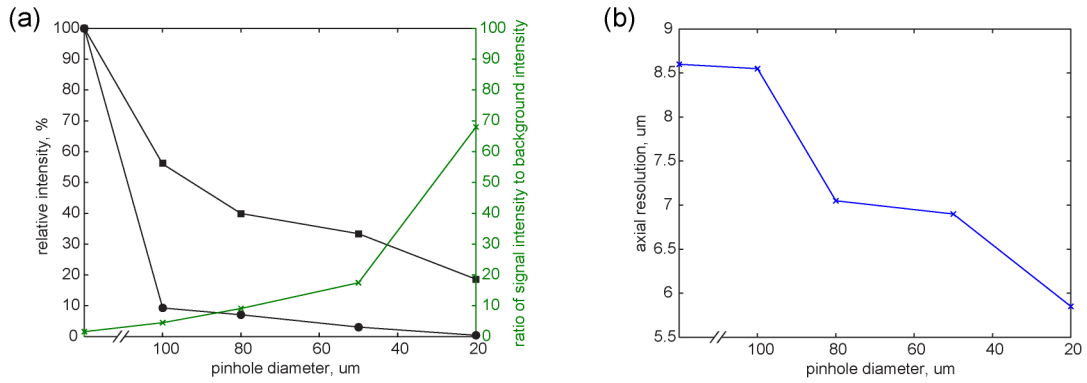

Figure 5.23: Influence of pinhole diameter on (a) signal intensity collected from polystyrene sphere (■), background signal intensity collected from quartz coverslip (●), ratio of these intensities (×) and (b) axial resolution.

5.6.3 Development of a confocal system

After demonstrating its potential, a confocal system of a pinhole and two lenses was added to the Raman spectroscopy setup. The first step in the development of this system is to identify the lenses and pinhole that are most suitable for the existing setup. The setup had around 400mm between the notch filter and collection lens in which the confocal system could be positioned. Therefore the maximum focal length that each of the two lenses could have was 200mm. To determine the minimum

diameter of pinhole that could be combined with these lenses, the magnification M of an image coming from the microscope objective and passing through the system must be considered, given by

$$M = \frac{f_l}{f_{obj}} \tag{5.12}$$

where f_l is the focal length of the confocal lens. The objective used in this setup has a focal length of 3mm, which means that a lens with a focal length of 200mm would provide a magnification of about 67×. According to Equation 5.10, the in-plane diameter of light collected by the objective is around 0.541μm. Therefore after passing through the first confocal lens, the diameter of the image of this light at the point of focus would be about 36μm. This point also corresponds to the position of the pinhole; therefore the minimum diameter of pinhole for this system is 36μm. Considering the underfilling of the objective and the subsequent reduction in its numerical aperture, this value increases to about 49μm. These theoretical values were expected to be less than the actual pinhole diameter suitable for the setup, but they were used for guidance in choosing a range of pinholes to assess experimentally. These were 50, 75, 100 and 150μm in diameter, in addition to two lenses each with a diameter of 25.4mm and focal length of 200mm (Thorlabs, UK).

The main reason for including a confocal system in a setup is to improve its axial resolution by removing any unwanted signal. However, as was demonstrated in the previous section, a confocal system also causes an unavoidable reduction in the intensity of Raman scattering collected from the sample. Therefore, it is the balance of all these parameters that were considered when positioning and aligning the confocal system and determining the suitability of each pinhole.

Firstly, the two lenses were positioned in the light path in the same way as any optical element as in Section 5.3.4. The pinholes were then positioned in the middle of these lenses and aligned by monitoring the Raman scattering collected from a piece of silicon. Silicon was used for this purpose as it is an opaque material; this ensures that the point at which maximum scattering is collected from the sample

corresponds to the laser being focused at its surface. The intensity of this Raman scattering was determined from the area of the Raman band at 520cm^{-1}, calculated after subtraction of a local linear baseline (Figure 5.24). As expected, this intensity greatly reduced when the 150µm pinhole was added to the system and then reduced further with each pinhole. These measurements suggest that the scattering focused by the first confocal lens has an image diameter of between 75 and 100µm, as there is a significant drop in signal intensity with the addition of the 75µm pinhole.

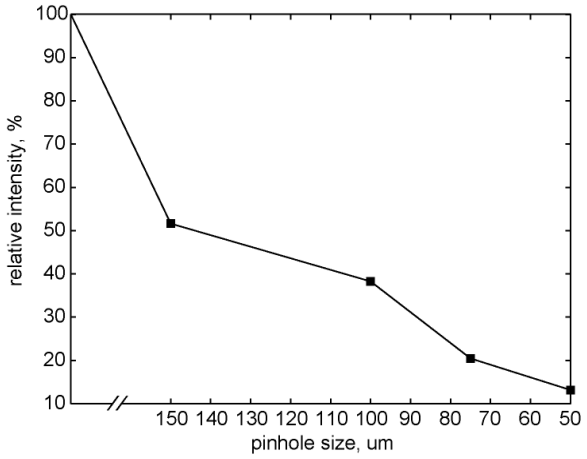

Figure 5.24: Influence of pinhole diameter on signal intensity collected from a piece of silicon as each pinhole was aligned in the optical path.

As before, once each pinhole was in position a series of Raman spectra were recorded as the laser beam was moved through a 1002nm polystyrene sphere on a quartz coverslip. These spectra were then transformed into response curves from which the axial resolution could be determined. This process was also repeated for the case in which there was no pinhole and just the two lenses. The spectra collected at the point of maximum signal intensity are shown in Figure 5.25. Again, there is a large amount of Raman scattering collected from the polystyrene sphere when there was no pinhole in place, but also a significant signal from the quartz coverslip. There is also a broad instrumental background in this spectrum. The rest of the spectra demonstrate a slight drop in signal from the sphere as each pinhole is introduced, but a more significant reduction in signal from the coverslip and general background.

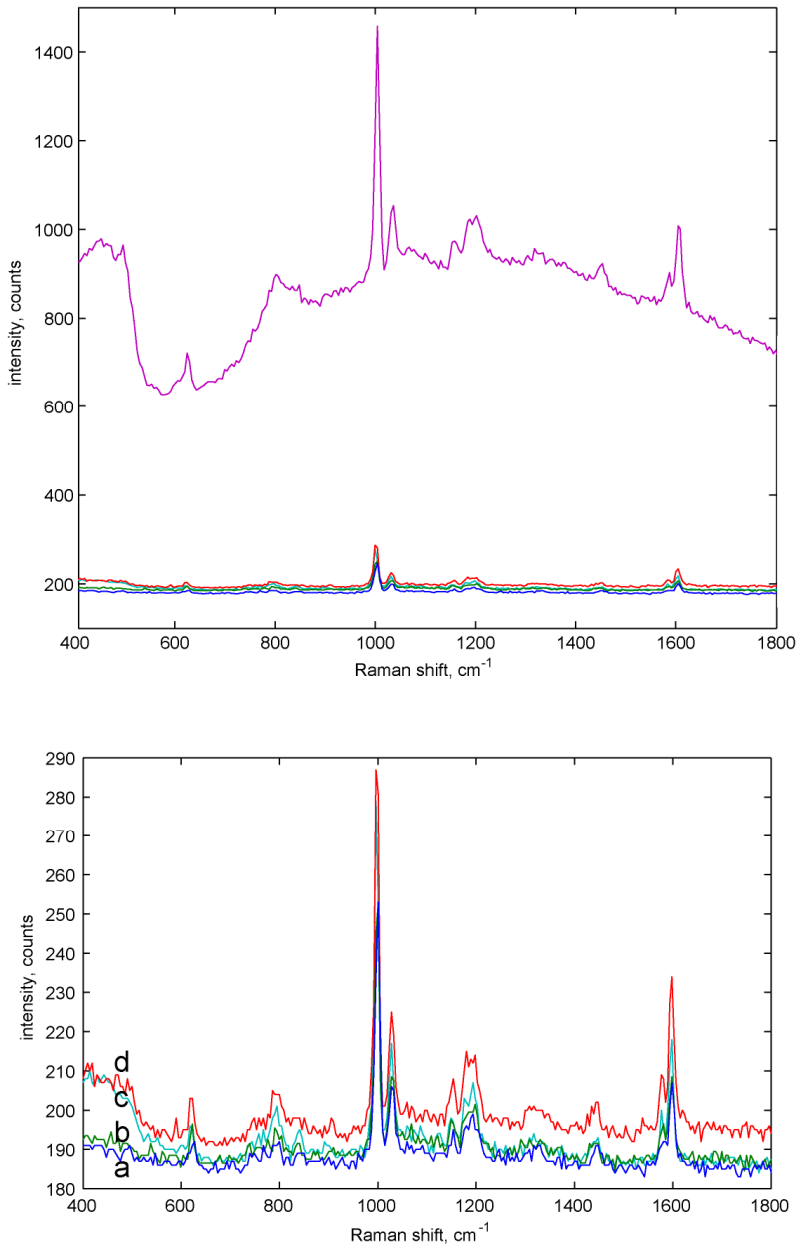

Figure 5.25: Raman spectra of a single polystyrene sphere on a quartz coverslip recorded with pinhole diameters of (a) 50µm, (b) 75µm, (c) 100µm and (d) 150µm (top image includes Raman spectrum recorded with no pinhole).

For each of the above spectra, the area of the Raman bands at 1001cm^{-1} and 428cm^{-1} was calculated after subtraction of a local linear baseline, corresponding to the intensity of scattering from the polystyrene sphere and quartz coverslip respectively. These intensities were then combined with measurements of the axial resolution to explore the balance between signal intensity and resolution (Figure 5.26). Firstly, the ratio of sample to substrate signal intensity was addressed, which gradually increases as the pinhole diameter is decreased (Figure 5.26a). The most significant increase in

this parameter occurs with the addition of the 75µm pinhole, for which the reduction in signal intensity from the quartz coverslip is much greater than any loss in signal intensity from the polystyrene sphere. Similarly, the 75µm pinhole provides the greatest improvement in axial resolution (Figure 5.26b).

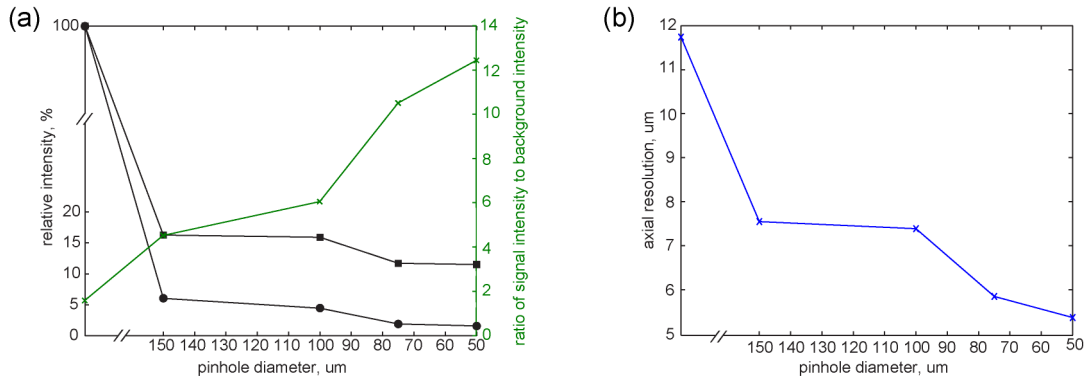

Figure 5.26: Influence of pinhole diameter on (a) signal intensity collected from polystyrene sphere (■), background signal intensity collected from quartz coverslip (●), ratio of these intensities (×) and (b) axial resolution.

This method of measuring the PSF of polystyrene spheres is well-established and widely used to characterise the spatial resolution of microscopy and spectroscopy systems. However, the value of axial resolution obtained from this method is highly idealised, since the sample is so small. A more realistic measure of axial resolution is determined from using the same method but with a layer of oil on a quartz substrate (Figure 5.27). This sample indicates a similar level of improvement in axial resolution with the addition of each pinhole as the polystyrene sphere. However the values of resolution are far more realistic, the 50µm pinhole reducing the axial resolution to 11.9µm.

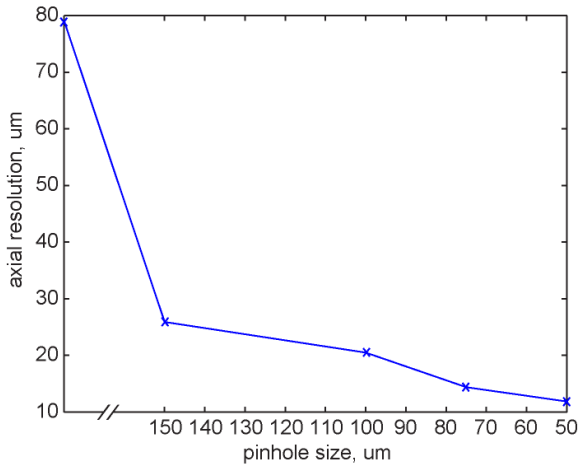

Figure 5.27: Influence of pinhole diameter on axial resolution, measured from a thin layer of oil on a quartz coverslip.

From all these measurements, it is apparent that the inclusion of a confocal pinhole of any diameter in the Raman spectroscopy setup is beneficial to some extent. However, the 75µm diameter pinhole offers the greatest improvement in axial resolution whilst retaining as much scattering from the sample as possible. Consequently, the addition of this confocal system also offers an improvement in the lateral resolution of the setup (Figure 5.28).

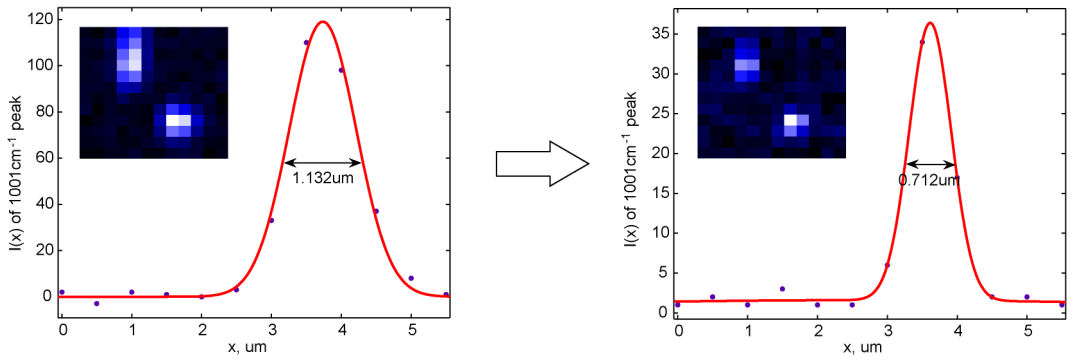

Figure 5.28: Chemical mappings (inset) and corresponding response curves measured from a single polystyrene sphere moving across the focus of the laser beam, indicating an improvement in the lateral resolution on the addition of the 75µm pinhole.

5.7 Conclusions

A Raman spectroscopy system based on an inverted microscope has been developed and characterised for studying SLBs. This system was built in-house from individual

components that were each designed, purchased, aligned and calibrated. Further development of the system included in the integration of AFM to allow simultaneous topographical imaging and high sensitivity chemical mapping. The spatial resolution of the system was then assessed from the response curves of polystyrene spheres as a function of their position in the focus of the laser beam. The lateral resolution in the x- and y-direction was found to be 0.965±0.09μm and 0.805±0.03μm respectively, which is excellent for this type of setup and sufficient to clearly resolve two spheres in close proximity to each other. The resolution along the optical axis was determined to be 7.095±0.4μm, which as expected is slightly worse than in-plane but reasonable for this system. The axial resolution was further investigated for several other materials with different dimensions and refractive indices. These samples provided values for the axial resolution ranging from about 17 to 30μm. Following these measurements, the potential to improve the axial resolution of the existing setup by adding a confocal system was explored. Firstly, the combination of the entrance slit and detector of the spectrometer was used to imitate this system, which indicated that the axial resolution could be reduced to about 6.9μm with a pinhole diameter of around 60-70μm. Then a confocal system of two lenses and a pinhole was added to the setup. A number of different diameters of pinhole were assessed for the purpose of improving in the axial resolution of the setup whilst causing minimal reduction in the signal intensity from the sample. A pinhole diameter of 75μm was found to be most suitable, resulting in an optimised RMS setup with integrated AFM.

Chapter 6

AFM and non-resonant Raman spectroscopy

In this chapter, the combination of AFM and Raman spectroscopy for investigating SLBs is discussed. Experiments are carried out to assess a variety of substrates for their suitability for both AFM and Raman spectroscopy studies. The compatibility of the substrate for supporting a single SLB must also be considered. The effect, if any, of laser power and exposure time on lipids is addressed. Finally, SLBs are measured and characterised with AFM and the RMS system.

6.1 Introduction

Supported lipid bilayers (SLBs) have found wide application as a model for the cellular membrane in biophysical research. SLBs consist of amphiphilic molecules called phospholipids that can self-assemble into a bilayer structure when deposited onto a hydrophilic support from an aqueous solution, either by vesicle fusion or the Langmuir-Blodgett (LB) technique [139]. Phospholipids dipalmitoylphosphatidylcholine (DPPC) and dioleoylphosphatidylcholine (DOPC) are saturated and unsaturated respectively and therefore have very different phase transition temperatures [74]. When combined in SLBs these lipids form microdomains, phase-separated areas of ordered gel state and disordered liquid-crystalline state, which affect the structure and biological function of membranes and

are an important feature in many cellular processes. These artificial membranes are well-defined and stable under a variety of conditions, allowing characterisation with a broad range of physical methods.

Atomic force microscopy (AFM) is one of the leading techniques for investigating SLBs, providing high-resolution imaging and a range of mechanical and electrical measurements [6]. Its ability to detect deviations in the topography of a surface with Ångström precision also makes AFM an invaluable tool for studying small deviations in the structure of an SLB such as microdomains [15]. SLBs are imaged in tapping mode with long triangular silicon nitride cantilevers with low spring constants, with both the sample and probe immersed in water. A common feature of SLBs is defects, or holes, which can be used to measure its thickness and in turn confirm its presence.

Raman spectroscopy is an optical method that is widely used for chemical analysis of biological materials, generating a spectral fingerprint of a given sample from the inelastic scattering of monochromatic light [28]. This spectrum provides extensive information about the sample based on intrinsic molecular vibrations arising from specific components in its physiochemical makeup. Raman spectroscopy has many advantages for studying biological materials, for instance it allows label-free, real-time investigation with high chemical specificity. The technique has the potential to offer detailed chemical and structural analysis of SLBs. Previously, optical-trapping has enabled the study of single phospholipid vesicles [38], but this technique is not suitable for investigating planar SLBs. The sensitivity and spatial resolution that can be achieved with conventional Raman spectroscopy can restrict its effectiveness at the micro- and nanoscale. A confocal Raman microspectroscopy (RMS) system, whilst possessing all the advantages of a conventional setup, has the ability to collect Raman scattering from a sample volume of less than 1μm in diameter. This technique is implemented by selective detection of Raman scattering through a pinhole by rejection of out-of-focus signal. Therefore any signal arising from any surrounding material, such as a substrate, that could obscure the weaker Raman signal from the sample can be eliminated. This enables excellent depth discrimination. Potentially, the combination of this method with AFM has the ability to topographically, mechanically and chemically investigate SLBs [43, 44]. However, there are a few issues to be addressed. Many of these relate to the choice

of substrate, which must be compatible with Raman spectroscopy, AFM, the experimental setup and the sample. Firstly, a single SLB is only about 4nm thick, so in order to detect it with AFM its substrate should have virtually no roughness at the nanoscale. Secondly, the RMS system contains an inverted microscope to allow for simultaneous AFM and the study of samples in liquid. This means that the substrate must be transparent, since any Raman scattering from the sample is collected through it. Finally, like most biological materials, lipids are very weak Raman scatterers. Therefore a substrate suitable for this application is required to have very little Raman signal itself. RMS allows selective detection, but making a careful choice of substrate avoids relying solely on this rejection of out-of-focus scattering. To begin experiments with a substrate that will have little contribution to the overall Raman scattering of the sample will assist in the success of this technique. Another important aspect to consider when studying biological materials with laser-based methods is whether or not there is any damage caused by prolonged exposure to high laser powers that may alter its physiochemical makeup. This holds for lipid molecules and needs to be addressed.

6.2 Choosing a suitable substrate

6.2.1 Contribution to Raman scattering

Firstly, a wide variety of substrates were assessed for investigating SLBs in terms of their own Raman scattering. These substrates were chosen for their current use in biological studies with either Raman spectroscopy or AFM, but it is unknown whether any of them are suitable for both techniques. For studying SLBs with Raman spectroscopy, the position of any Raman bands as well as the overall background signal produced by each substrate is important. A suitable substrate is required to have as few peaks as possible in its spectra. Any Raman bands that are present should not occur in the spectral range of interest for lipids (600-3200cm^{-1}) and especially not in the fingerprint region up to about 1600cm^{-1}. The ideal substrate should also have a minimum overall background signal, in order to avoid hiding the weak scattering excited from lipids making detection very difficult.

The Raman spectra of a range of substrate materials are shown in Figure 6.1, recorded with a laser power of 10mW and exposure time of 5s. Mica is a material that is widely used for AFM studies of biological materials, particularly model lipid membranes [140, 141]. This is due to its excellent cleavage, which provides an atomically flat surface that is ideal for imaging nanoscale structures. It is easy to split the mica into molecular layers, producing single sheets of mica with absolute minimum roughness with excellent reproducibility. However, mica has a considerable number of peaks at low Raman shifts and a broad background, deeming it unsuitable for Raman spectroscopy studies. Glass coverslips are a readily available and commonly used transparent substrate, but they have a very large background that covers the entire fingerprint region, no matter how thin. Quartz is a possible substrate for Raman spectroscopy studies, since it has lower signal than both mica and glass. For AFM of SLBs, a mica substrate is often used with a glass support. A more promising alternative to this would be to use quartz instead. However, the combination of two different materials creates a huge Raman background due to the additive nature of the scattering from the individual substrates and also the introduction of an extra interface. This interface between the two materials triggers refraction of the laser light and any scattering from the substrate, which will fall as stray light in the spectrometer and appear as extra background signal in the Raman spectra. From Figure 6.1, the most suitable substrates for studies of SLBs with Raman spectroscopy are magnesium fluoride (MgF_2) and sapphire. These are both thin and transparent and have minimal Raman scattering. The Raman spectra of these materials contain few and distinct peaks and almost no background.

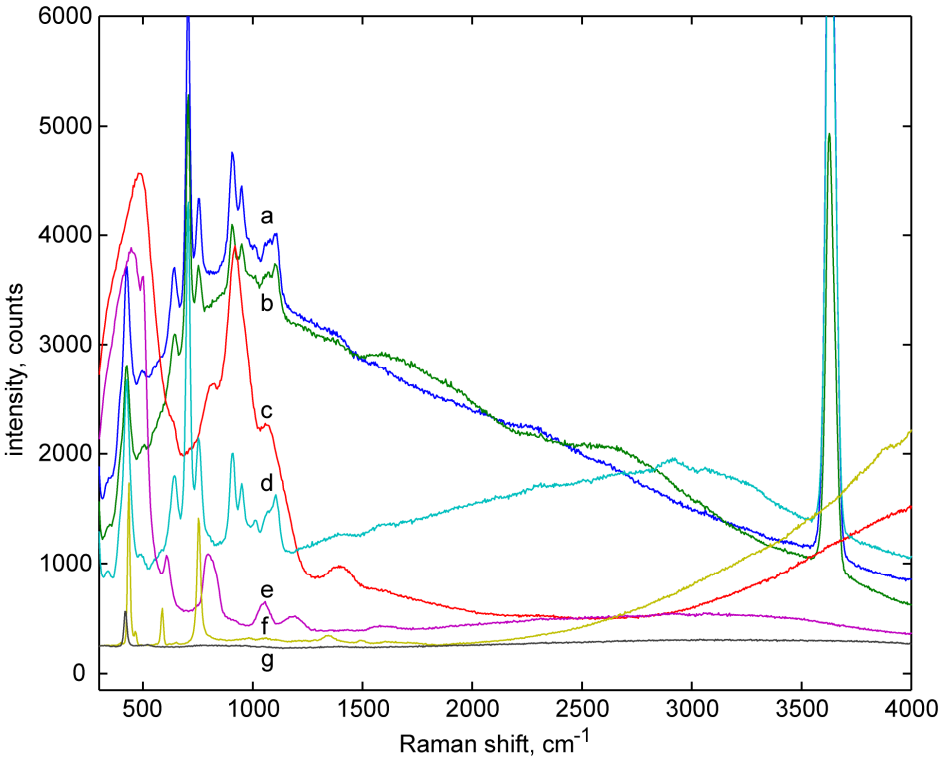

Figure 6.1: Raman spectra of substrates to be considered for studying SLBs (a) mica on glass (b) mica on quartz (c) glass (d) mica (e) quartz (f) sapphire (g) MgF_2.

Another way to assess the suitability of these substrates for studying SLBs is to determine whether a small sample with weak Raman scattering can be detected on them. For this, a single 1002nm polystyrene sphere was measured on each substrate and the ratio of the Raman scattering from the sample to that of the substrate was calculated. This ratio compares the intensity of the 1001cm^{-1} Raman band of polystyrene (I_s) with the intensity of the background arising from the substrate at the same spectral position (I_{bg}) (Figure 6.2).

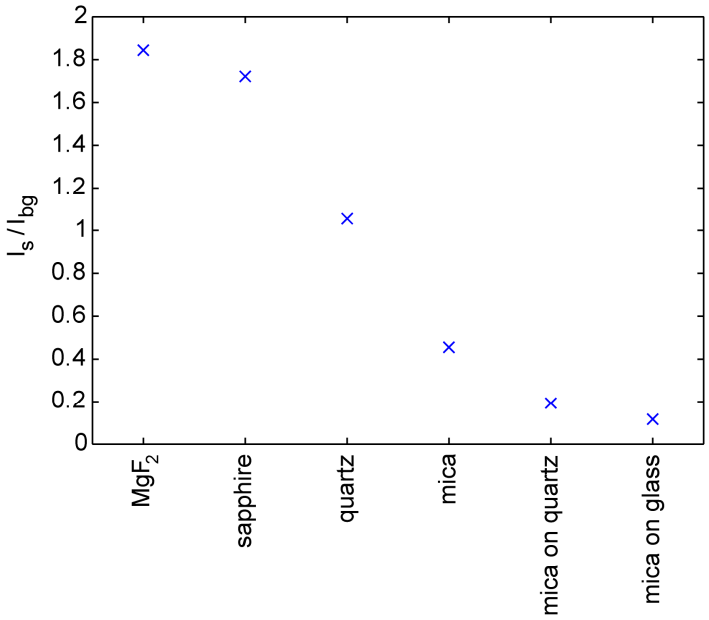

Figure 6.2: Plot of the ratio of signal to background at 1001cm^{-1} of a polystyrene sphere on a range of substrates.

As seen in the Raman scattering of these materials, the combination of mica with a support of glass or quartz produces a large background signal. This makes it almost impossible to detect the Raman scattering from the polystyrene sphere, evident from its low ratio of signal to background. The polystyrene sphere on just mica has only a slightly higher ratio. In contrast quartz, MgF_2 and sapphire all have significantly lower signal and consequently fairly high ratios of signal to background when detecting a 1002nm diameter polystyrene sphere. Therefore these three materials are the most suited to detecting comparably weak Raman scatterers such as SLBs. For instance, the spectrum of polystyrene is evident within the spectrum of sapphire (Figure 6.3). Raman bands in the spectrum of sapphire are below the main region of interest for SLBs. Also, for an exposure time of 5s, around 200 counts of the overall background signal is from the instrumental setup, therefore sapphire adds very little to this.

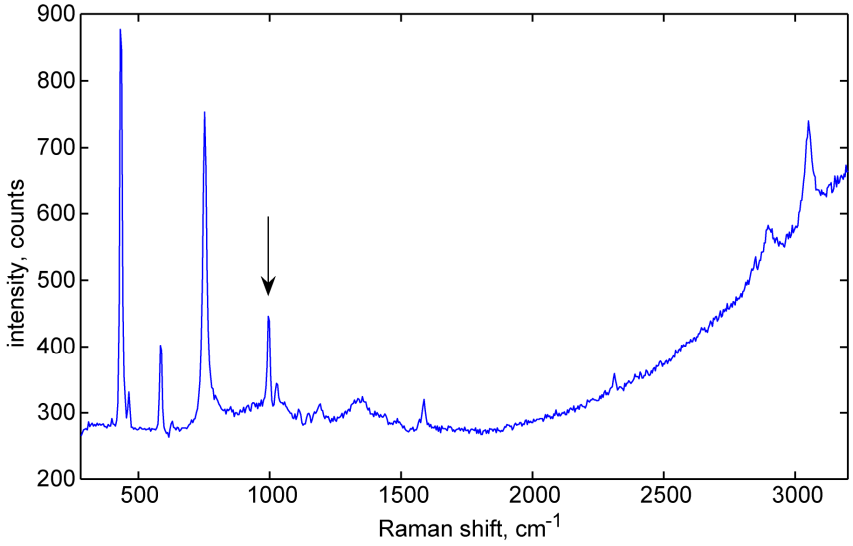

Figure 6.3: Raman spectrum of a single polystyrene sphere on sapphire (arrow highlights 1001cm^{-1} Raman band of polystyrene).

6.2.2 Characterising roughness for AFM imaging

Potentially quartz, MgF_2 and sapphire all have the appropriate Raman scattering to detect SLBs. However, to also be suitable for simultaneous AFM imaging of lipid microdomains, their surface must be relatively smooth. Therefore these substrates must be assessed for their nanoscale roughness. The signal collected from an AFM probe is primarily caused by the interactions between the tip and the surface of the material being imaged. However, it also has some contribution from the substrate that is supporting the material. Changes in substrate height of as little as 1Å can be detected in the overall topographical measurement of a sample, which means that the choice of substrate for thin, soft samples is of great importance. Biological cells are large enough to be studied with AFM on a substrate of considerable roughness, but for SLBs that are merely a few nanometres high a substrate is required to be atomically flat.

A substrate commonly used for depositing SLBs onto is mica. Mica is an aluminium silicate mineral with a hexagonal sheet-like arrangement of atoms and consequently can be mechanically cleaved to produce an atomically flat surface. This is the most prominent characteristic of mica and that which makes it an ideal substrate for AFM when studying nanoscale structures. Imaging a cleaved piece of mica with AFM

reveals a root mean squared roughness of just 50pm (Figure 6.4). This is the level of roughness that is required to successfully image a single SLB. However, it has been previously demonstrated that its Raman scattering is unsuitable for the combined AFM-Raman system.

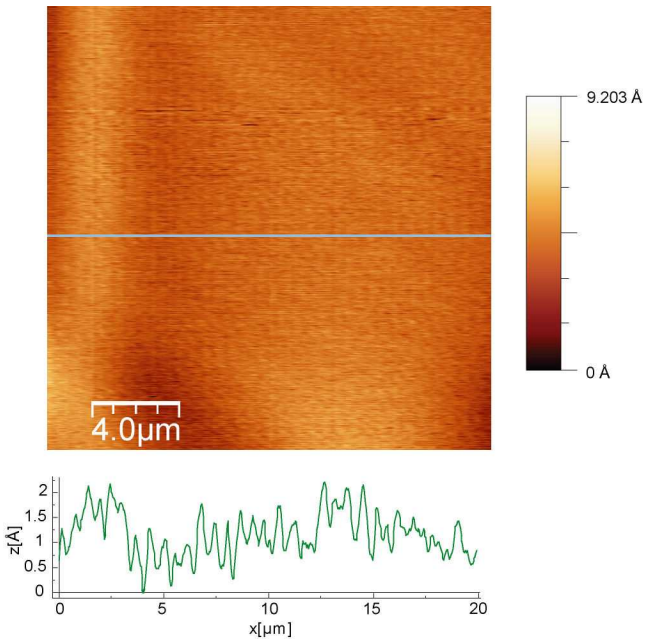

Figure 6.4: AFM image and corresponding line profile of mica.

MgF_2 is often used for Raman spectroscopy studies of biological cells. It is a white crystalline salt that is transparent and has very little Raman scattering. However, it is unsuitable for imaging SLBs with AFM. After being cleaned with various solvents, MgF_2 still has a roughness of around a nanometre (Figure 6.5), which is too large for measuring the topography of SLBs accurately.

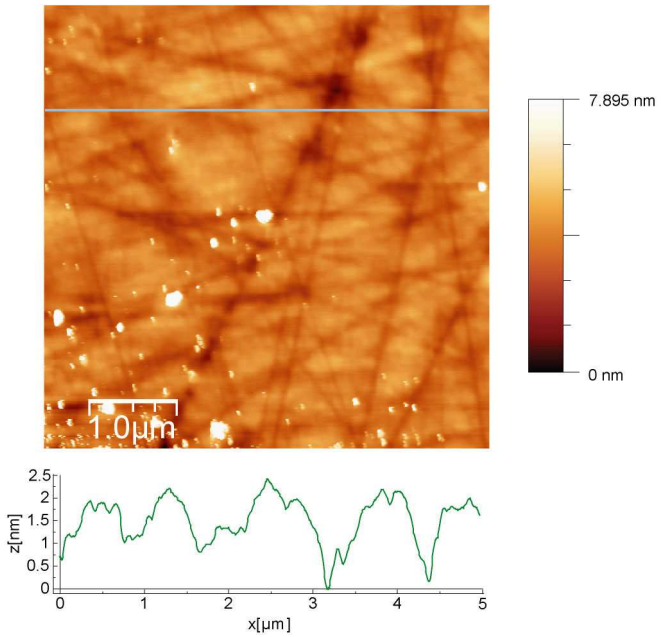

Figure 6.5: AFM image and corresponding line profile of MgF_2.

Another substrate with a suitable Raman scattering for detecting SLBs on is sapphire. Sapphire is a gem made of the mineral corundum, an aluminium oxide, which has a transparent appearance compatible with the inverted RMS system. Sapphire can be bought as an epi-polished single crystal, which can withstand annealing at very high temperatures and acid etching. Preparing the material in this way triggers step bunching, a phenomena in which atomic steps in the surface of the sapphire move together to leave large, flat terraces [142]. This makes it ideal for simultaneous AFM and Raman spectroscopy of SLBs, as it results in a clean surface that has a roughness comparable with that of cleaved mica (Figure 6.6).

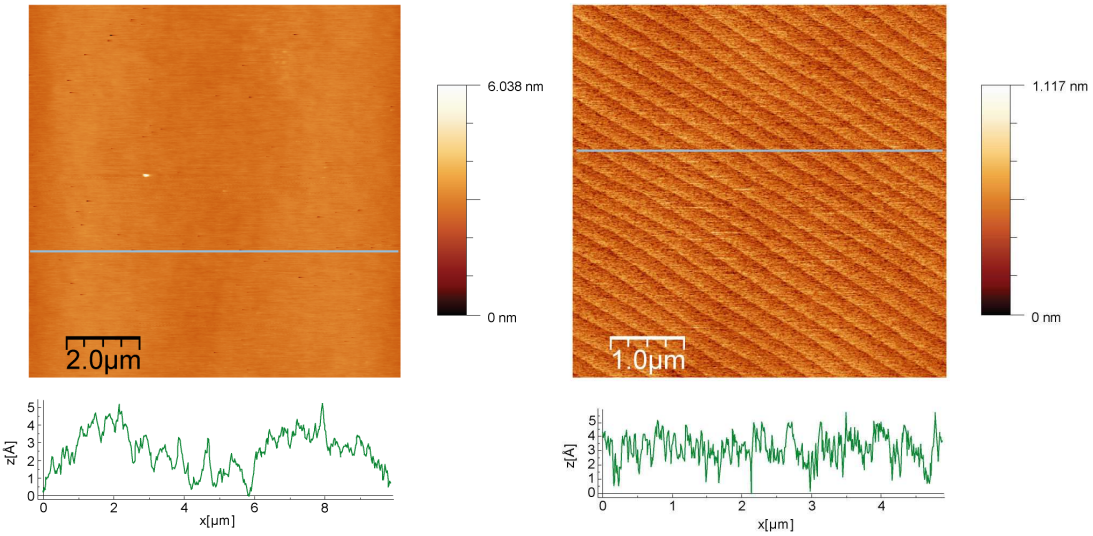

Figure 6.6: AFM images and corresponding line profiles of sapphire (the image on the right is of an area containing steps).

Glass and quartz are both transparent materials suitable for the inverted configuration of the experimental setup. Quartz also has minimal Raman scattering and consequently is commonly used in Raman spectroscopy studies. However, both these materials are known to have considerable roughness, therefore making them unsuitable for imaging SLBs with AFM.

6.3 Assessing the effect of laser power and exposure

Before using Raman spectroscopy to study SLBs, it is important to rule out any effect that the laser could have on the lipids. Exposure to high laser powers could disturb their chemical structure and consequently introduce variations into the Raman spectrum of the material. High laser powers or long exposure times are often used in non-resonant Raman spectroscopy experiments in order to obtain the highest signal-to-noise ratio spectra possible. This would provide the best chance of detecting SLBs. However, this may not be possible if these factors induce thermal effects that cause changes in the physiochemical makeup of the lipid molecules.

Small spectral changes may be significant but not apparent by eye. Therefore a careful statistical analysis is required to detect the slightest variance in the Raman spectra. Singular value decomposition (SVD) and principal component analysis (PCA) are common techniques for data reduction and analysis of multivariate data

that allow spectral similarities or differences to be easily seen and identify the principal directions in which the data varies [143]. They are statistical methods that explain variability among observed random variables in terms of fewer unobserved random variables and consequently indicate how correlated a data set is. In Raman spectroscopy, SVD and PCA have been previously used for the evaluation of the potential influence of high laser powers on the chemical distribution of material [144, 145]. These techniques have also been used for the reduction of noise in data sets for chemical imaging and subsequent analysis of the spectral content. For example, if a group of spectra such as the chemical components of a biological cell have definite and repeatable differences, the data points from each component are clustered together. This provides discrimination of different Raman signatures within a single data set.

If the variation in a data set is caused by some natural property or random experimental error, it is expected to be normally distributed. However, if the variation in data is caused by some other relationship, PCA provides a way of reducing the dimensionality of a data set in order to represent its variance. This is done by transforming a number of possibly correlated variables into a smaller number of uncorrelated variables called principal components. This creates a new co-ordinate system such that the direction with the greatest variance lies on the first co-ordinate (PC1), the second greatest variance on the second co-ordinate (PC2), and so on. These later co-ordinates will contain parameters that are essentially constant with some noise. The results of PCA are displayed as a plot of variance against principal components known as a Scree test, a graphical method first proposed by Cattell [146]. This plot has a negative slope in which any random variability in a data set falls to the right. Variables to the left of where the plot flattens out are the ones of interest, since these have the largest and unexplained variance and are an indication of correlation. The Scree test yields component loadings and scores. Loadings help to interpret spectral variance in a data set such as peak location and shape changes, indicating the correlation between the variables of the original data set and the principal components. Generally, loadings of 0.3 and above are considered to be significant. Scores demonstrate trends or groupings in a data set, which help describe relationships amongst spectra. The principal component weights are used in conjunction with the original variable values to calculate each score. For

example, in the extreme case where there is no significant variability in a group of spectra, the loadings and scores beyond PC1 will contain just noise and scattered points respectively.

To assess the potential influence of the laser power on SLBs, a series of thirteen spectra have been recorded at a single position on a lipid film sample with an exposure time of 10s at powers ranging from 0.5 to 20mW (Figure 6.7).

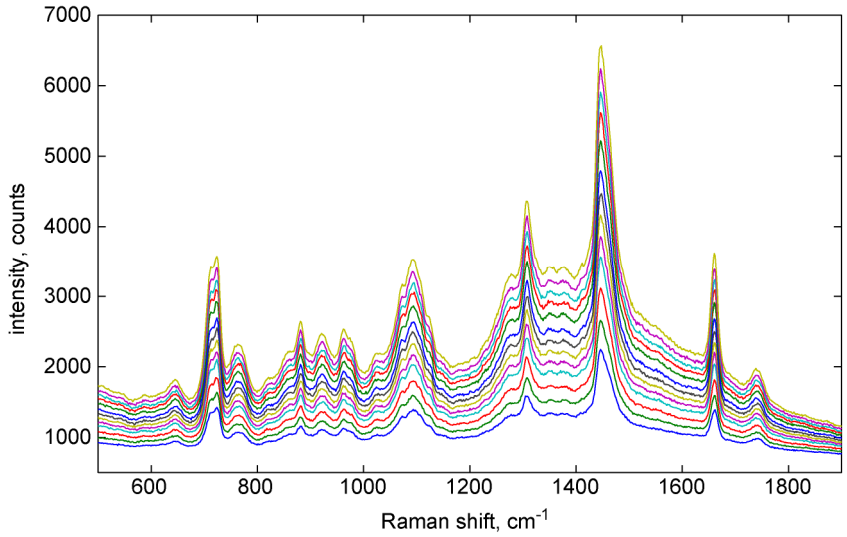

Figure 6.7: Raman spectra taken from one area of the lipid sample at powers of 0.5 to 20mW with 10s exposure.

From the Scree test for this data set, it can be seen that all spectral variation can be accounted for by a single principal component, suggesting that an increase in laser power introduces no change in the lipids for 10s exposure (Figure 6.8). The corresponding mean-centred loadings and scores confirm this (Figure 6.9). Almost all structural variation in the spectra occurs in PC1. The loading of this co-ordinate contains spectra comparable with the original data set whereas higher principal components contain just noise. Similarly, the score of PC1 is a plot of correlated points, whilst principal components beyond this show random variation. These results demonstrate that all spectra in the data set have very similar characteristics and therefore increased laser power has no significant effect on lipids.

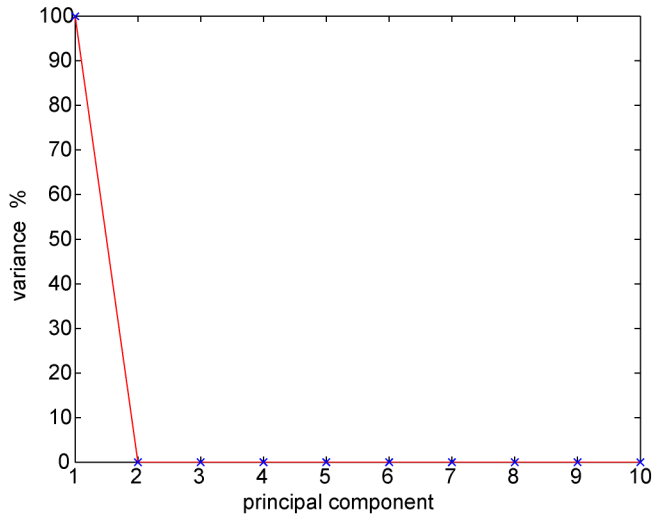

Figure 6.8: The Scree test of the data shown in Figure 6.7.

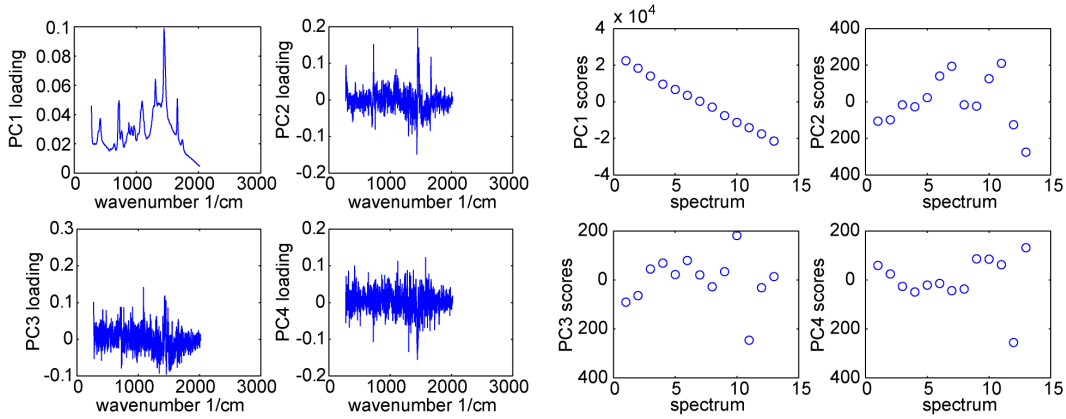

Figure 6.9: The loadings and scores for up to the fourth principal component of the data shown in Figure 6.7.

Experiments have also been carried out to assess whether extended exposure to laser radiation has any effect on SLBs. Ten spectra were recorded consecutively at a single position on a lipid film sample at a power of 1mW over a 10mins period in 1min intervals, each with an exposure time of 10s (Figure 6.10).

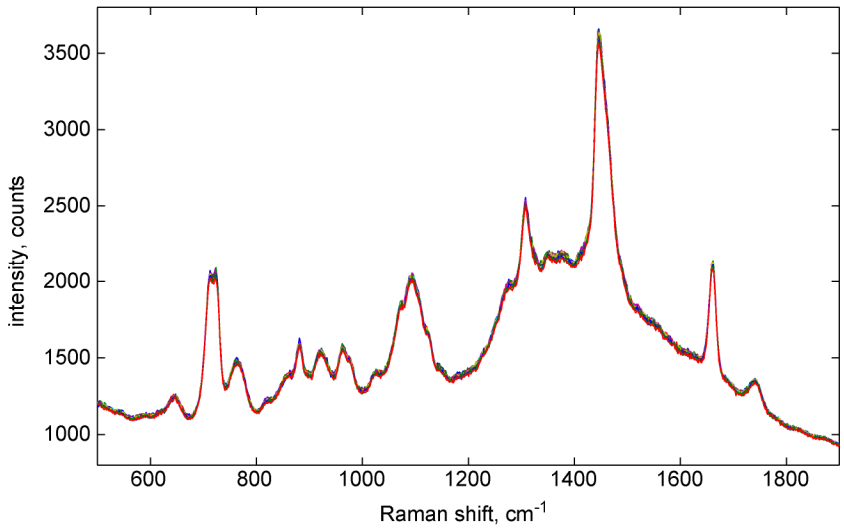

Figure 6.10: Raman spectra taken from one area of the lipid sample at a power of 1mW in 1min intervals up to 10mins.

The Scree test shows that about 80% of all spectral variation can be accounted for by two or three principal components, indicating that exposure to the laser at this power has little effect on the lipids (Figure 6.11). However, this is not an ideal plot, so mean-centred loadings and scores can give a clearer indication of exactly how much effect the laser has on the lipids at prolonged exposures (Figure 6.12). According to the loadings for this data set, only a single principal component shows any spectral variation and beyond this is merely noise. Similarly, correlation is only apparent from the first co-ordinate in the scores. This demonstrates that observed random variations are responsible for any discrepancy in the spectra and therefore long exposure to this laser power has no significant effect on the lipids.

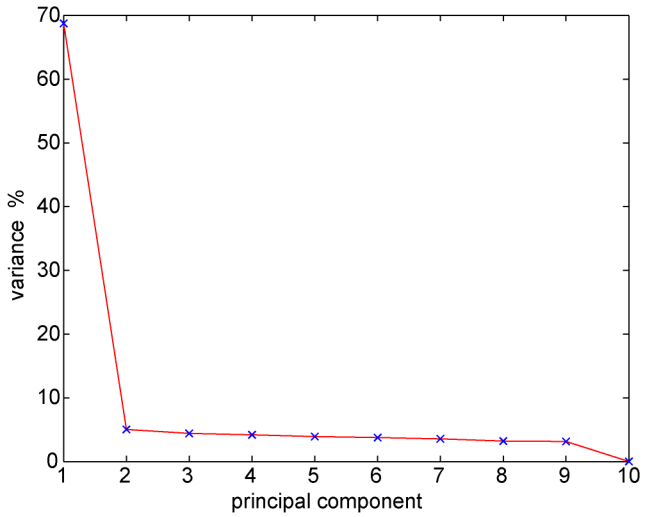

Figure 6.11: The Scree test of the data shown in Figure 6.10.

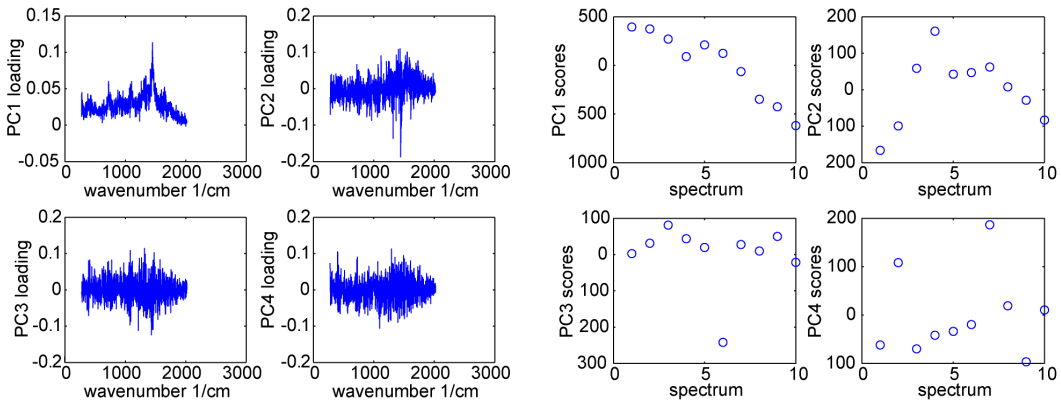

Figure 6.12: The loadings and scores for up to the fourth principal component of the data shown in Figure 6.10.

A data set was also collected at a higher laser power. These spectra were recorded at a single position on a lipid film sample at a power of 15mW over a 10mins period in 1min intervals, again with an exposure time of 10s for each spectrum (Figure 6.13).

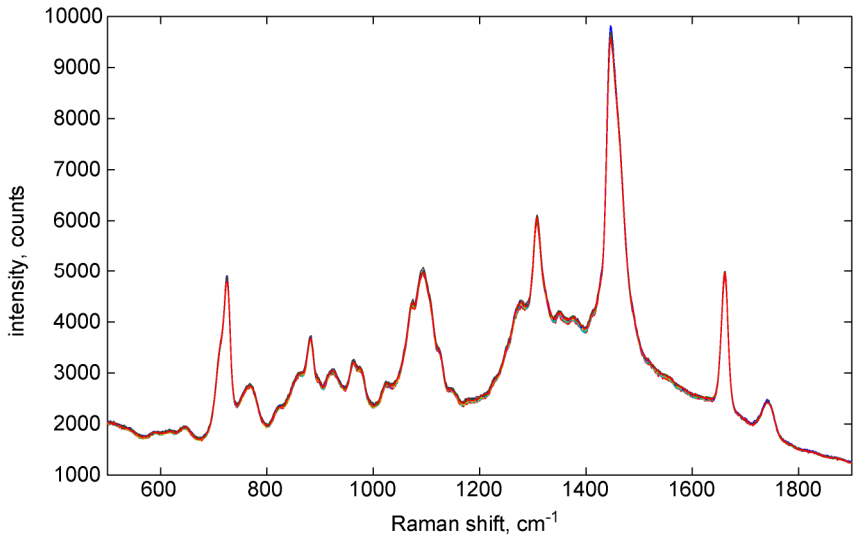

Figure 6.13: Raman spectra taken from one area of the lipid sample at a power of 15mW in 1min intervals up to 10mins.

The Scree test at this laser power shows that spectral variation is contained in three or four principal components, indicating that exposure to the laser at a very high power has a small effect on lipids (Figure 6.14). In the mean-centred loadings of this Scree test, spectral variance becomes apparent in a second co-ordinate. Also there is very little correlation in any of the mean-centred scores (Figure 6.15). These results suggest that high laser powers at extended exposure times have a very slight effect on the spectra of lipids. As expected, prolonged exposure to high laser powers have more effect on the lipids than lower laser powers.

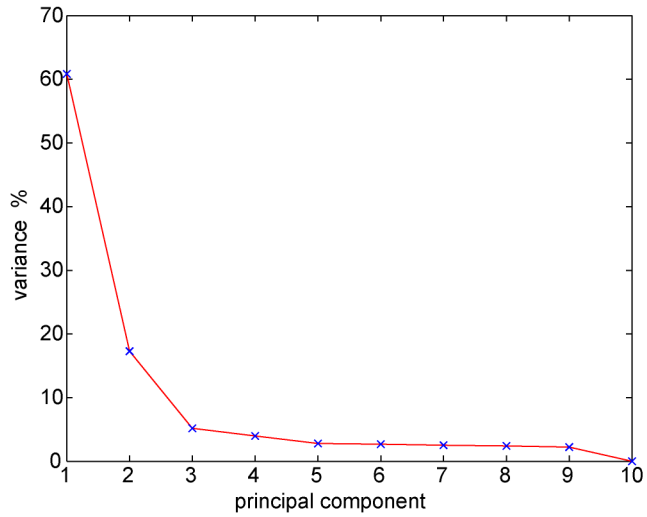

Figure 6.14: The Scree test of the data shown in Figure 6.13.

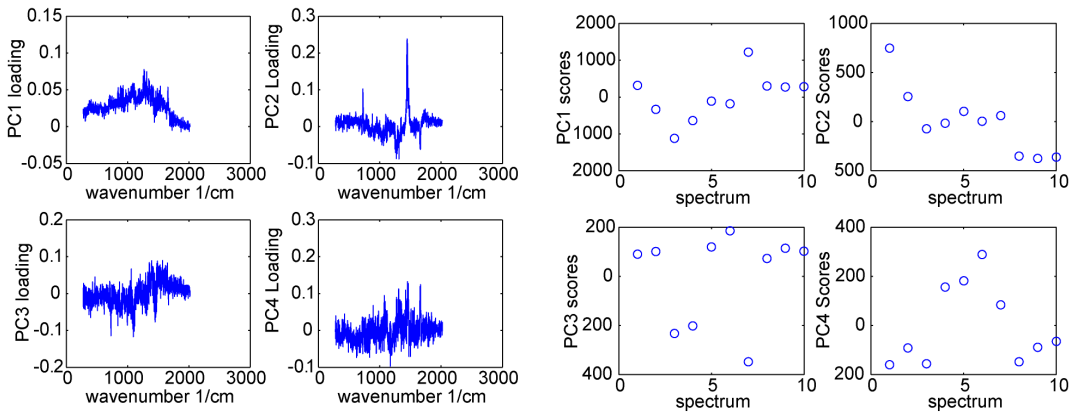

Figure 6.15: The loadings and scores for up to the fourth principal component of the data shown in Figure 6.13.

6.4 AFM imaging and characterisation of SLBs

SLBs have been formed by the vesicle fusion method using phospholipids DPPC and DOPC and studied with AFM. Single and mixed SLBs of DPPC and DOPC were investigated and both exhibited microdomains, determined by phase transitions of the phospholipids [74]. All structures were supported on mica substrates that were firstly cleaved and treated with magnesium chloride ($MgCl_2$) to encourage fusion of the lipid vesicles into a bilayer. The lipid vesicles were left to crash down for at least 3hrs, after which time the sample was washed with water several times to remove excess, unfused vesicles. Samples were imaged at room temperature with tapping mode AFM in water, with triangular silicon nitride probes with a resonant frequency of 12-24kHz and a spring constant of 0.06N/m (Veeco).

DOPC and DPPC each form a single SLB that can be imaged and characterised *in situ* with AFM. It is expected that this structure will not cover the entire substrate and will consequently contain defects (Figure 6.16a). When imaging an SLB these defects, or holes, can be easily detected by AFM. Holes in an SLB vary in area, but it is their depth that is of importance. If this is measured to be consistent with the thickness of a single bilayer, holes can be used to confirm its presence. Phospholipids such as DOPC and DPPC can also form a variety of phase-separated microdomains (Figure 6.16b and c).

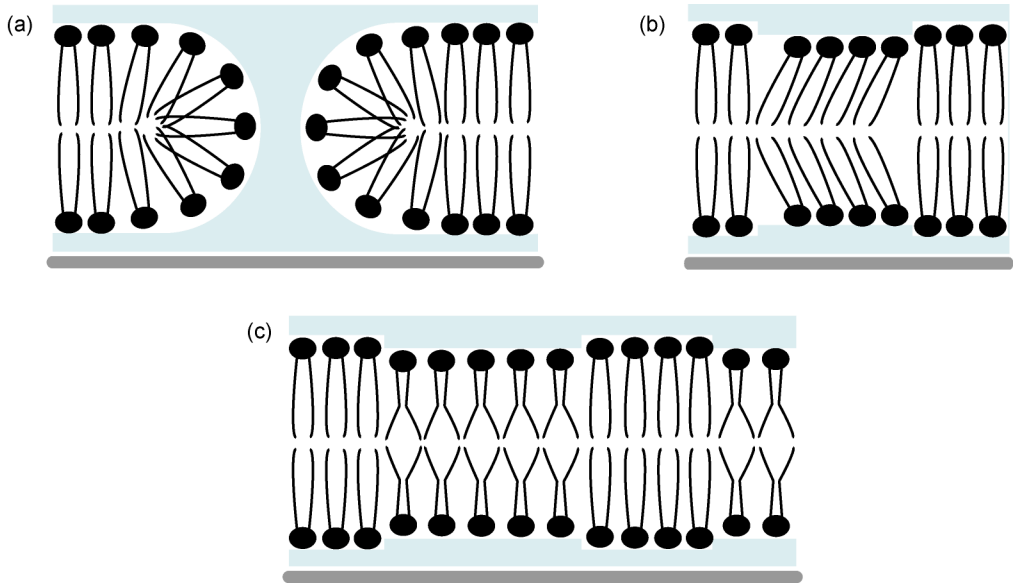

Figure 6.16: Illustration of phases of an SLB (a) Ordered gel state SLB containing a hole (b) Ordered gel phase SLB with microdomains of disordered tilted lipids (c) Mixed SLB consisting of areas of both ordered gel phase lipids and disordered liquid-crystalline phase lipids.

SLBs of DPPC were formed and successfully imaged with AFM (Figure 6.17). The darker areas in the image are the substrate detected through holes in the SLB whilst any white spots are unfused vesicles that have remained on the surface of the structure after washing. The thickness of a single bilayer of DPPC is 4.7nm at room temperature [147], which can be confirmed by topography line profiles taken along a single scan line of the AFM image that contains holes.

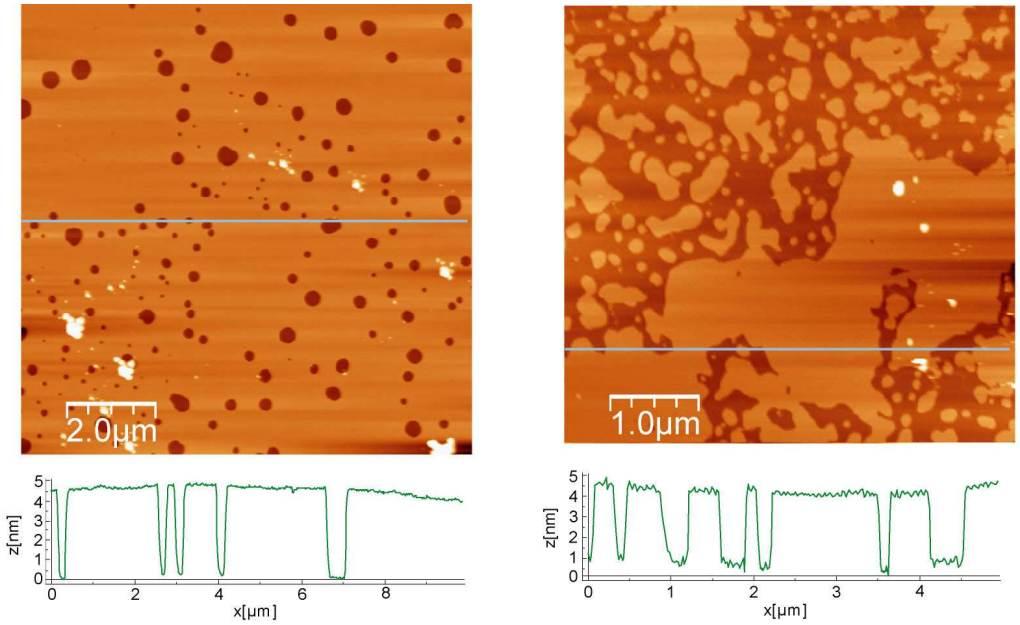

Figure 6.17: AFM images and corresponding line profiles of a single DPPC SLB (for comparison of synthesis methods, the image on the left is of a bilayer formed by the LB technique).

As well as holes being evident in these SLBs, some single bilayers of DPPC form mid-height regions of lipids around a nanometre below the surface of the bilayer (Figure 6.18). These regions are a type of microdomain composed of tilted lipid molecules in a slightly disordered lipid phase compared with the rest of the SLB [26]. These microdomains are apparent from a line profile across the appropriate area as well as histograms of the statistical distribution of heights across the image; the change in topography between the mica substrate (S), microdomains (M) and the top surface of the bilayer (B) can be determined from the difference in peaks in the histogram.

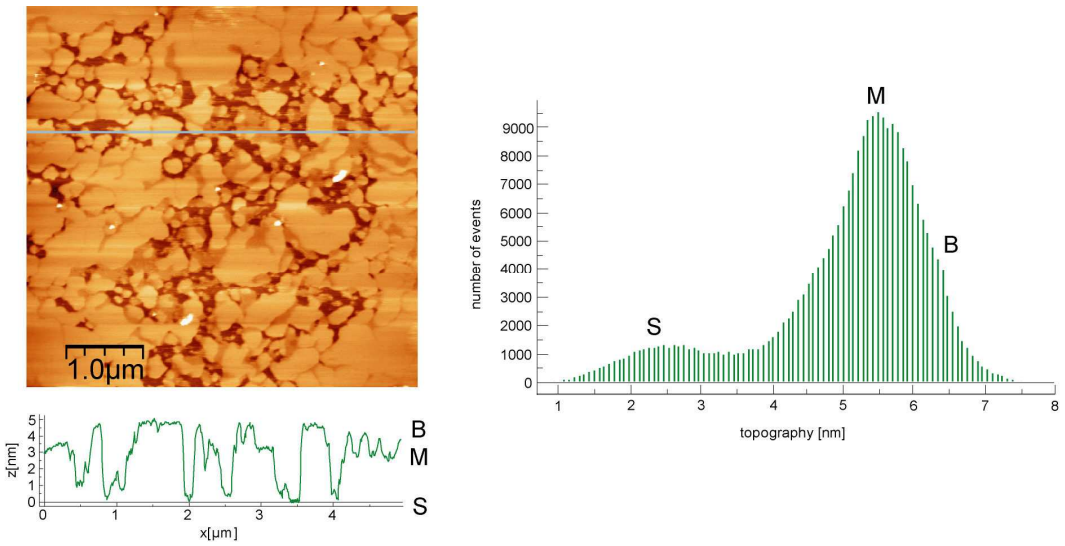

Figure 6.18: AFM image, line profile and height distribution histogram of a single DPPC bilayer containing microdomains (see text for notations).

Similarly, single SLBs of DOPC were created and imaged with the AFM (Figure 6.19). All structures contained holes consistent with the thickness of a single bilayer of DOPC, which is 3.7nm at room temperature [147]. Also, as with the DPPC SLB, there is evidence of microdomains about a nanometre shorter than the rest of the bilayer from a line profile and height distribution histogram.

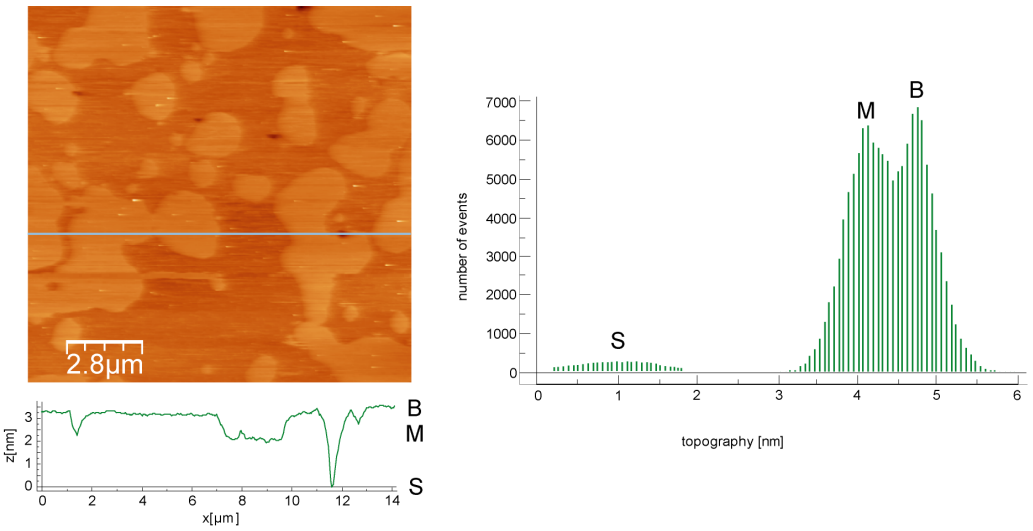

Figure 6.19: AFM image, line profile and height distribution histogram of a single DOPC bilayer containing microdomains (see text for notations).

Phospholipids can also be combined to form mixed SLBs. Some combinations of lipids readily form phase-separated microdomains, small areas in the bilayer that

arise from temperature-dependant phase transitions of the different lipid molecules. Phase transitions in lipids occur for many reasons such as hydrocarbon chain length, unsaturation, asymmetry and branching, as well as the type and position of chain attachment to the glycerol backbone [75]. These factors lead to lipids having different thermodynamic properties including the temperature at which they are in a certain phase. This is the case for DPPC and DOPC and the reason why they form microdomains when mixed in an SLB (Figure 6.20). DPPC undergoes phase transition from a gel to a liquid-crystalline state at about 41°C, whilst this change occurs at around -18°C for DOPC due to its carbon-carbon double bonds. Therefore when both DPPC and DOPC are present in a bilayer structure, they are in two different phases over a large range of temperatures. This includes room temperature, at which an SLB of DPPC and DOPC consists of regions of a saturated lipid-rich gel phase amongst a bilayer of unsaturated lipid-rich disordered liquid phase.

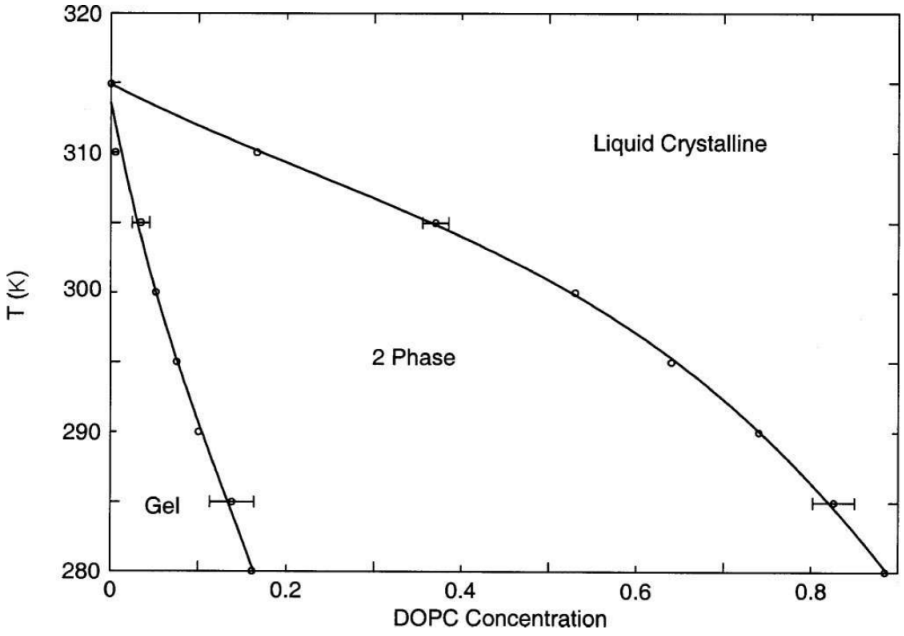

Figure 6.20: Phase diagram for an SLB composed of DPPC and DOPC as a function of the volume fraction of DOPC [75].

Microdomains are evident from line profiles and height distribution histograms of AFM images of mixed SLBs of DOPC and DPPC (Figure 6.21), in which areas consisting of DPPC protrude about 0.9nm from the rest of the bilayer.

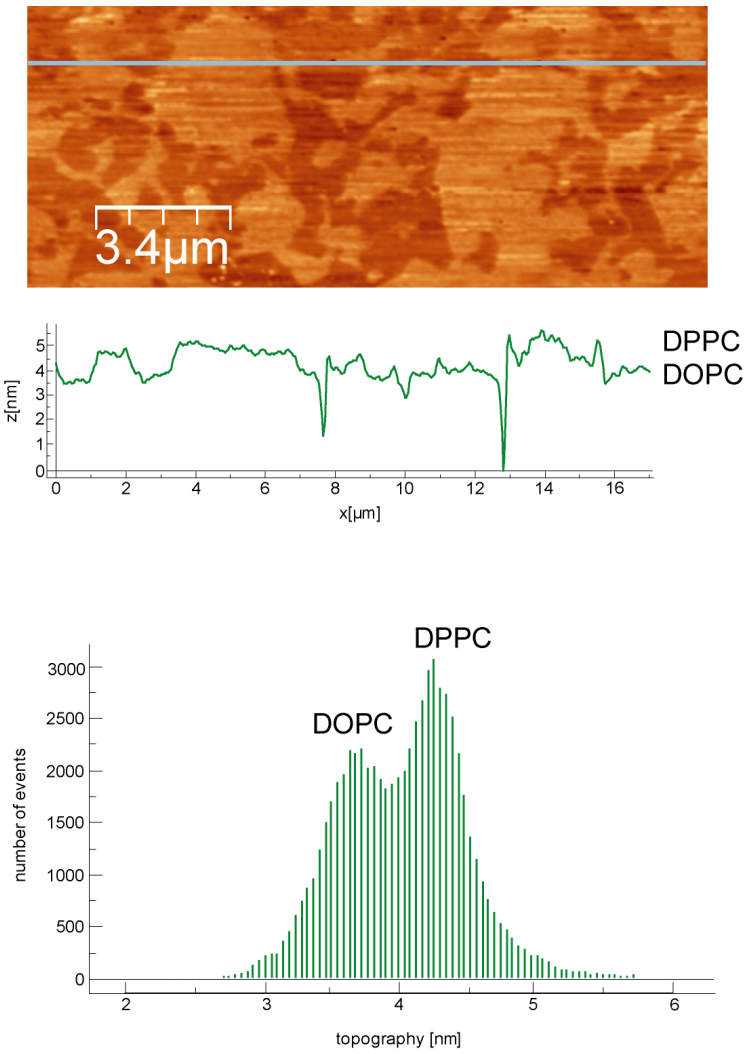

Figure 6.21: AFM image, line profile and height distribution histogram of a DPPC/DOPC SLB.

6.5 Detecting multilayer SLBs with Raman spectroscopy

Raman spectra of DPPC and DOPC in multilayered structures have been measured with RMS (Figure 6.22). The assignment of Raman bands for phospholipids is shown in Table 6.1. Notable Raman bands include carbon-carbon double bond in-plane bending at 953cm^{-1} and stretching at 1641cm^{-1}, only present in the spectra of DOPC at room temperature.

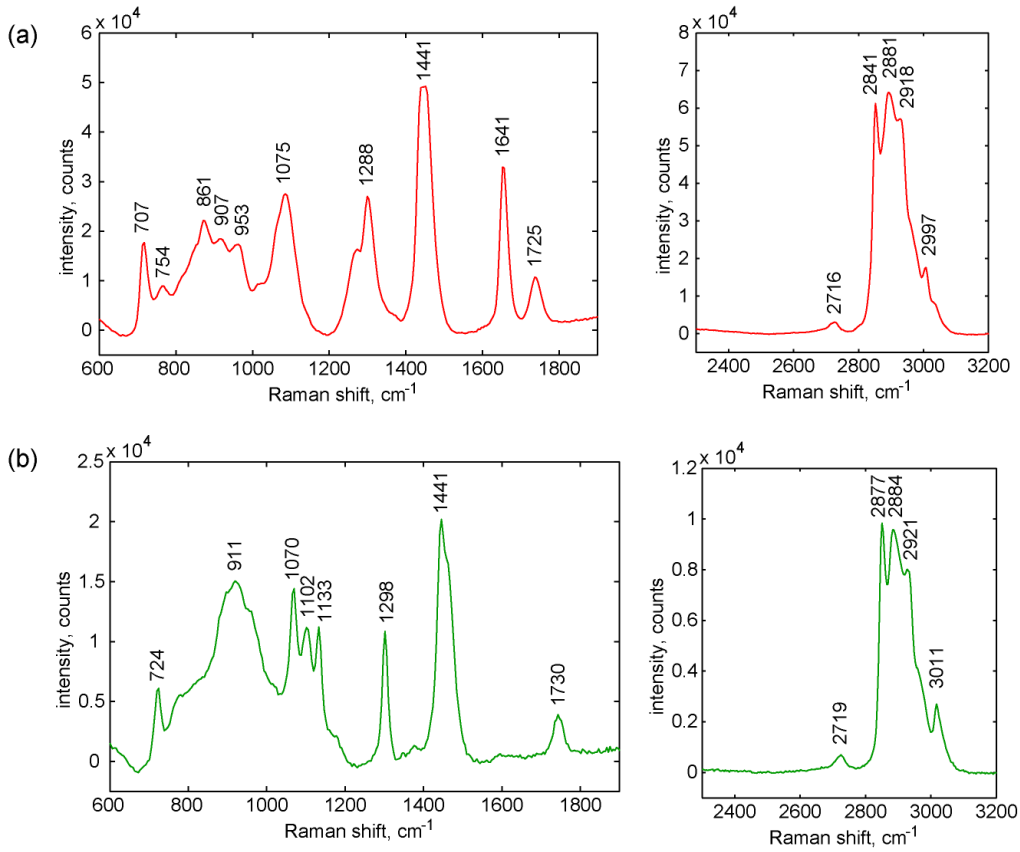

Figure 6.22: Raman spectrum of (a) DOPC and (b) DPPC in multilayered structures.

Raman band position, cm^{-1}	assignment
800 - 920	C-C stretching
945 - 970	C=C in-plane bending
1060 - 1135	C-C stretching
1250 - 1280	=C-H bending
1295 - 1305	C-H twisting deformations
1400 - 1500	CH scissoring deformations
1640 - 1680	C=C stretching
1730 - 1750	C=O stretching
2700 - 3015	C-H stretching

Table 6.1: Assignment of Raman bands of phospholipids [148].

Previously, sapphire was chosen as a suitable substrate for the experimental setup and both AFM and Raman spectroscopy, with the potential to investigate SLBs. It is transparent and has very little roughness or Raman scattering. However, sapphire is not a common substrate for SLB studies. In light of these findings, a DPPC bilayer

was successfully formed on sapphire and imaged with AFM (Figure 6.23). The sapphire was annealed at 1100°C for 2hrs to produce a clean and flat surface. It was then etched with a piranha solution of 3:1 sulphuric acid and hydrogen peroxide (H_2SO_4:H_2O_2) (Sigma Aldrich, UK) for further cleanliness and also hydrophilicity. Finally, it was treated with $MgCl_2$ in the same way as mica. DPPC vesicles were prepared via the vesicle fusion method, which were then deposited onto the prepared sapphire and left to form a bilayer across the surface, resulting in a DPPC SLB on sapphire. Recently, the formation of SLBs on sapphire and their evolution across step and terrace structures has been investigated [149].

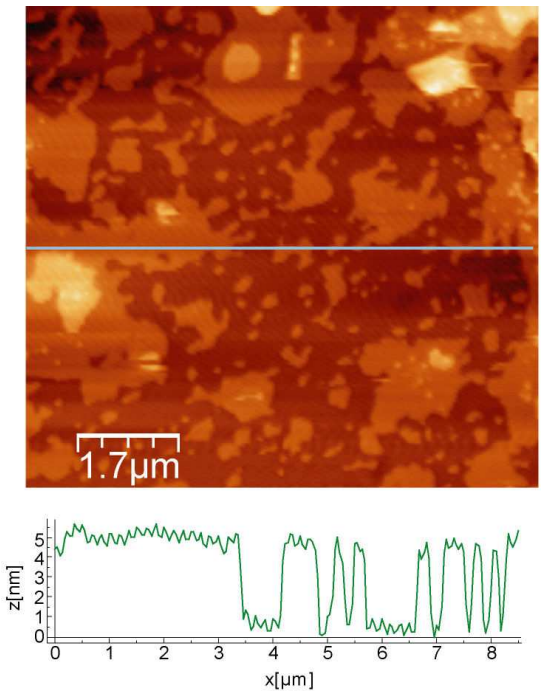

Figure 6.23: AFM image and corresponding line profile of a DPPC SLB on sapphire.

Despite this progress, a single SLB was not detectable with the RMS system described in the previous chapter. The spatial resolution of the setup has been optimised by the combination of a water-immersion, high numerical aperture objective and confocal system to improve the collection of scattering from small samples by tight focusing of the laser and rejection of out-of-focus signal. However, this setup lacks the sensitivity required to detect the weak scattering from SLBs with RMS.

6.6 Conclusions

The combined AFM-Raman system has been investigated for studying SLBs with RMS. Firstly, it was established that a number of substrates are suitable for detecting scattering of small structures with this setup. In terms of their own Raman scattering, the spectra of quartz, MgF_2 and sapphire have few Raman bands and little overall background. However, only sapphire was deemed appropriate for AFM studies of SLBs, as it can be treated to provide a surface with almost no roughness. Secondly, a range of laser powers and exposure times were investigated for their effect, if any, on lipid molecules. By statistical analysis of spectra, it was found that only prolonged exposure to a high laser power had any effect on the Raman spectrum of lipids.

A variety of SLBs have been created and then imaged and analysed with AFM. Single and mixed SLBs of DPPC and DOPC were characterised by topography line profiles and height distribution histograms, measuring a bilayer height of 4.7nm for DPPC and 3.7nm for DOPC. Microdomains were observed in all SLBs. Single SLBs contained a tilted lipid phase about a nanometre below the rest of the bilayer. Mixed SLBs containing both DPPC and DOPC formed phase-separated microdomains that protrude 0.9nm from the rest of the bilayer. Raman spectra of DPPC and DOPC in multilayered structures have been measured and Raman bands have been identified. Also, SLBs have been deposited onto sapphire substrates and imaged with AFM. However, the detection of a single SLB was not possible with this RMS setup and the sensitivity currently achievable.

Chapter 7

Surface-enhanced Raman spectroscopy

Progress towards studying an SLB with SERS is reported here. A key part of this work is the development of suitable SERS-active substrates to combine with the AFM-Raman system. NSL substrates are characterised and optimised for providing both the level of enhancement required to detect an SLB and the uniformity of SERS signal necessary to chemically image phase-separated microdomains. SERS spectra and mappings are analysed for various molecular monolayers and a fatty acid bilayer. Supported by calculations and modelling, these experiments demonstrate the potential of the experimental setup for label-free imaging of phospholipid SLBs.

7.1 Introduction

Potentially, Raman microspectroscopy (RMS) can provide the spatial resolution required to image supported lipid bilayers (SLBs) and microdomains. However, the sensitivity of the system is still too low to chemically detect these structures. The inclusion of a confocal system removes most out-of-focus photons to isolate the Raman scattering from the sample of interest. However, in the case of a single SLB, this scattering is too weak to be detected with this setup alone. Thus detection of the Raman spectra of SLBs requires significant enhancement, which can be achieved with surface-enhanced Raman spectroscopy (SERS).

In the past decade, SERS has become a widely used derivative method of Raman spectroscopy. The enhancement it provides originates from increased electric fields that arise from the plasmon resonances of rough, metallic surfaces [54, 55]. SERS can be performed on a standard Raman spectroscopy system, with no direct modification to the experimental setup. The only addition is a SERS-active substrate consisting of metallic nanoparticles or nanostructures. However, this substrate is key to the success of the technique. In general, it is the most important aspect of any research employing SERS and consequently much of the work in this field has focused on the design and development of SERS-active substrates [150, 151]. Often these substrates are produced in-house so that they can be created precisely for the desired sample and application.

A nanosphere lithography (NSL) substrate has been developed, characterised and optimised for imaging SLBs with the combined atomic force microscopy (AFM) – Raman system and SERS. The main requirement of any SERS substrate is to provide high and reproducible enhancement that is sufficient enough to enable measurement of spectra from the sample. In this case, it is also important that this is achieved without disturbing the planar structure of an SLB. Therefore the substrate must have a nanoscale roughness that is compatible with both activating SERS and supporting a single SLB. In addition, the enhancement must be consistent and uniform at a micrometer scale to allow detection of spatially resolved chemical features such as those associated with microdomains in a mixed SLB. Finally, the setup has an inverted configuration to allow for the integration of an AFM and studies of biological materials in aqueous environment. This means that a suitable SERS substrate must be optically transparent.

7.2 Development of NSL substrates for SERS

Large-scale, two-dimensional (2D) arrays of truncated tetrahedral nanostructures were formed [152] to create NSL SERS-active substrates [153]. NSL is a common technique that has been extensively used to fabricate periodic arrays of nanoparticles upon solid surfaces [154] and more recently developed for optical applications [112]. This type of substrate is now a popular choice for SERS studies, as it can be entirely custom-made to requirements and is known to provide reliable enhancement of

Raman scattering in the range ~10^4-10^8 [113]. Typically, NSL substrates are prepared via the evaporation of a metallic thin film over hexagonally close-packed spheres that are later removed. This is the technique adopted here.

An evaporation mask of a nanosphere monolayer was prepared using monodisperse polystyrene spheres with a diameter of 384 and 1002nm, 10wt.% in water (Varian, Inc) mixed with an equal amount of ethanol (Sigma Aldrich, UK). A silicon (111) wafer (PI-KEM, UK) was cut into 3×2cm substrates. Alongside 22mm diameter glass coverslips (VWR International), these pieces of silicon were cleaned with a variety of solvents and etched with a piranha solution of 3:1 sulphuric acid and hydrogen peroxide (H_2SO_4:H_2O_2) (Sigma Aldrich, UK) for hydrophilicity. The silicon substrates were then kept in 10% sodium dodecyl sulphate (Sigma Aldrich, UK) solution overnight to encourage nanosphere ordering. About 4µl of the prepared solutions of polystyrene spheres was applied to the surface of a silicon substrate and distributed using a Microman pipette (Gilson, Inc). This substrate was very slowly immersed into a 15cm diameter glass beaker (Schott Duran) filled with ultrapure water, floating the nanosphere monolayer on the water surface. Then 4µl of 2% sodium dodecyl sulphate solution was added to change the water surface tension and consolidate the polystyrene spheres to form a large area of highly ordered hexagonally close-packed monolayer. This monolayer was slowly lifted off the surface of the water onto previously mentioned glass coverslips. A ~25nm thin film of silver was thermally evaporated in vacuum (Edwards) onto these coverslips at a pressure of 10^{-7}mbar and evaporation rate of 0.3-0.4nm/s. Finally, the coverslips were immersed in tetrahydrofuran (Sigma Aldrich, UK) for 15min and then kept in an ultrasonic bath for 20s to dissolve and remove the polystyrene spheres. The coverslips were then washed with ethanol and dried, resulting in a glass substrate of large-scale, 2D arrays of truncated tetrahedral nanostructures of silver (Figure 7.1).

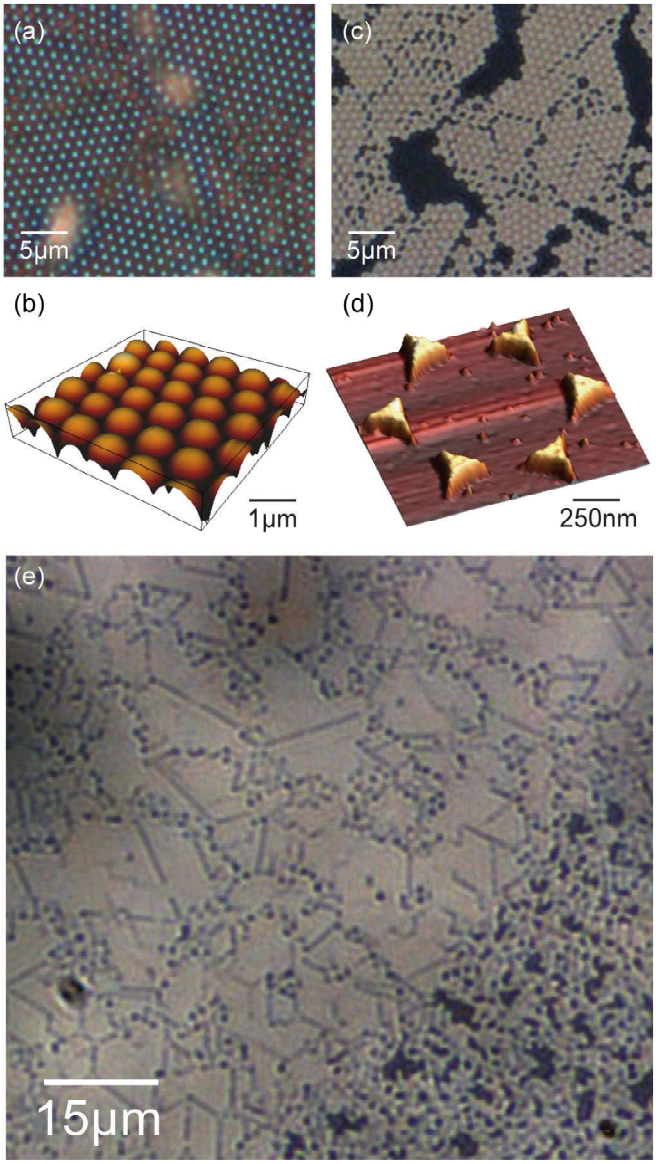

Figure 7.1: NSL substrates at different stages in their development (a) Optical image at 60x magnification and (b) 3D AFM image of highly ordered hexagonally close-packed monolayer of polystyrene spheres (c) Optical image at 60x magnification, (d) 3D AFM image and (e) Optical image at 20x magnification of a large-scale, 2D array of truncated tetrahedral silver nanostructures.

7.3 Characterisation of SERS substrates

7.3.1 Spatial measurements with AFM

All substrates were firstly characterised with AFM, focusing on the dimensions, scale and ordering of the silver truncated tetrahedral nanostructures. Measuring these physical aspects is essential for ensuring the large-scale ordering of nanostructures that will activate high and consistent enhancement across the substrate. Collective

resonances from areas of tens of microns of these nanostructures are key to achieving localised electric field optimisation and in turn optimised SERS activity [150].

Substrates were imaged with tapping mode AFM, with rectangular silicon probes with a resonant frequency of 70 kHz and a spring constant of 2N/m (Veeco). The size of individual nanostructures and the extent of ordering across the substrate is apparent from a standard topographical AFM image and line profile (Figure 7.2a). A firmer indication of the ordering can be achieved from measuring a 2D fast Fourier transform (FFT) from this image (Figure 7.2b); the concentric periodic structure reveals the length scale of the nanostructures within the substrate and more importantly high hexagonal order. This data demonstrates the suitability and potential of these substrates for activating SERS; however, a quantitative measure of this enhancement can be derived from further analysis with Raman spectroscopy, calculations and simulations.

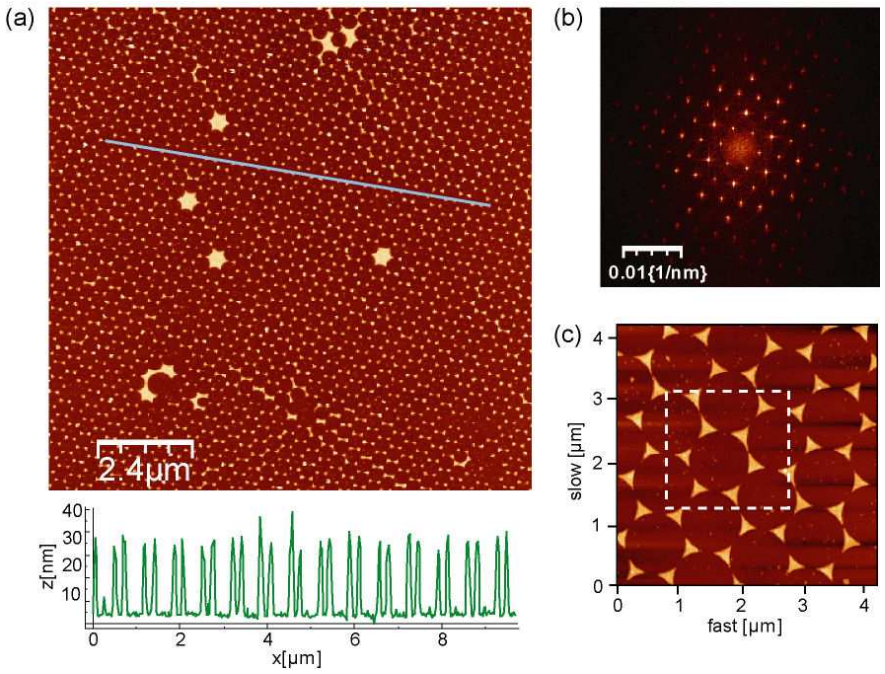

Figure 7.2: NSL substrates characterised for SERS (a) Large AFM image and line profile of a typical substrate (b) 2D FFT of the presented image (c) Small AFM image, highlighting a typical area used in SERS mapping.

7.3.2 SERS spectra and mappings of molecular monolayers

The SERS activity of the substrates was investigated with monolayers of rhodamine 6G (R6G) and p-aminothiophenol (p-ATP) (Sigma Aldrich, UK). R6G is a large fluorescent dye molecule. Exposing this molecule to visible wavelengths excites its fluorescence, which is broad and intense and totally covers its weaker Raman scattering. However, as well as increasing useful signal, SERS strongly quenches fluorescence. Therefore obtaining the Raman spectrum of R6G on the substrates is a good indication of successful SERS. p-ATP is an aromatic compound that contains a thiol group (–SH). This group has a high affinity to metal enabling the molecule to adsorb to a SERS substrate and form a single monolayer. At the scale of a monolayer Raman scattering is extremely weak, therefore any signal detected at low laser powers and short exposure times must arise from SERS. For these reasons, both R6G and p-ATP are commonly used in SERS studies [155-157].

The substrates were immersed in 1mM R6G and 10^{-4}M p-ATP methanol solutions for 2hr and then rinsed in methanol to ensure one molecular layer was adsorbed. The prepared substrates were initially imaged with the AFM to locate a large ordered area of at least 15×15μm containing a monolayer of molecules, ideal for performing SERS mapping. Within this image a 1-2μm^2 region was selected to record a chemical mapping (Figure 7.2c). Mappings were constructed by automated scanning of the sample through the focus of the laser, with a spatial resolution of less than 1μm and a laser power of 20μW. Samples were moved in a raster pattern with step sizes of 50-100nm, acquiring a SERS spectrum at each position at a rate of 2s per pixel. The area of a Raman band in each spectrum was calculated after subtraction of a local linear baseline and used to build a spectral mapping one pixel at a time. This mapping was then related back to the original AFM image, enabling direct correlation between SERS nanostructures and Raman scattering to reveal the exact position, orientation and uniformity of enhancement across the substrate.

Before taking any spectroscopy measurements of molecules on the SERS substrates, the Raman scattering from a bare substrate was recorded for subtraction from subsequent measurements (Figure 7.3). However, the substrates themselves were

found to have no Raman signal. Therefore no background was removed from the spectra to follow.

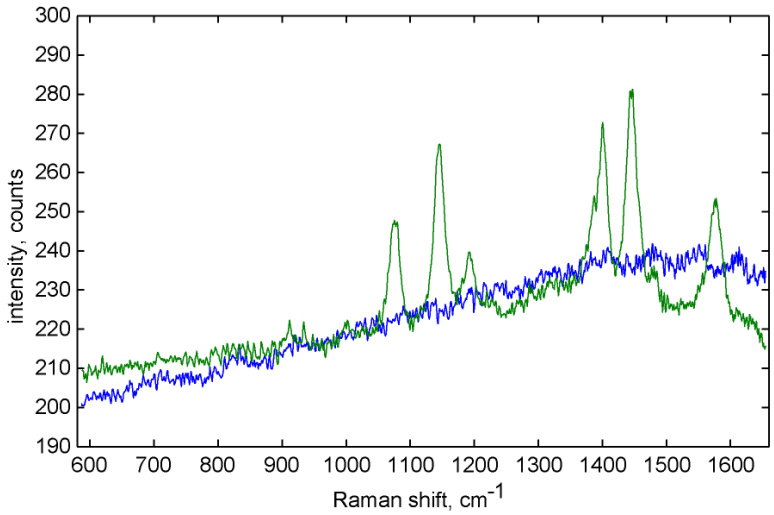

Figure 7.3: Typical SERS spectrum of p-ATP (green) and background signal from the substrate with no molecules (blue).

Substrates formed from both 384 and 1002nm polystyrene spheres were mapped with monolayers of R6G (Figure 7.4) and p-ATP (Figure 7.5). Raman bands at 1363cm^{-1} (aromatic C–C stretching and C–N stretching) and 1143cm^{-1} (C–H bending and NH_2 rocking) were used to create the mappings of R6G and p-ATP respectively. For both molecules, the mappings of the 1002nm substrates provide information about the distribution of SERS enhancement, since the structure of the substrates can clearly be seen from the mappings. When compared to the AFM images taken of the same areas, regions of higher intensity pixels correspond to the position and orientation of the silver nanostructures whilst weaker SERS scattering was detected in between these nanostructures. This suggests that for this type of substrate the SERS effect arises from the metallic surfaces themselves rather than the gaps between them. The mappings of the 1002nm substrates also exhibit some very bright pixels, again occurring at positions where the nanostructures are situated, assumed to be SERS "hot-spots". On the other hand, individual nanostructures and features are indistinguishable from the mappings of the 384nm substrates. Instead, these substrates provide a consistent enhancement of the Raman signal. The spatial resolution of a Raman spectroscopy system has an intrinsic lower threshold set by the diffraction limit, which is about 500nm for this setup. In most cases this is a negative

aspect as it restricts the size of surface features that can be resolved. However, using SERS substrates with nanostructures smaller than this limit provides enhancement that appears to be distributed evenly across the substrate. Therefore the 384nm substrates could be suitable for investigating non-uniform samples such as mixed SLBs, for which variation in SERS scattering across the sample can be used for spatially resolving the physiochemical properties of lipid microdomains.

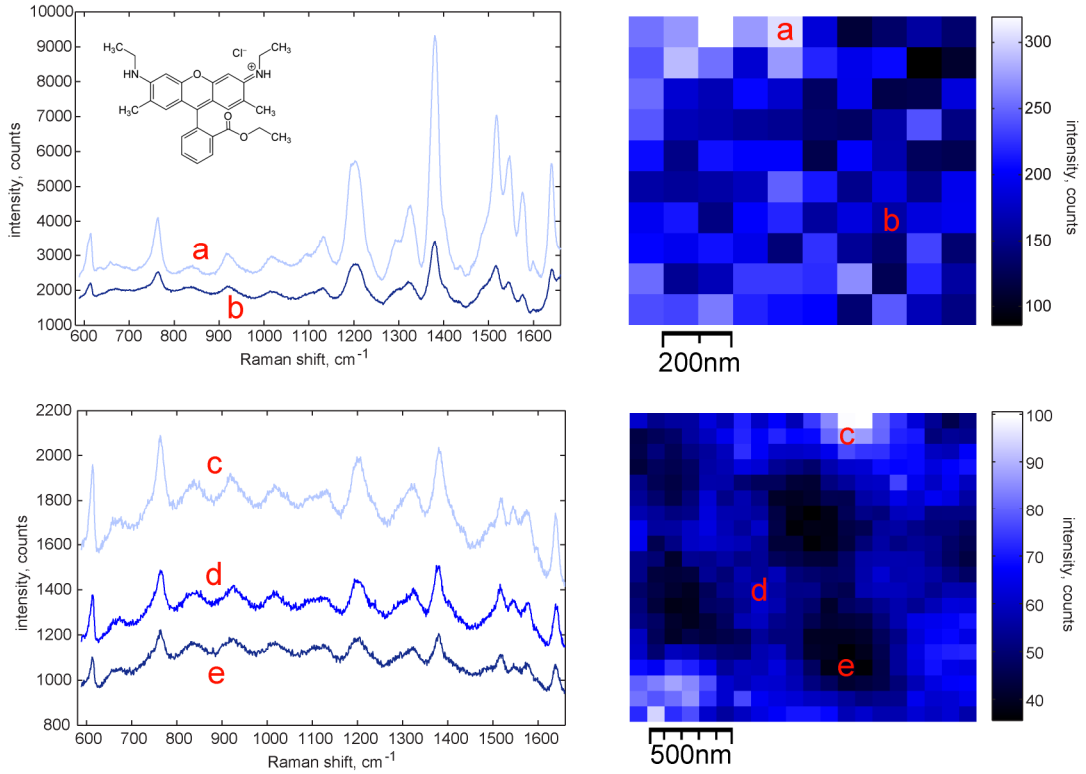

Figure 7.4: SERS spectra and mappings of R6G on 384nm (top) and 1002nm (bottom) substrates. Labelled spectra correspond to the scattering measured at the position of the same labelling in the mappings.

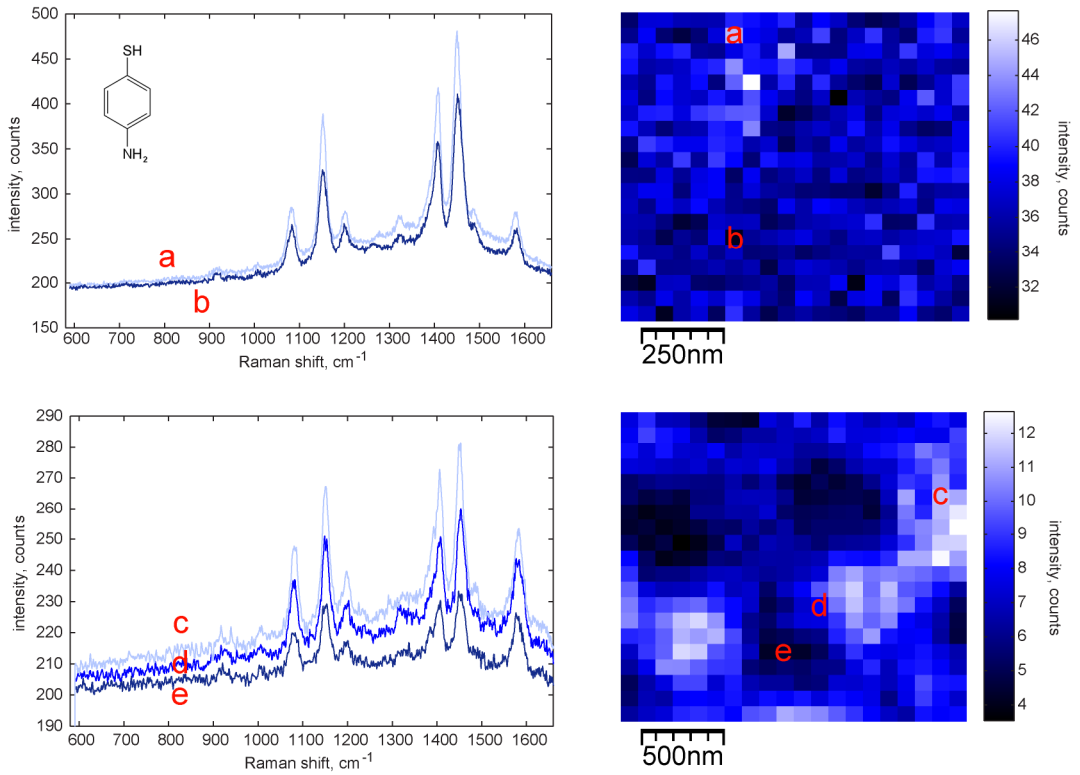

Figure 7.5: SERS spectra and mappings of p-ATP on 384nm (top) and 1002nm (bottom) substrates. Labelled spectra correspond to the scattering measured at the position of the same labelling in the mappings.

In addition, after repeatedly recording mappings over an area of the substrate the SERS signal appeared to reduce. It was observed from consecutive mappings of an R6G monolayer on a 1002nm substrate (Figure 7.6). Firstly, two mappings were recorded one after the other of the same 2μm^2 area. The second mapping showed a universal drop in intensity. Then a 4μm^2 mapping covering the same region was recorded. This larger mapping has an area in the centre that is significantly lower in intensity than the pixels around it, which corresponds to the position of the original two mappings. This loss of SERS intensity has been seen previously and deemed irreversible [68]. It is believed to be associated with the localised heating caused by the high electric fields that the SERS effect originates from.

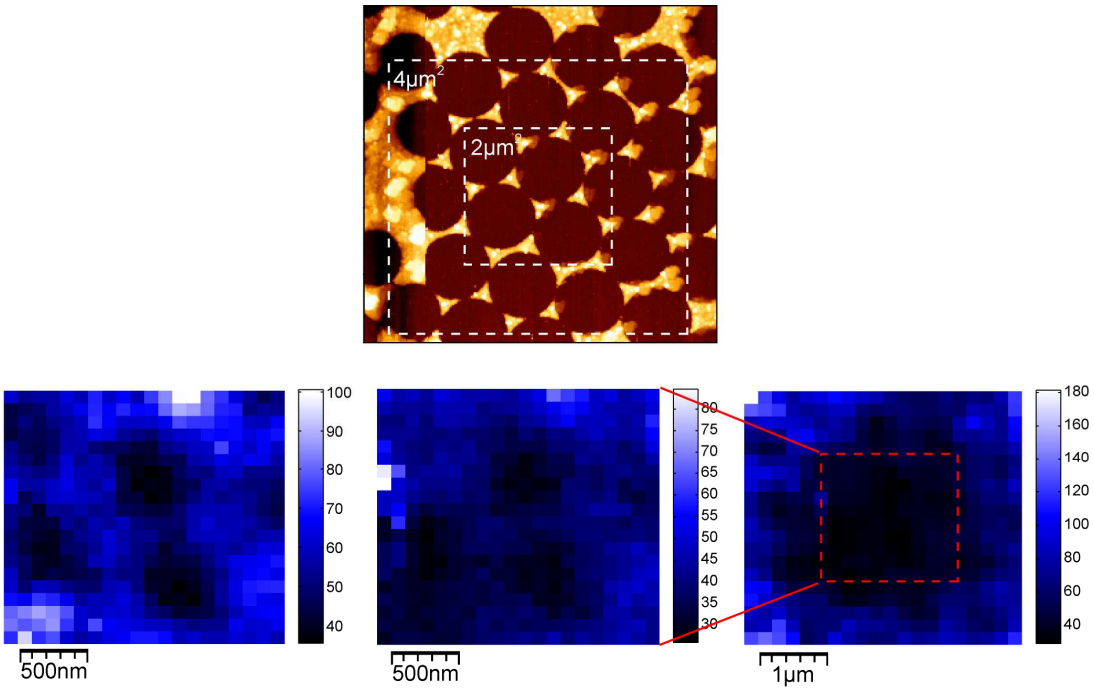

Figure 7.6: Sequential SERS mappings of an R6G monolayer on a 1002nm substrate, demonstrating a loss of SERS signal after repeated mappings of the same area. AFM image highlights mapping areas.

7.3.3 Calculation of enhancement factor

The enhancement factor *EF* of both substrates was calculated by comparing the area of a p-ATP Raman band from the SERS spectra (I_{SERS}) with the area of the same band of unenhanced Raman scattering from a neat solution of the molecule on a bare glass coverslip (I_{RS}) (Figure 7.7). This value was calculated from the point of view of the substrate [158], given by

$$EF = \frac{I_{SERS} / (\mu_M \mu_S A_M)}{I_{RS} / (c_{RS} H_{eff})} \tag{7.1}$$

where μ_M is the surface density of the individual nanostructures producing the enhancement, μ_S is the surface density of molecules on the metal, A_M is the surface area of the metallic nanostructure, c_{RS} is the concentration of the solution used for the non-SERS measurements and H_{eff} is the effective height of the scattering volume of the Raman spectroscopy system.

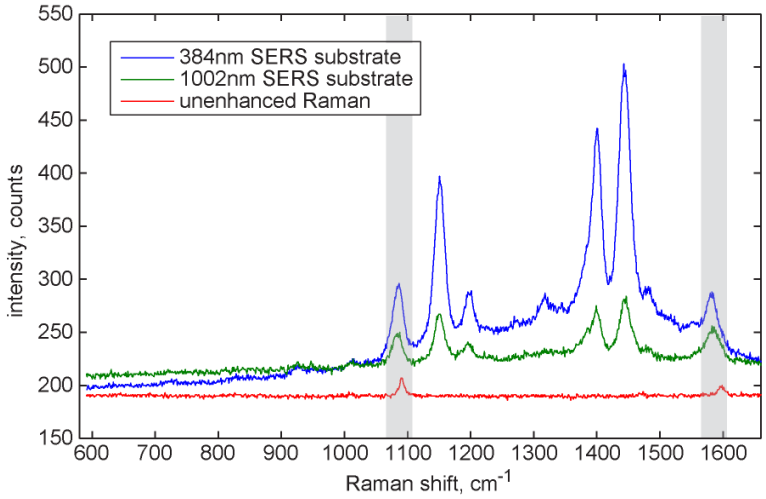

Figure 7.7: A selection of the spectra used to calculate *EF* for each of the SERS substrates (Raman bands used for I_{SERS} and I_{RS} are highlighted).

Two different p-ATP Raman bands and several concentrations of neat solution c_{RS} were used for the intensities I_{SERS} and I_{RS} and then averaged to give the final enhancement factor for each substrate. The values of μ_M and A_M for the two substrates were calculated from geometry. Since the SERS substrate is constructed from hexagonally close-packed spheres, μ_M is the number of nanostructures within the area of a hexagon with sides the length of the nanosphere diameter D (Figure 7.8a). Therefore,

$$\mu_M = \frac{6}{\frac{3\sqrt{3}}{2}D^2} \tag{7.2}$$

This value was calculated to be 1.57×10^{-5}nm^{-2} for the 384nm substrates and 2.30×10^{-6}nm^{-2} for the 1002nm substrates. The area A_M was calculated from

$$A_M = \sqrt{3}d_m\left(2a_{SL} - d_m\right) + \frac{\sqrt{3}\left(a_{SL} - d_m\right)^2}{3} \tag{7.3}$$

where d_m is the thickness of the metal deposition (or the height of the nanostructures) and a_{SL} is the in-plane particle diameter defined as the perpendicular bisector of the largest inscribed equilateral triangle that fills the base of the nanostructures [159, 160]. The value of d_m is 25nm for both substrates. From geometry, a_{SL}, is defined as

$$a_{SL} = \frac{3}{2}\left(\sqrt{3} - 1 - \frac{1}{\sqrt{3}}\right)D \tag{7.4}$$

which is 89.5nm for the 384nm substrates and 233.5nm for the 1002nm substrates. This value is related to the interparticle spacing of the nanostructures $d_{ip,SL}$, which is 221.6 and 578.2nm for the 384 and 1002nm substrates respectively and is given by

$$d_{ip,SL} = \frac{D}{\sqrt{3}} \tag{7.5}$$

Therefore, A_M was calculated to be 9066nm^2 for the 384nm substrates and 44227nm^2 for the 1002nm substrates. Kinetic studies estimate a coverage area of 22Å^2 per molecule for a close-packed monolayer of p-ATP [161], giving 4.5nm^{-2} for the value of μ_S for this setup. H_{eff} was measured directly from the experimental setup by measuring the Raman scattering as the laser was focused through a silicon wafer. The opaque nature of silicon means that it is strongly absorbent, therefore all the Raman signal detected comes from the silicon wafer surface (and therefore from the focal plane at z=0μm). The peak area of the 520cm^{-1} Raman band of silicon is measured as a function of distance from this focal plane and plotted as an intensity-distance profile (Figure 7.8b). The profile is bell-shaped and shows a gradual decrease in Raman intensity either side of z=0μm. H_{eff} is the full width at half maximum (FWHM) of this plot, which is measured as 21.2μm. This value depends on the numerical aperture of the microscope objective and the size of the spectrometer slit of the experimental setup.

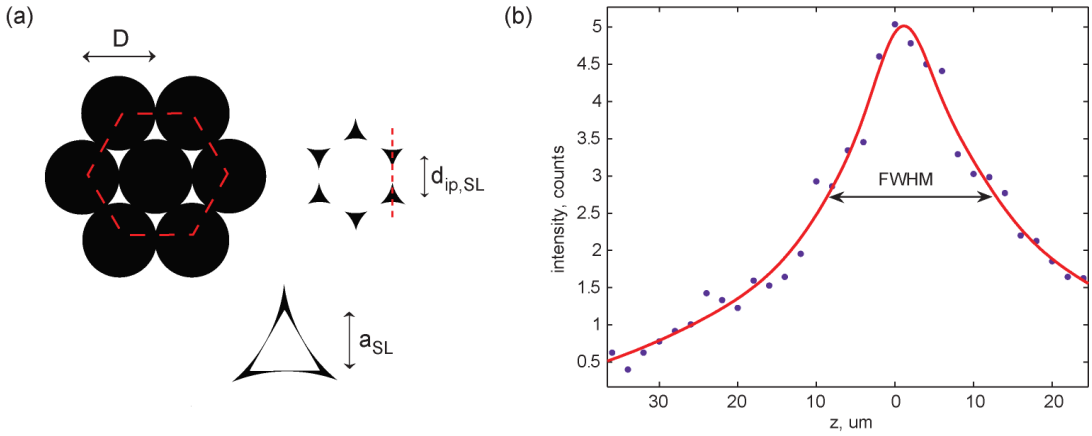

Figure 7.8: Parameters used in the calculation of *EF* (a) Geometry and corresponding parameters of the NSL substrates used to calculate μ_M, A_M and μ_S (b) Intensity-distance profile of the laser moving through a silicon wafer indicating the FWHM, used to measure H_{eff}.

This gives an enhancement factor of about 1.8×10^5 for both SERS substrates with the 384nm substrate having a slightly higher value than the 1002nm substrate, which is in reasonable agreement with similar substrates [113]. In general, conventional SERS is considered to be capable of an enhancement on the order of 10^5-10^6 [162].

7.3.4 Finite element analysis

The distribution and magnitude of enhancement across the SERS substrates was modelled and further analysed with FEM. FEM is a numerical technique for finding approximate solutions of partial differential equations by dividing a geometric model into domains and smaller elements. It is used for countless applications in a range of subject areas from chemical engineering to plasma physics, structural mechanics to electromagnetics. The interaction of the laser with the NSL SERS substrates was simulated in COMSOL Multiphysics (COMSOL, UK), FEM software in which a geometry is defined, meshed and solved for a specific set of physical parameters and concepts.

To model these substrates, 2D sections (indicated in Figure 7.8a) through a three-dimensional (3D) array of silver truncated tetrahedrons on a glass support in air were constructed in a frequency-domain study. The substrate was positioned parallel to the xz-plane while the silver nanostructures were placed along the y-axis. A transverse electromagnetic wave propagating along the y-axis was considered with

incident electric and magnetic fields in the x and z directions respectively, expressed as

$$E_{inc,x} = E_0 e^{-i\frac{2\pi}{\lambda}y}\hat{x} \qquad H_{inc,z} = H_0 e^{-i\frac{2\pi}{\lambda}y}\hat{z} \tag{7.6}$$

where E_0 and H_0 are the incident electric and magnetic field amplitudes respectively and λ is the wavelength of the incident light. The total electromagnetic fields $E = E_{inc} + E_{scattered}$ and $H = H_{inc} + H_{scattered}$ should satisfy Maxwell's equations within the medium, substrate and nanostructure domains.

$$\begin{aligned} \nabla \times (\nabla \times \boldsymbol{E}) - \omega^2 \varepsilon \mu E = 0 \\ \nabla \times (\nabla \times \boldsymbol{H}) - \omega^2 \varepsilon \mu H = 0 \end{aligned} \tag{7.7}$$

where ε and μ are domain-dependent permittivity and permeability, $\omega = 2\pi/\lambda$ is the frequency of the incident light, $\boldsymbol{E} = (E_x, E_y, 0)$ and $\boldsymbol{H} = (0, 0, H_z)$. Each domain was given the appropriate material properties, including optical constants for air, glass and silver corresponding to the appropriate wavelength of incident light [163]. To numerically solve Maxwell's equations, various boundary conditions were applied to define the physics of each domain. Scattering boundary conditions were applied at the edge of the system and the silver nanostructures were defined as perfect electric conductors. Continuity of tangential components of $\boldsymbol{E}$ and $\boldsymbol{H}$ across the interface between domains leads to the following boundary conditions,

$$\begin{aligned} (\boldsymbol{E}_1 - \boldsymbol{E}_2) \times \boldsymbol{n} = 0 \\ (\boldsymbol{H}_1 - \boldsymbol{H}_2) \times \boldsymbol{n} = 0 \end{aligned} \tag{7.8}$$

where $\boldsymbol{n}$ is the interfacial normal vector. Numerical solutions of these equations were obtained for each material; Equations 7.7 were solved for each domain whilst Equations 7.8 were held for all internal interfaces. Perfectly matched layers (PML) were also employed in the model [164]. PML are artificial absorbing layers used in FEM to simulate open boundaries. They do this by attenuating propagating waves to prevent their reflection back into the model, applying the low-reflection boundary condition

$$\boldsymbol{n} \times \left(\nabla \times \boldsymbol{H}_z \right) - i\omega H_z = 0 \tag{7.9}$$

After applying boundary conditions, each domain in the model is meshed into smaller elements (Figure 7.9). The size of the mesh was selected according to the relevance of each area of the model to the overall system. For instance, a higher density mesh was chosen for the surface of the nanostructures. The number of elements within each mesh was chosen as a compromise between accuracy and computation time. Maxwell's equations are then solved for each of these elements. This results in a visualisation of the 2D electric field distribution across the system (Figure 7.10).

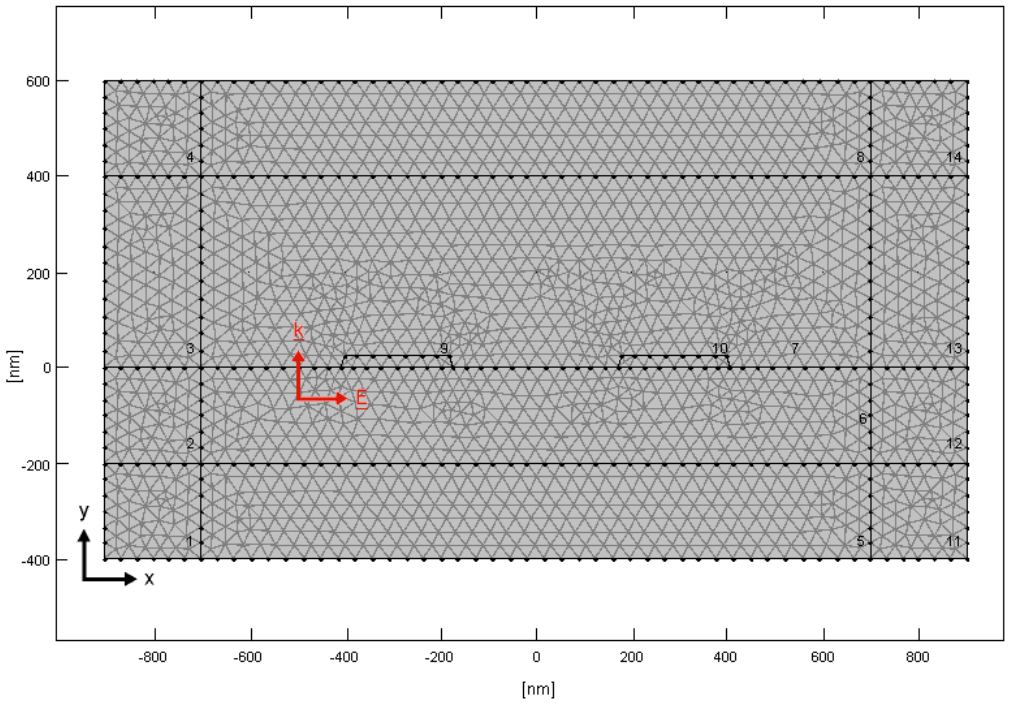

Figure 7.9: FEM model meshed and ready to be solved, with defined domains, boundary conditions and PML.

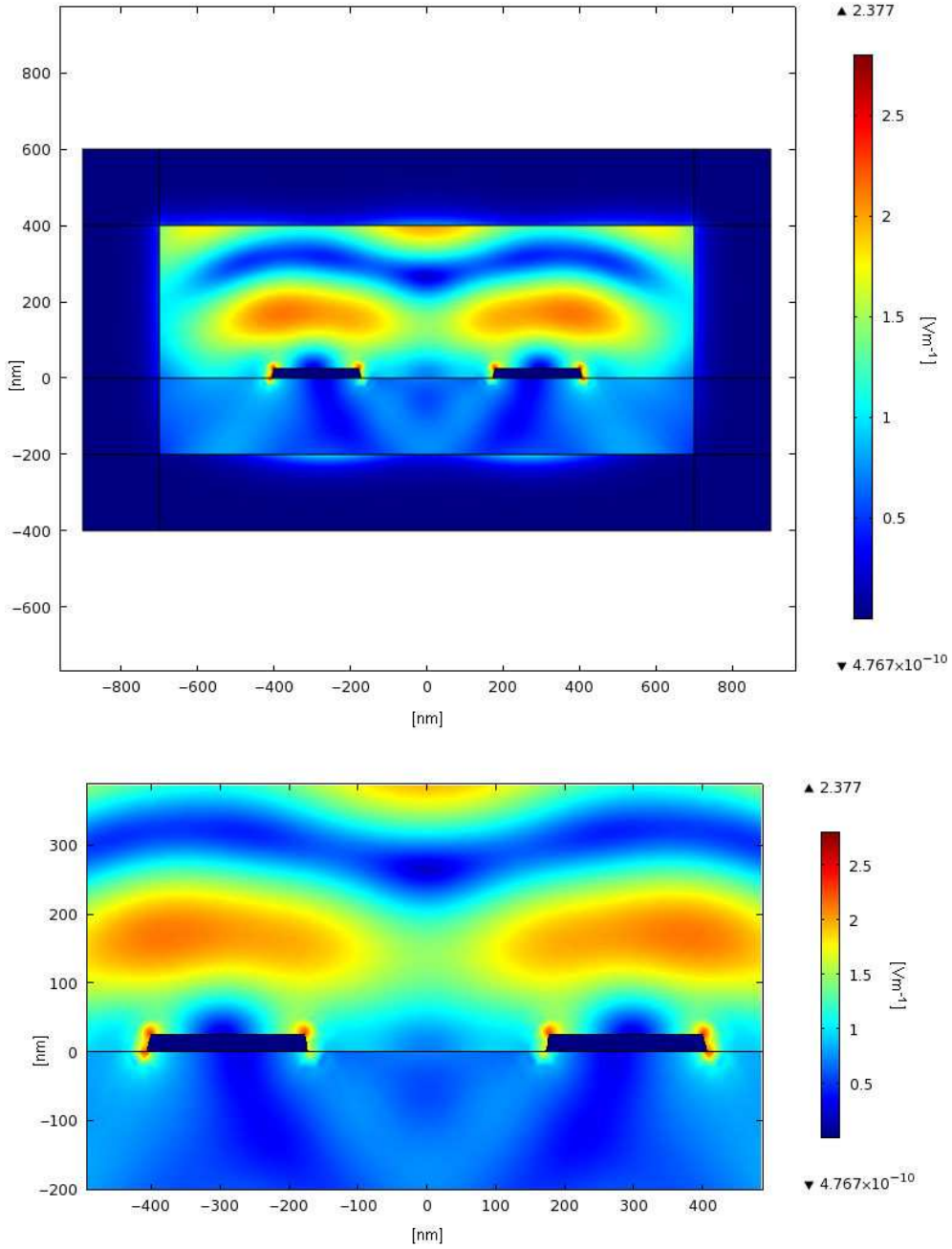

Figure 7.10: Solution of FEM model for 1002nm SERS substrates, displaying the resultant electric field (Vm^{-1}). The top image is of the entire model, demonstrating the function of PML.

These FEM simulations support the experimental SERS mappings. They both demonstrate that the SERS effect occurs on the metallic surfaces themselves rather than the gaps between them. The model also indicates that the greatest enhancement of electric field occurs at the vertices of the nanostructures, which is in agreement with reported theoretical studies of these substrates [165, 166]. The magnitude of electric field in these models can be used to calculate the SERS enhancement factor,

$$EF = \log\left(\left|\frac{E(x,y)}{E_0}\right|^4\right) \tag{7.10}$$

where *E(x,y)* is the electric field amplitude at location (x,y). Using the model above, this gives an enhancement factor of 1.35×10^4 for the 1002nm substrates and 1.55×10^4 for the 384nm substrates. These values are slightly lower than those calculated from experimental data. This is expected, since the model does not consider the 3D nature of the real substrates or the chemical enhancement mechanism. Chemical enhancement arises from charge transfer between the material of interest and the metallic surface and only contributes around an order or two of magnitude to the overall SERS effect [126].

7.4 SERS imaging of a lipid bilayer

7.4.1 Phospholipids vs. fatty acids

Commonly, SLBs consist of phospholipids. These naturally occurring lipids are a major component of cell membranes, therefore they provide a biologically relevant model. However, a phospholipid SLB is a difficult structure to prepare and study, since it is unstable on storage in ambient conditions. In addition, many surfaces are incompatible with supporting a phospholipid bilayer. One step that can be taken before attempting to detect an SLB and image its microdomains with SERS is to investigate a simpler but similar model. A suitable alternative is a fatty acid bilayer. Fatty acids are a type of lipid that has many similarities to phospholipids, including dimensions, structure and composition. They also readily form a bilayer when exposed to water and have very weak Raman scattering. On the other hand, they are much easier to prepare, store and study than phospholipids.

Therefore, as a demonstration of the capability of the SERS substrates to provide sufficient and uniform enhancement for imaging SLBs, lipid bilayers of arachidic acid (AA) were investigated on the SERS substrates. AA is a saturated fatty acid molecule with lipid number C20:0 (Sigma Aldrich, UK). It is a well known amphiphile that is often used for Langmuir-Blodgett (LB) studies, as it can easily form monolayers on a water surface and be transferred with unit transfer ratio to

create single or multiple layer films. Consequently, AA is often used as a matrix for studying other molecules in a monolayer or bilayer with SERS. The hydrocarbon chain in AA is chemically inert and a very poor Raman scatterer below about 2800cm^{-1} (C–H stretching), providing a convenient spectral window in the fingerprint region. However, this also means that AA itself is difficult to detect without good enhancement of signal and is rarely studied.

AA bilayers were formed using an LB trough (Nima Technology). 50µl of a 1mg/ml solution of AA in chloroform was deposited onto a subphase of water and compressed at a rate of 100cm^2/min to form a monolayer (Figure 7.11). The SERS substrates were then dipped through this monolayer to form a supported bilayer.

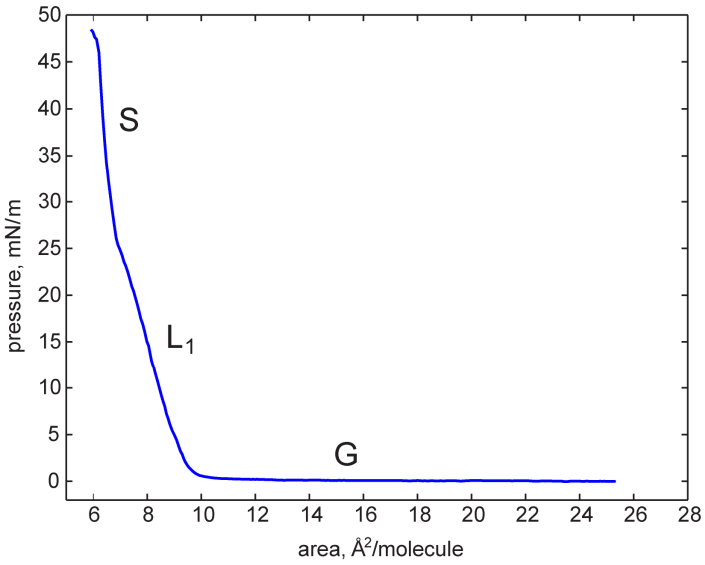

Figure 7.11: Surface pressure-area isotherm from the compression of a monolayer of AA on water (three distinct regions of gaseous (G), liquid (L_1) and solid (S) phase are indicated).

7.4.2 Comparison of Raman and SERS vibrations of AA

The assignment of Raman bands of lipids and fatty acids is well established [32, 167]; however, those relating to the SERS spectra of these molecules are not as well known. This is particularly the case for AA, for the aforementioned reasons. Often the Raman and SERS spectra of a molecule vary [101], due to the variation in Raman spectroscopy selection rules that arises from the SERS effect [102]. SERS spectra often contain peaks that are slightly shifted in frequency from those in the Raman

spectra, or even absent. Alternatively, SERS spectra can contain additional Raman bands. In most cases, different bands exhibit different levels of enhancement. Therefore before recording any mappings, the Raman spectrum of powdered AA and the SERS spectrum of an AA bilayer were compared (Figure 7.12). Vibrational modes at 1064, 1106 and 1131cm^{-1} in the Raman spectrum of AA can be assigned to C–C *trans* stretching, and relate to SERS peaks at 1063, 1103 and 1125cm^{-1}. The Raman band at 1296cm^{-1}, occurring at 1292cm^{-1} in the SERS spectrum, denotes CH_2 twisting deformations. Peaks in the Raman spectrum at 1418, 1441 and 1465cm^{-1} correspond to CH_2 scissoring and symmetric bending of the C–H bonds in the ester methyl group, and similarly the SERS vibration at 1394cm^{-1}. An additional peak is present in the SERS spectrum of AA at 924cm^{-1}; vibrational modes in the region of this peak can be assigned to acyl or C–C stretching, involving both the C–C and C–O bonds adjacent to the carbonyl group or the methyl terminal C–C bond.

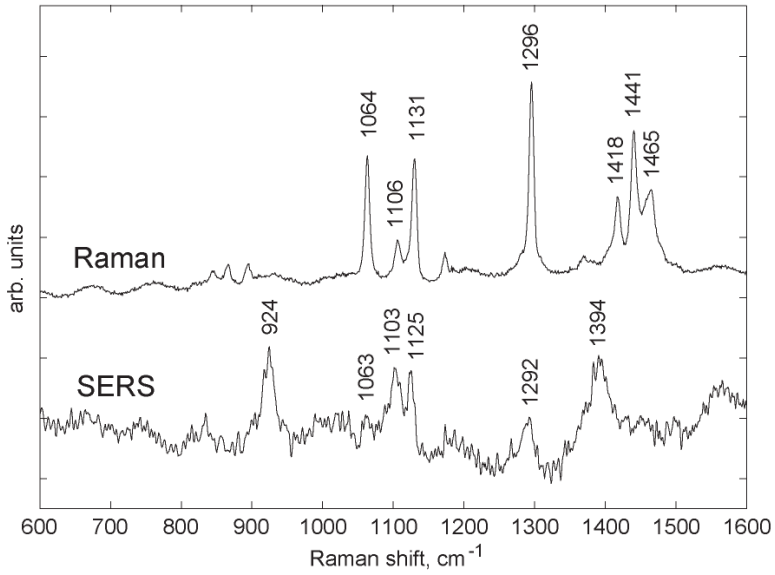

Figure 7.12: Comparison of unenhanced Raman and SERS spectra of AA, with the positions of significant Raman bands labelled.

7.4.3 SERS spectra and mapping of AA

In the same way as the mappings of R6G and p-ATP, the prepared substrates were firstly imaged with the AFM and a small area of was selected. The sample was then raster scanned through the laser focus whilst collecting the SERS spectrum at each point to generate a mapping from peak intensities. Finally, the mapping and AFM

image were compared to correlate chemical and physical information. Again, there was no background signal from the substrate itself to be subtracted from the spectra.

SERS substrates formed from both 384nm and 1002nm polystyrene spheres were mapped with bilayers of AA (Figure 7.13). The Raman band at 1394cm^{-1} ($-CH_2$ deformations) was used to create the mappings. Raman spectra with good signal-to-noise ratio were recorded for the lipid bilayer with a laser power of just 20μW and exposure time of 5s. As before, the distribution of SERS nanostructures and enhancement is apparent from the mappings of the 1002nm substrates. Comparing to AFM images taken of the mapping areas, the highest signal detected relates to the location of the silver nanostructures and less SERS scattering is collected from around these surfaces. SERS "hot-spots" were also detected at some of these points. Most notably, these results highlight that signal is detected from the entire substrate. This suggests that the substrate is completely covered by the bilayer and that its roughness is compatible with supporting an SLB [168]. Inversely, the mappings of the 384nm substrates appear to provide a uniform distribution of SERS signal, since the structure of the substrates is below the spatial resolution of the Raman spectroscopy system and consequently undetectable. Therefore, it is possible to image a single lipid bilayer both chemically and physically with NSL SERS substrates, particularly with the 384nm substrates for which there is little variation in enhancement detected across the substrate.

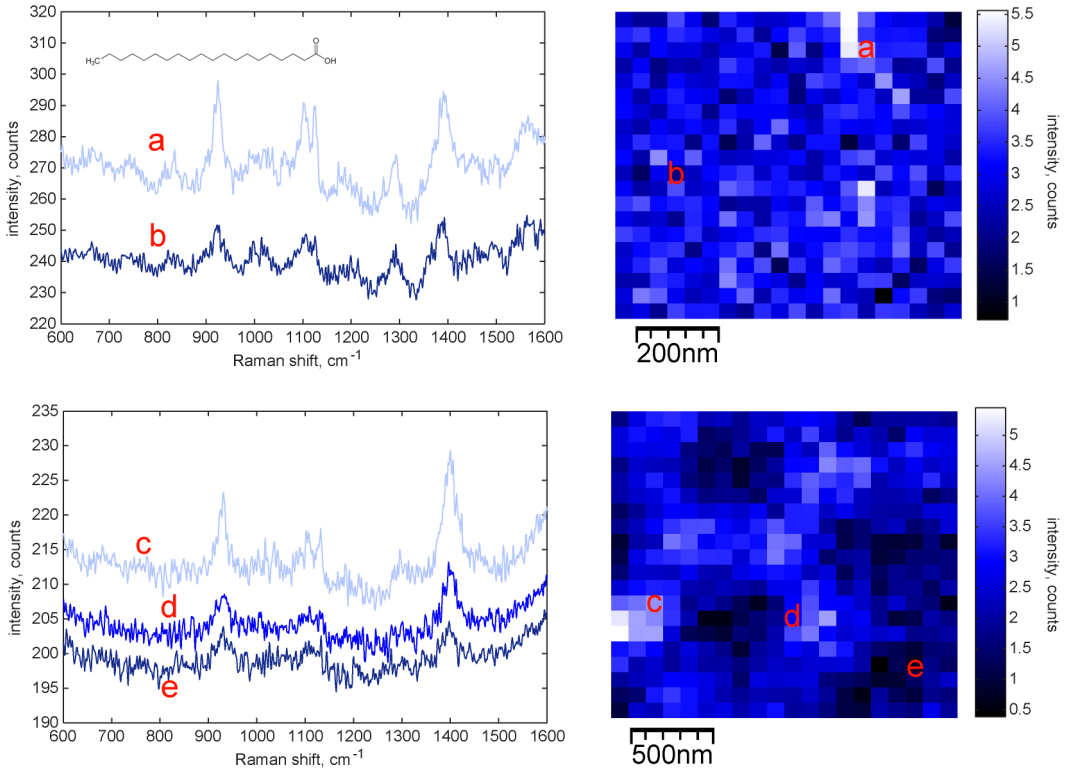

Figure 7.13: SERS spectra and mappings of AA on 384nm (top) and 1002nm (bottom) substrates. Labelled spectra correspond to the scattering measured at the position of the same labelling in the mappings.

7.5 Progress towards SERS imaging of phospholipid SLBs

The results from the SERS mapping of an AA bilayer demonstrate the potential of NSL substrates for imaging an SLB, in terms of providing a sufficient and uniform enhancement of its Raman signal. However, the substrates are constructed on glass, which does not allow imaging of microdomains by AFM. A common substrate for SLBs is mica, as it can be cleaved to provide an atomically flat surface. However, it is for these reasons that it is not possible to make the SERS substrates on mica, as the material breaks up on removal of the polystyrene spheres at the end of the NSL process. Mica also has distinguishable Raman scattering. As demonstrated in the previous chapter, a number of other substrates are not compatible with potentially supporting an SLB. The exception is sapphire. This material was identified as a suitable substrate for SLBs as it can be treated with heat and acids to create an extremely flat and clean surface. It also has minimal Raman scattering. Therefore sapphire provides the best chance of imaging SLBs with SERS.

A critical step in this work is to support an SLB on a sapphire-based SERS substrate and progress has been made towards achieving this. As described in the previous chapter, a dipalmitoylphosphatidylcholine (DPPC) bilayer was successfully formed on sapphire. Furthermore, the SERS substrates have been produced on sapphire. They were prepared in the same way as the original glass substrates with the addition of annealing the sapphire at 1100°C for 2hrs at the beginning of the process. This resulted in NSL substrates on sapphire suitable for imaging SLBs with SERS. Finally, these two developments were combined to support an SLB on a SERS substrate made of sapphire, confirmed by the presence of 4.1nm defects, or holes, in the SLB when imaged with AFM (Figure 7.14).

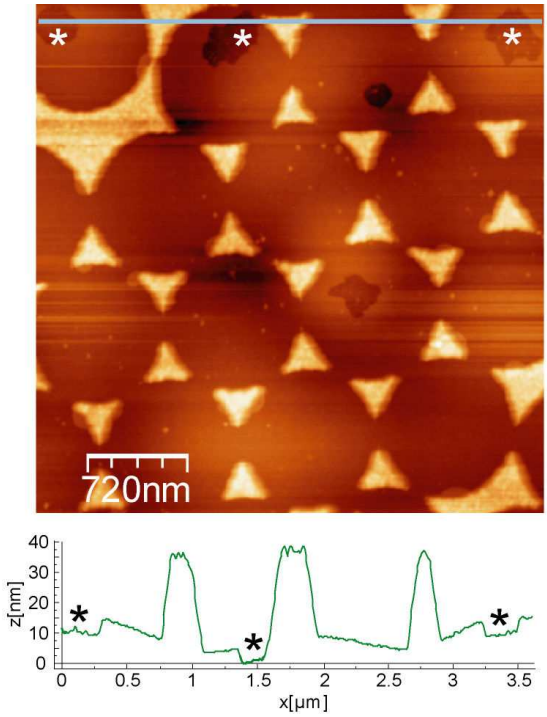

Figure 7.14: AFM image and line profile of a DPPC SLB on a sapphire-based SERS substrate (holes in SLB are indicated by *).

The main challenge in imaging SLBs with SERS is obtaining sufficient enhancement to detect these nanoscale structures with the experimental setup. The ability to produce a chemical mapping of a bilayer of AA with good signal-to-noise ratio spectra suggests that this is achievable; however, further work is needed here.

7.6 Conclusions

In this chapter, NSL substrates have been investigated in terms of their suitability for SERS imaging of SLBs. These substrates were assessed for the distribution and magnitude of enhancement of Raman signal that they could provide, since high, uniform enhancement is important for detecting the weak scattering from SLBs and the variation in chemical composition of an SLB containing microdomains. The combined AFM-Raman system allowed direct correlation of physical and chemical information about these substrates and several samples deposited on them. SERS spectra and mappings of R6G and p-ATP monolayers revealed the structure and variation in enhancement of the 1002nm substrates, indicating that the highest signal occurs on the silver nanostructures themselves. Uniform enhancement was detected in similar mappings of the 384nm substrates, for which the nanostructures are below the diffraction limit of the system. An enhancement factor common for this type of SERS substrate was calculated and FEM models were constructed to support this and the experiments.

Finally, the substrates were used for measuring SERS mappings of AA lipid bilayers. Comparison between the Raman and SERS spectra of AA enabled assignment of its SERS bands. The SERS mappings demonstrated a uniform distribution of enhancement across the 384nm substrates whilst leaving the bilayer undisturbed, making them suitable for label-free imaging of lipid microdomains. Considering the close similarities between fatty acid molecules and membrane lipids such as phospholipids, this study demonstrates the potential of combined AFM and SERS with NSL substrates for detecting SLBs and imaging the phase-separated microdomains they form.

Chapter 8

Tip-enhanced Raman spectroscopy

This chapter describes the development of functionalised probes for TERS. The phenomenon DEP is generated within a conductive AFM setup to grow clusters of gold nanoparticles at the tip apex of AFM probes. This growth is monitored with force spectroscopy, topographical imaging and related parameters and then analysed further with SEM and EDX. Finally, the TERS activity of these probes is explored with chemical mappings performed on the combined AFM-Raman system.

8.1 Introduction

Tip-enhanced Raman spectroscopy (TERS) is one of the most recent advances in nanoscale chemical analysis [69, 128]. This relatively new Raman spectroscopy technique is based on the same mechanism as the surface-enhanced Raman spectroscopy (SERS) effect; local electric fields are strongly enhanced in the vicinity of a metallic surface due to the coupling of its plasmon resonances with the excitation light. In TERS this metallic surface takes the form of a sharp metal tip, usually an atomic force microscopy (AFM) or scanning tunnelling microscopy (STM) probe coated in silver or gold. The technique has great potential for imaging biological materials such as supported lipid bilayers (SLBs) [71]. The main reason for this is that TERS requires no special sample preparation, meaning the sample can be measured *in situ*. This is one advantage the technique has over SERS, in which consideration must be given to the compatibility of the sample and metallic surface

as the sample is often deposited onto it. TERS can achieve excellent spatial resolution, which in principle is only limited by the size and shape of the scanning probe microscopy (SPM) probe tip apex. The setup of TERS also ensures there is no variation of enhancement across a sample and automatically allows correlation of surface topography with chemical information.

As is the case with SERS, the development of the metallic surface that provides the enhancement of Raman scattering is essential to the success of TERS and must be optimised to realise the full potential of the technique. Commonly, there are two approaches to producing TERS-active probes; either creation of an SPM tip by electrochemical etching of a thin wire or modification of an existing SPM probe by metal evaporation or nanostructuring. However, the fabrication of TERS probes is not straightforward and is yet to be established [169]. The work described in this chapter presents a novel method for functionalising AFM probes to produce a metal-coated tip capable of activating TERS. A phenomenon known as dielectrophoresis (DEP) has been employed to accumulate clusters of nanoparticles from a suspension at the tip apex of an AFM probe. This growth is developed within a conductive AFM setup and monitored by force spectroscopy, topographical imaging and a variety of AFM parameters. The technique was investigated for its potential to create reproducible, suitably optically-active probes by scanning electron microscopy (SEM) imaging and related chemical analysis. This potential was then further explored using the combined AFM and Raman spectroscopy system, an ideal experimental setup for performing TERS.

8.2 Dielectrophoresis

There are generally two approaches to the movement and organisation of nanoparticles to create functional nanoscale systems; direct assembly of individual elements by controlled manipulation [170] and self-assembly of elements without guidance or management from an outside source [171]. However, DEP is one method that sits between these two extremes, using electric field gradients to guide nanoparticulate growth.

This phenomenon was first studied in detail in the 1950s by physical chemist Herbert Pohl [172]. For centuries before there had been scientific interest in the manipulation of matter using electric fields, including the more specific effects of inhomogeneous electric fields on neutral matter that DEP is based on. However, it was not until the pioneering work of Pohl that these effects were fully explored or defined. He combined theoretical calculations and experimental observations to describe the induced motion of suspended dielectric particles by forces in a non-uniform electric field. Since this original study, work in the field has steadily progressed until recently when its application to nanoscience boosted interest. DEP has now been applied to a broad range of research areas, from the separation and sorting of biological substances [173, 174] to the assembly of micro and nanoscale devices [175-177]. This is possible due to the ability of the technique to manipulate particles with great selectivity. The strength of the force from which the effect arises can be finely tuned, since it depends on the medium, the shape, size and electrical properties of the particles and the frequency of the electric field. In addition, DEP does not require the particle to be charged, which is a major advantage it has over similar phenomena such as electrophoresis.

To avoid confusion with similar and related phenomena, the characteristics of DEP were later defined by Pohl (Figure 8.1) [178]. These can be summarised as:

(1) Particles only experience DEP when the electric field is non-uniform.
(2) The DEP force does not depend on the polarity of the electric field, so it can be observed with AC or DC excitation.
(3) Particles are attracted to regions of stronger electric field when their permittivity exceeds that of the suspension medium.
(4) When the permittivity of the medium is greater than that of the particles, they are repelled from regions of stronger electric field.
(5) The DEP force acts on uncharged particles that can be polarised.

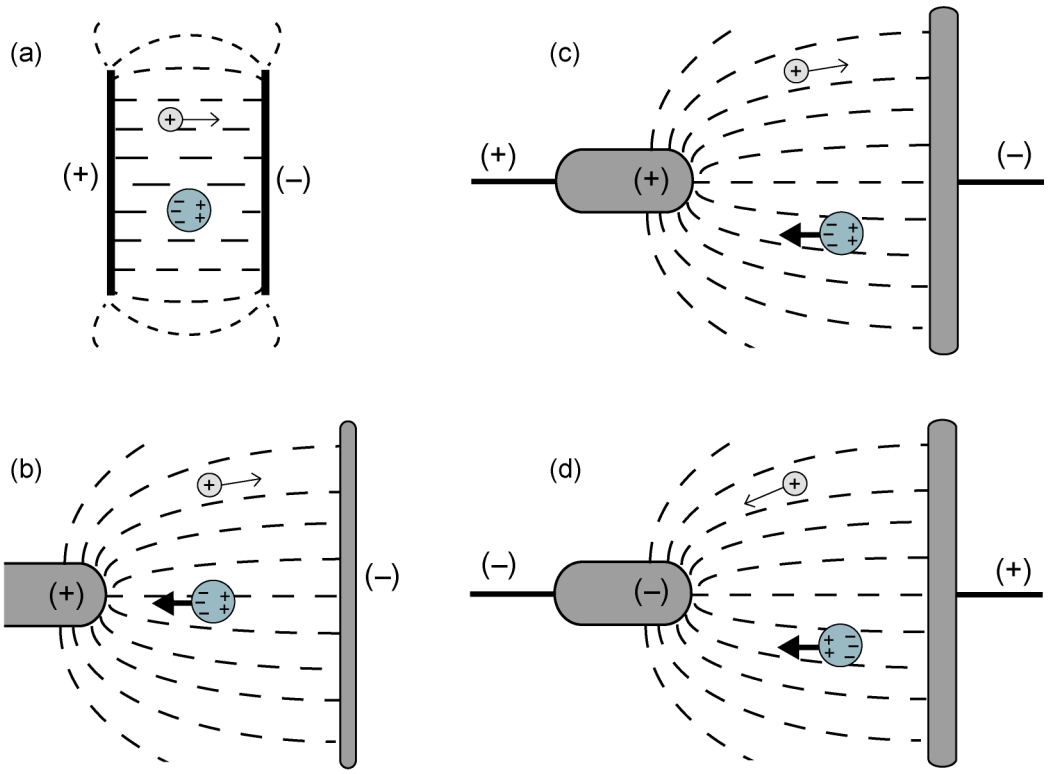

Figure 8.1: Comparison of the behaviour of neutral and charged particles in (a) a uniform and (b) non-uniform electric field (c-d) an alternating non-uniform electric field.

The DEP force arises from the effect an inhomogeneous electric field has on the dipole moment of a neutrally-charged particle. In any electric field, uncharged particles are polarised and a dipole is induced across each of them that is aligned parallel to the field [179]. However, it is only in a non-uniform field that these particles will move, as they are pulled along the gradient of the electric field towards regions of stronger electric field. This is a result of the DEP force, which is given by

$$F_{DEP} = 2\pi r^3 \varepsilon_m \left(\frac{\varepsilon_p - \varepsilon_m}{\varepsilon_p + 2\varepsilon_m} \right) \nabla E^2 \tag{8.1}$$

where r is the particle radius, ε_m is the permittivity of the suspension medium, ε_p is the permittivity of the particle and ∇E is the gradient of the electric field. One key feature of this expression is the factor in brackets, which is known as the Clausius-Mossotti function [179, 180]. This factor contains all the frequency dependence of the DEP force. The force is proportional to the magnitude of this factor and directionally dependant on its sign. The expression above also highlights that the

behaviour of the DEP force is proportional to both the volume of the particle and the dielectric permittivity of the suspension medium. Most notably, it indicates the direct dependence of the DEP force on field gradient, which is an interesting result for practical applications of the effect. The geometry of an experimental setup of DEP has been previously considered [181], to determine the scaling law

$$\nabla E^2 = \frac{V^2}{L^3} \tag{8.2}$$

where V is the applied potential across a pair of electrodes and L is the characteristic length scale of the system. From this law, it can be seen that an increase in DEP force can arise from an increase in the applied voltage or a reduction in the size of the system. Therefore it is possible to achieve DEP with voltages much less than those of the original experiments by Pohl.

8.3 Development of nanostructured probes for TERS

8.3.1 Generating DEP within an AFM setup

Conductive AFM has been employed to develop nanostructured TERS-active probes with DEP. Conductive AFM is an application of AFM that is commonly used for electrical characterisation of samples by simultaneously measuring their topography and current or charge distribution. However, the technique can easily be adapted to provide a variety of purposes. It requires a conductive AFM probe combined with a specially-designed cantilever holder that includes a transimpedance amplifier with a feedback resistor.

A typical conductive AFM setup was used to functionalise iridium-coated conductive silicon probes with a resonant frequency of 45-95kHz, spring constant of 0.5-4.4N/m and manufactured tip radius of 23±10nm (MFP-3D, Asylum Research) (Figure 8.2). The surface for experiments was a 1cm^2 piece of graphite that was freshly cleaved and placed into a sample mount with electrical contacts. The AFM probe was loaded into a holder containing an in-built transimpedance amplifier of 20nA/V gain with a 50MΩ feedback resistor, which can measure the current at the probe-sample junction

by biasing the sample with a suitable potential. This holder was connected to the graphite and sample mount to form a circuit. After tuning the cantilever and approaching the surface, the tip was calibrated for force and electrical measurements. A small o-ring was placed in the middle of the graphite and filled with a suspension of 10nm diameter thiol-passivated gold nanoparticles in water, forming a meniscus. The cantilever holder, sample mount and graphite were then connected to a frequency generator and oscilloscope. The AFM cantilever was re-tuned in the nanoparticle suspension and approached. After scanning the graphite, the tip was disengaged. Manual positioning of the tip was achieved by accessing low level functionality of the AFM; this was necessary to gradually raise the tip whilst monitoring the change in the deflection of the cantilever. The vertical position of the tip was set to the point just before the deflection started to increase and the tip was about 50-100nm above the surface of the graphite. The frequency generator was then set to the desired frequency and voltage, which was applied over a certain time period to establish DEP between the graphite surface and the tip apex of the AFM probe. Finally, the probe was recalibrated, force curves were repeated and the graphite was scanned again to detect any changes in the surface or the tip of the AFM probe.

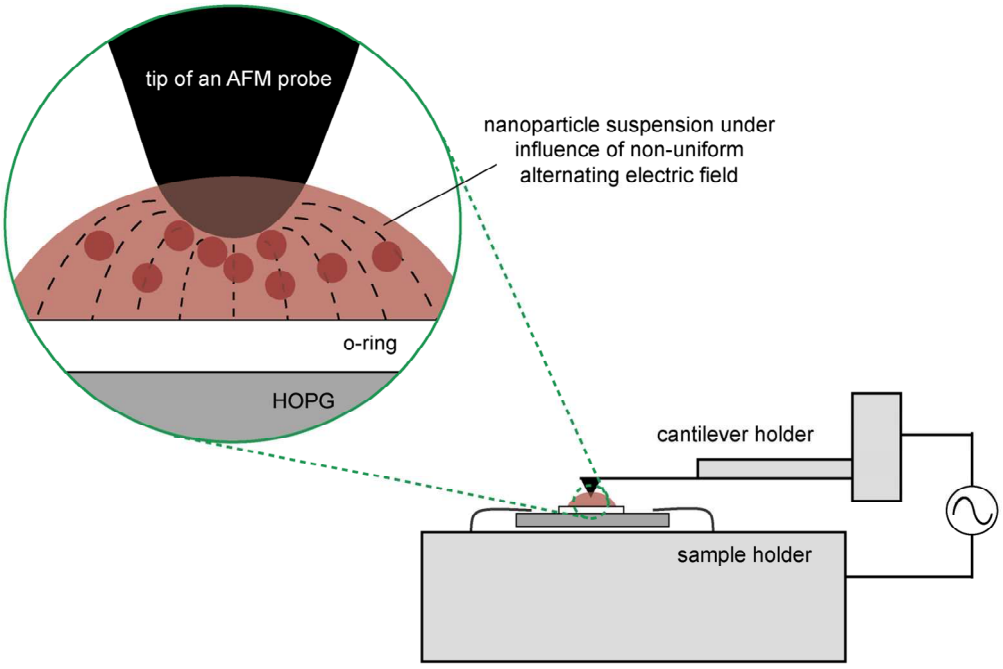

Figure 8.2: Schematic of the conductive AFM setup used to functionalise probes using DEP (detection and feedback mechanisms omitted from the diagram).

Initially, fairly high frequencies and voltages of around 15MHz and 20Vpp were applied to the system to gauge an idea of how large these values needed to be in order to generate an efficient DEP force. The difference in the shape and axes of force curves recorded before and after applying these voltages indicated that a large amount of material had been added to the tip of the AFM probe (Figure 8.3a). These force spectroscopy results were supported by a number of imaging parameters that were monitored over the course of these experiments. There was a large variation in the deflection of the cantilever and the vertical position of the tip, which suggested a reduction in the distance between the tip and the surface of the graphite. There was a significant increase of about 0.16N/m in the spring constant of the AFM cantilever, indicating that the probe had gained mass. It was also very difficult to image with the tip after applying the voltage, which suggested that the tip apex had been greatly modified. All these changes were seen to a lesser extent when lower frequencies and voltages of around 1MHz and 5Vpp were applied to the system (Figure 8.3b), suggesting less activity between the tip and the graphite surface and allowing for greater control and refinement of the technique.

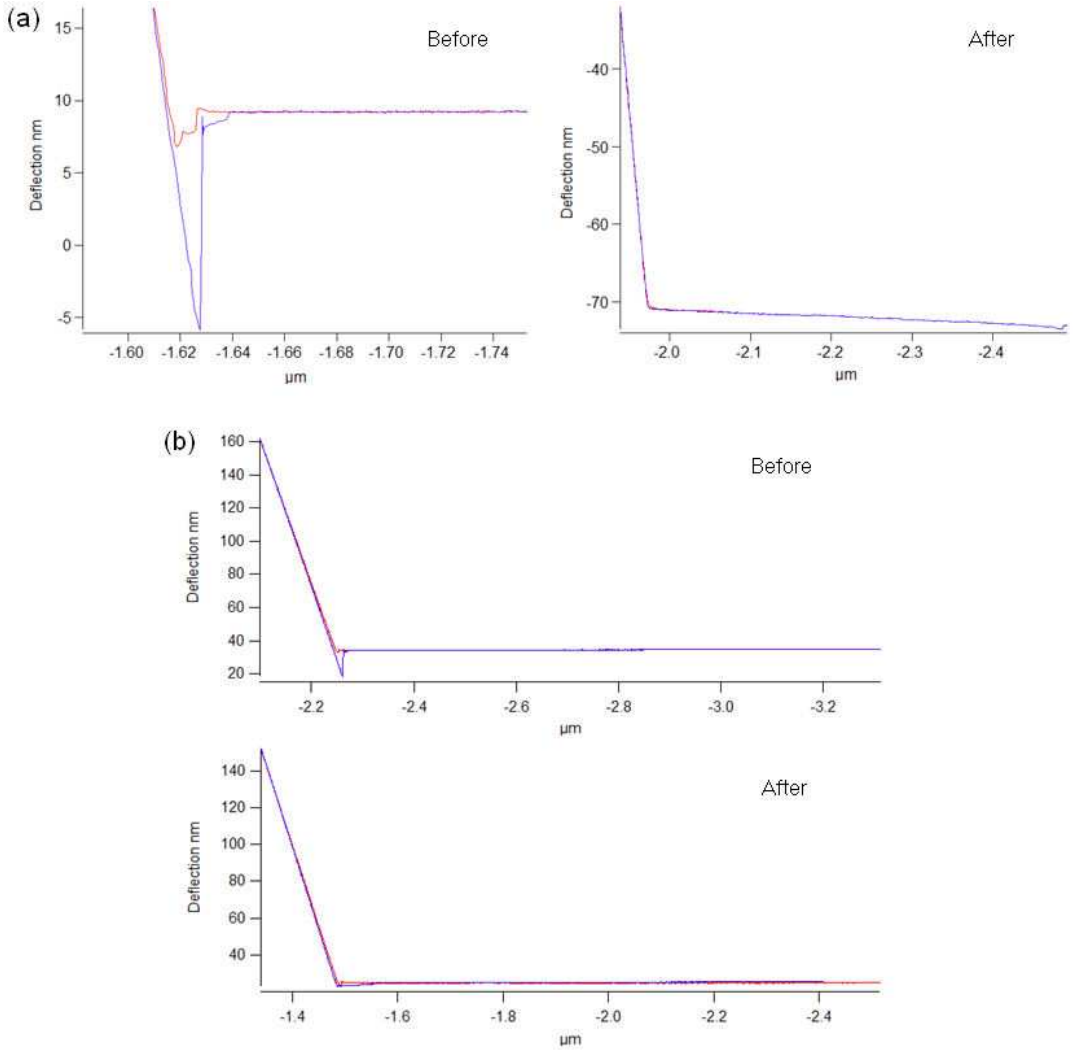

Figure 8.3: Force curves recorded before and after applying (a) high and (b) low frequency and voltage.

After these lower voltages were applied to the system, the tips were capable of scanning the surface of graphite and producing reasonable topographical images of it (Figure 8.4). There was an obvious deterioration in imaging quality before and after performing each experiment; however, the resolution was good enough to observe some interesting changes in the graphite surface. In general, material had accumulated and been added to the surface.

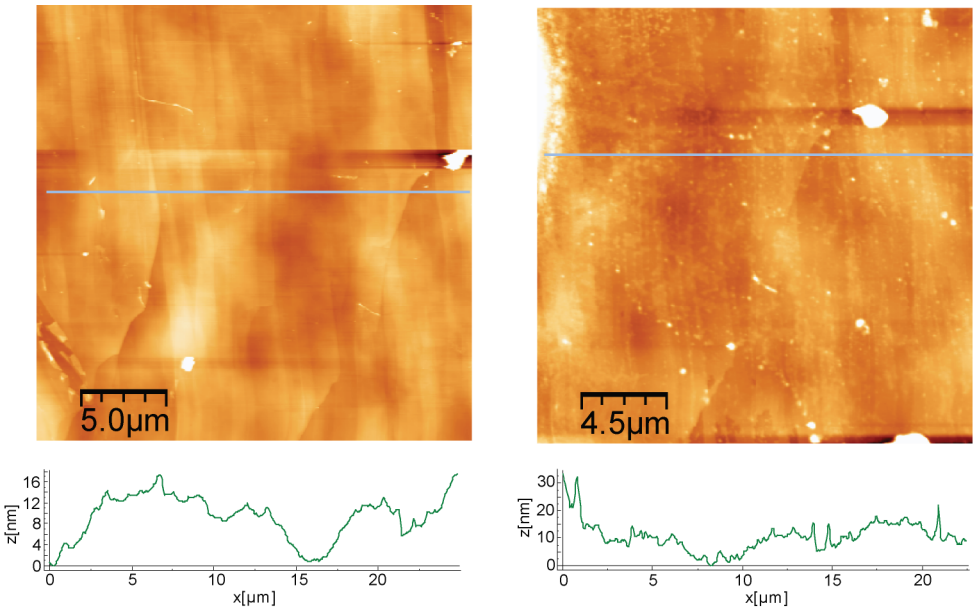

Figure 8.4: AFM images and height profiles of the topography of the graphite surface before and after applying a voltage to the system.

These images changed the focus of experiments towards depositing clusters of nanoparticles on the surface as an indication of growth on the probe. This was evidence of DEP being generated, as material was being trapped between the tip of the AFM probe and the graphite surface. The voltage and frequency being applied to the system was tuned to deposit a small amount of material on the surface at the exact position of the tip (Figure 8.5 and Figure 8.6). A frequency of 1MHz and a voltage of 10Vpp were found to produce suitable, reproducible results. In addition, the size of deposition was able to be controlled by varying the period of time over which the voltage was applied to the system, from around 30 to 120s. This growth on the graphite suggested that nanoparticles were collecting and aggregating between the tip apex and the surface and then breaking apart to form structures on each. This was the clearest indication from any AFM measurements that DEP was being established and reproducibly functionalising the probes inserted into the setup. However, direct analysis of the tips with other techniques was required for verification of this.

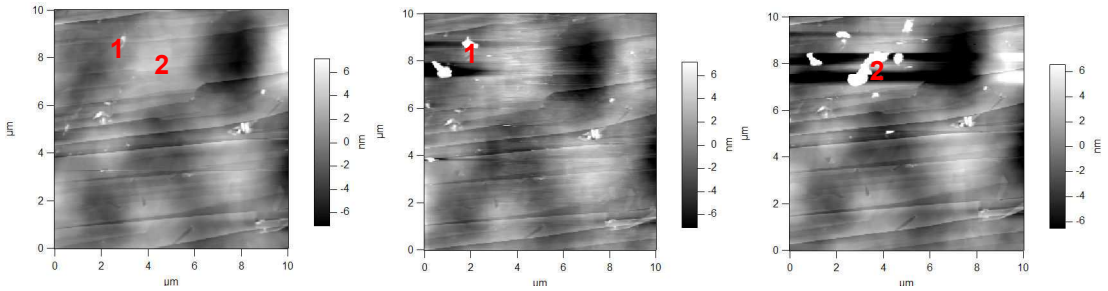

Figure 8.5: Successive AFM images show the growth of nanoparticle clusters after applying a voltage for 30s at position 1 and then again for 60s at position 2.

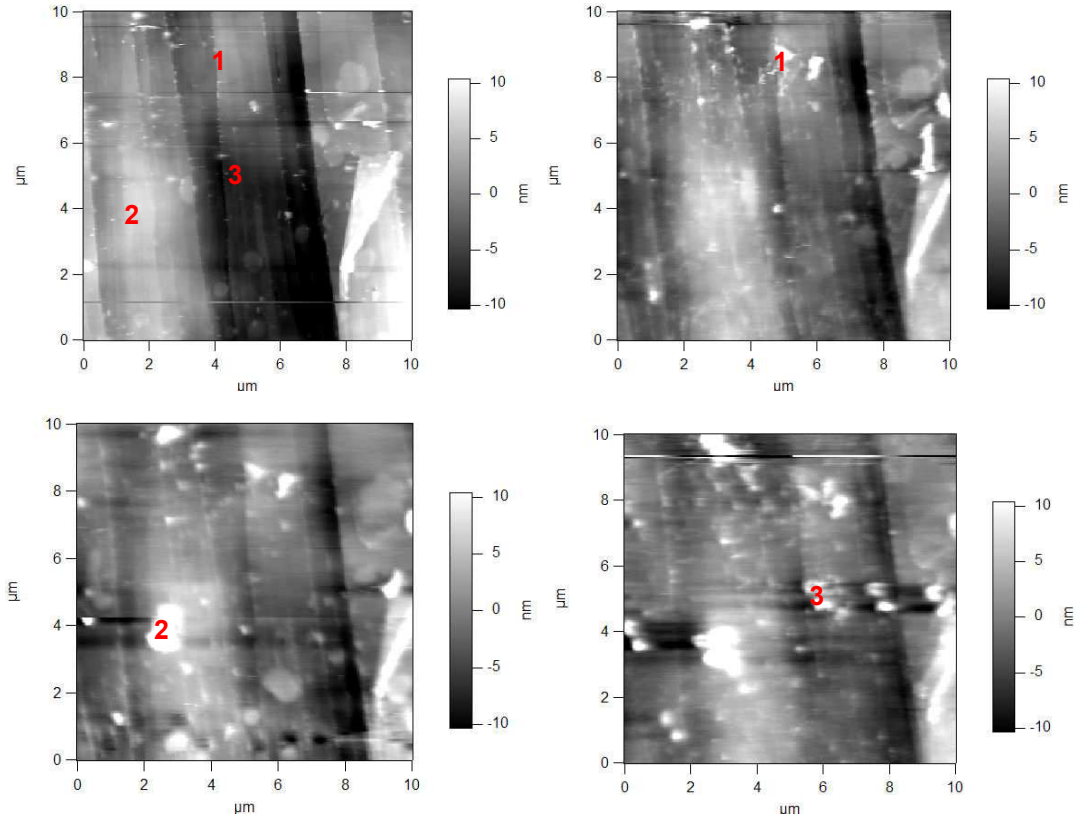

Figure 8.6: Successive AFM images show the growth of nanoparticle clusters after applying a voltage for 30s at position 1, for 60s at position 2 and then for 30s at position 3.

8.3.2 SEM imaging and chemical analysis

Alongside SPM, SEM is the most commonly used high-resolution surface analysis technique. It is predominantly used to image large objects with nanoscale features. In one pass it can image an area on the order of square millimetres with high resolution, high magnification and a depth of field on the order of millimetres. SEM uses a high-energy electron beam guided by a complex array of lenses to interact with a sample as it scans its surface. This produces a range of signals, including

secondary and back-scattered electrons that are used to build a three-dimensional (3D) topographical image of the sample. Another key outcome of the technique is characteristic x-rays, which are detected by an energy-dispersive x-ray spectroscopy (EDX) setup connected to the SEM. These are used to measure the abundance of elements in the sample and identify its chemical composition. The main disadvantage of SEM is that it requires special sample preparation. It is performed in vacuum and requires samples to fit in the specimen chamber, be mounted rigidly on a specimen holder and be electrically conductive. However, this is not a problem for dry, solid, metal objects such as AFM probes.

The AFM probes functionalised with DEP were analysed with SEM and EDX, which produced a variety of interesting results. Firstly, fractal-like structures were observed on many of the AFM probes (Figure 8.7). These structures are characteristic of diffusion-limited aggregation (DLA), a process whereby particles undergoing a random walk due to Brownian motion cluster together to form aggregates [182]. DLA is often observed with DEP [183]. Therefore, these structures provide evidence for some form of aggregation and growth of nanoparticles on the AFM probes as a result of the experimental setup.

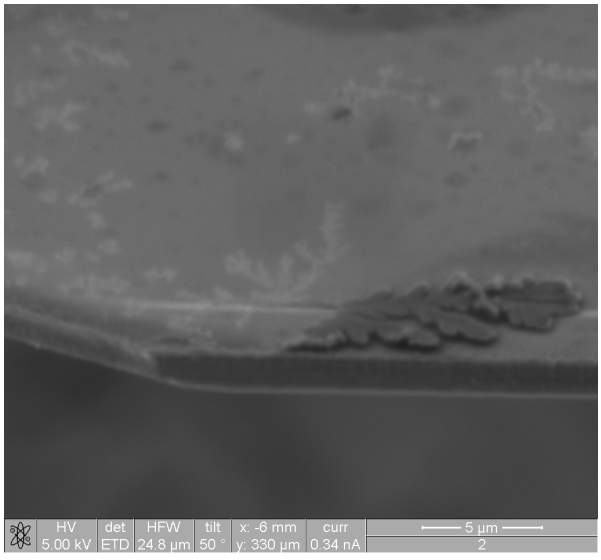

Figure 8.7: SEM image of fractal-like structures on a functionalised AFM probe (located on the side of the cantilever, near the tip).

A number of functionalised AFM probes exhibited wire-like structures growing out from the surface of the tip, which are typical of those produced by DEP (Figure 8.8).

The growth and manipulation of these structures is a relatively new development of DEP, first observed in 2001 [177, 184]. They consist of long, thin aggregations of metallic nanoparticles, often with a diameter of a few micrometres and a length on the order of millimetres. These structures were originally believed to be a result of fluid flow; however, subsequent work in the field focused on the DEP force being the dominant effect [185, 186]. Their growth rate, branching and thickness can be controlled by variations in the voltage and frequency applied, the nanoparticle concentration and size and the concentration of the suspension medium.

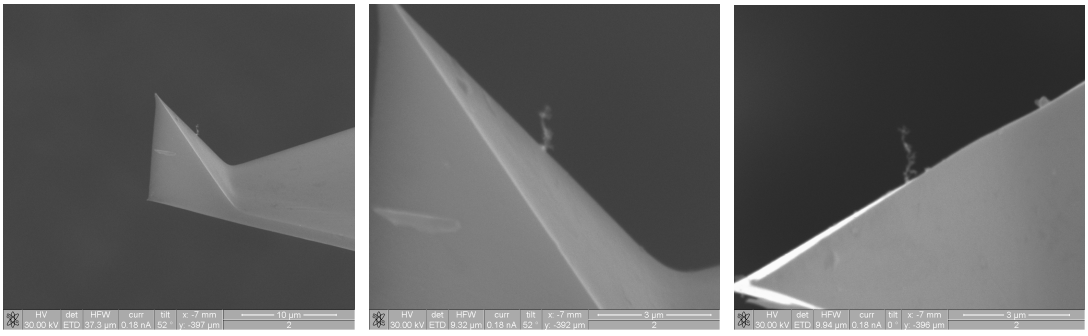

Figure 8.8: SEM images of the tip of a functionalised AFM probe, exhibiting typical DEP growth.

Finally, two of the AFM probes exposed to DEP had a significant clustering of nanoparticles at the tip apex. This was firstly observed in SEM images of the probes (Figure 8.9 inset). Then the chemical nature of this growth was analysed quantitatively with EDX; alongside the expected elemental composition of an AFM probe, spectral data revealed an abundance of gold within the region of the tip apex (Figure 8.9 spectrum and Table 8.1). This analysis confirmed that the growth consisted of nanoparticles, assembled from suspension at the tip apex of the AFM probe by DEP. It is the location of this growth that makes these probes suitable for TERS studies.

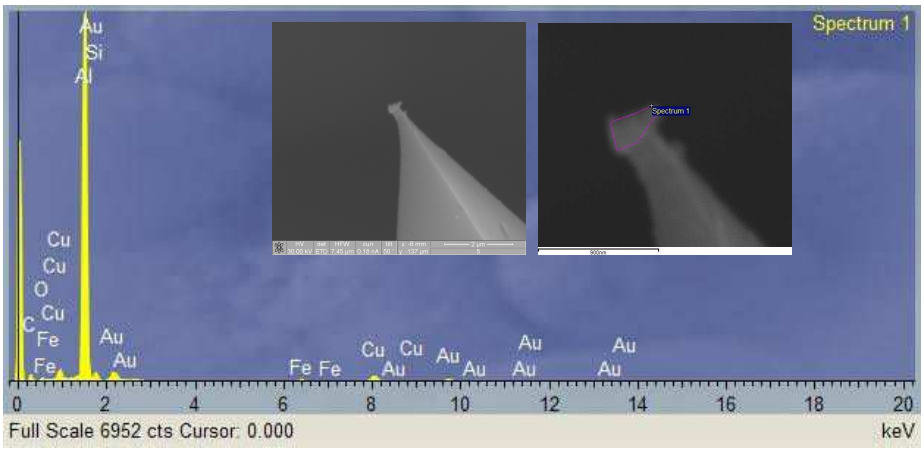

Figure 8.9: EDX spectrum of the tip apex of a functionalised AFM probe imaged with SEM (inset), containing many peaks corresponding to gold.

element	*app. conc.*	*intensity corrn.*	*weight %*	*weight % sigma*	*atomic %*
C K	4.73	0.2607	20.79	1.72	39.54
O K	1.95	0.6328	3.52	0.59	5.03
Al K	56.02	1.0740	59.73	1.44	50.58
Si K	1.17	0.5581	2.40	0.23	1.95
Fe K	0.53	0.9213	0.66	0.14	0.27
Cu K	3.64	0.8981	4.64	0.33	1.67
Au M	**4.63**	**0.6424**	**8.25**	**0.70**	**0.96**
totals			100.00		

Table 8.1: EDX data (figures for gold are highlighted in bold).

8.3.3 Performing TERS on combined AFM-Raman system

The TERS activity of the functionalised AFM probes was investigated by bringing the tip into contact with a monolayer of p-aminothiophenol (p-ATP) (Sigma Aldrich, UK) on a thin silver film and measuring its Raman scattering. As with the SERS mapping detailed in the previous chapter, p-ATP is an ideal molecule for reliably determining electric field enhancement as it contains a thiol group (–SH) that attaches to a metallic surface to form a single monolayer. Additionally, the Raman scattering of this structure is extremely weak, therefore any signal detected at low laser powers and short exposure times must arise from some form of enhancement of the scattering. However, this setup may benefit from gap-mode TERS [187].

The p-ATP monolayer was deposited onto glass coverslips coated in a thin film of silver. Firstly, the glass coverslips (VWR International) were cleaned with a variety of solvents and etched with a piranha solution of 3:1 sulphuric acid and hydrogen peroxide (H_2SO_4:H_2O_2) (Sigma Aldrich, UK) for hydrophilicity. Then a ~25nm thin film of silver was thermally evaporated in vacuum (Edwards) onto these coverslips at a pressure of 10^{-7}mbar and evaporation rate of 0.3-0.4nm/s. The coated coverslips were immersed in 10^{-4}M p-ATP methanol solution for 2hr and then rinsed in methanol to ensure one molecular layer was adsorbed. One of these coverslips was then placed into the combined AFM and Raman spectroscopy system along with the AFM probe to be investigated.

A 500nm^2 region of the coverslip was selected to record a chemical mapping. These mappings were performed to locate the position at which the tip apex of the AFM probe is aligned with the laser spot. This is essential to achieving efficient electric field enhancement and is the most challenging aspect of creating a successful TERS setup. Commonly, the probe is scanned across the laser beam whilst its back-scattered light is directed to the spectrometer charge-coupled device (CCD) or a photodetector to be monitored. For reproducibility, the system is often aligned automatically using a piezoelectric stage and feedback mechanism. However, this setup was not possible with the instrument at the time of these experiments. Instead, the tip apex of the AFM probe was roughly aligned with the position of the laser beam using the crosshair of the optical camera. The area around this point was selected to record a chemical mapping in the same way as in the previous chapter, except this time the AFM probe was moved in a raster pattern whilst the sample was kept stationary. Chemical mappings were constructed with a laser power of just 20μW and a step size of just 25nm, acquiring a Raman spectrum at each position at a rate of 5s per pixel. The area of the Raman band at 1088cm^{-1} (S–C stretching) in each spectrum was calculated after subtraction of a local linear baseline and used to build a spectral mapping one pixel at a time. If the AFM probe and laser spot were aligned within the area of this mapping, there would be a single pixel or small collection of pixels that were much higher intensity than the rest.

Before taking any measurements with the functionalised AFM probe, a control experiment was carried out with an untreated probe (Figure 8.10). Chemical

mappings were recorded with this probe both in contact with the p-ATP monolayer and slightly retracted, each at a rate of 3 accumulations of 10s per pixel. This extended exposure time was required to detect the unenhanced Raman scattering that was expected from these measurements. Consequently, none of the spectra showed any sign of TERS.

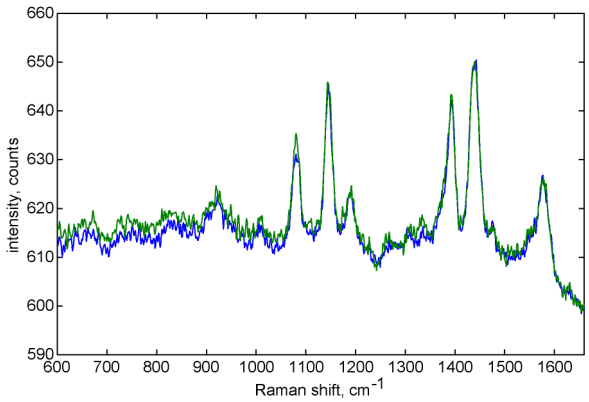

Figure 8.10: Averaged control spectra of a p-ATP monolayer on the silver substrate with an untreated AFM probe retracted (green) and in contact (blue) with the surface.

In contrast, TERS activity was observed in chemical mappings of the functionalised AFM probes (Figure 8.11). Most notably, these mappings contained a bright pixel, suggesting the alignment of the AFM probe with the laser beam at that position. However, from analysing the spectrum of this pixel, it could be seen that it varied from the rest of the mapping in more ways than just intensity. The Raman bands in this single spectrum are slightly shifted in frequency from their positions in the unenhanced Raman spectrum of p-ATP. The spectrum of the high intensity pixel also consists of different enhancements for different bands and contains extra bands that are not present in the spectra of the rest of the mapping. These aspects of the spectrum are consistent with those associated with SERS and TERS [101, 103, 104], which arise from the variation in the selection rules of conventional Raman spectroscopy [102, 105]. Therefore the combination of these spectral features with the obvious increase in the signal provides evidence for TERS and the ability of AFM probes functionalised by DEP to activate the effect.

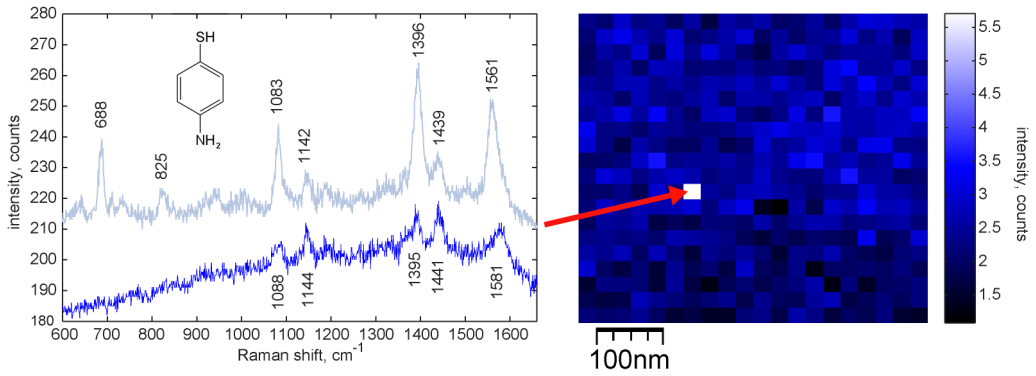

Figure 8.11: Spectra and mapping of a functionalised AFM probe across a p-ATP monolayer. TERS is evident in the upper trace, recorded at the corresponding position in the mapping (lower trace is the unenhanced Raman spectrum, which was recorded at all other positions).

8.4 Conclusions

The potential of DEP to functionalise AFM probes for TERS studies has been investigated. These probes were developed within a conductive AFM setup consisting of a specially-designed cantilever holder and a sample mount with electrical contacts connected in a circuit with a frequency generator. A voltage was applied to this system to generate DEP forces between the tip of an iridium-coated conductive AFM probe and a freshly-cleaved piece of graphite. Force spectroscopy was initially used to determine the success of this system. Force curves recorded before and after applying a voltage to the system indicated that there was an accumulation of nanoparticles on the AFM tip. This was consistent with changes in imaging parameters such as the deflection of the cantilever, the vertical position of the tip and the spring constant of the cantilever. When high voltages and frequencies were applied to the system, these factors suggested that a large amount of material had been deposited on the tip, which made it difficult to image with following experiments. At lower voltages and frequencies this was possible, revealing nanoparticle clusters on the graphite surface as well as on the AFM probe. The position of these depositions was consistent with the location of the tip apex at the time of applying a voltage to the system, suggesting the trapping and growth of material between the tip and the graphite surface by DEP. It was found that applying a frequency of 1MHz and a voltage of 10Vpp over a period of 30-120s provided suitable results for this application.

Whilst AFM measurements indicated that the probes had been functionalised by DEP, they were further investigated both physically and chemically with SEM. SEM images revealed fractal-like structures arising from DLA on many of the AFM probes. Some of them also exhibited wire-like structures that are typical of DEP growth. Most notably, two of the probes had a significant amount of material deposited on the tip apex. EDX analysis confirmed that this growth was a cluster of gold nanoparticles that could potentially activate TERS. These probes were assessed for TERS with the combined AFM-Raman system. Chemical mappings were recorded by raster scanning the tip across the laser beam focused on a monolayer of p-ATP. At a certain point in these mappings the tip apex and laser were aligned to successfully activate TERS.

Chapter 9

Summary and outlook

Discussions of all the main results of the thesis are given here along with suggestions for the future directions of the research.

9.1 Summary of findings

The main focus of this thesis has been the development of various Raman spectroscopy methods for investigating supported lipid bilayers (SLBs) and microdomains. The ability to manipulate and modify the makeup and environment of these lipid structures to create a biologically relevant model of a cell membrane has made SLBs a major area of scientific research. They have now been studied with a wide variety of microscopy and spectroscopy techniques. However, Raman spectroscopy is one technique that offers a full exploration of the physical and chemical properties of SLBs, which are still poorly understood [5].

Throughout the work described in this thesis, Raman spectroscopy has been used in numerous forms. This began with a non-resonant Raman spectroscopy setup based on an inverted microscope, developed and characterised for studying SLBs. The system then progressed into a confocal Raman microspectroscopy (RMS) setup with integrated atomic force microscope (AFM). Finally, scattering enhancing techniques surface-enhanced Raman spectroscopy (SERS) and tip-enhanced Raman spectroscopy (TERS) were explored to provide the sensitivity required to detect

SLBs and image microdomains. This work has demonstrated the potential of Raman spectroscopy methods for non-invasive physiochemical analysis of lipid membranes. In a wider sense, it will provide scientists with a better understanding of membrane function and aid investigation into important fields of medical research such as cell toxicology and drug delivery.

The starting point for all the work in this thesis is the experimental setup described in Chapter 5. The setup began as a conventional Raman spectroscopy system based on a continuous wave laser, inverted microscope and Czerny-Turner spectrometer. This system was built in-house and continually developed to optimise what could be achieved from the instrumentation with the aim of detecting and studying SLBs. A key step in this development was the integration of an AFM, allowing simultaneous topographical, mechanical and chemical measurements. The setup was characterised in terms of its sensitivity and spatial resolution capabilities, which led to the inclusion of a confocal system that improved both the axial and lateral resolution. The end result of this progression was an RMS setup with integrated AFM capable of performing high resolution SERS mapping and TERS.

Firstly, this setup was investigated for its ability to study SLBs without the assistance of any scattering enhancing techniques. In Chapter 6, a variety of substrates were assessed for their suitability for combined AFM and Raman spectroscopy of SLBs. From measurements of their Raman scattering and roughness, it was determined that sapphire was the most appropriate. The effect of laser power and exposure time on the structure of SLBs was then considered. Statistical analysis of Raman spectra recorded from a lipid film sample under a range of conditions revealed that only prolonged exposure to a high laser power had any effect on the Raman spectrum of lipids. A variety of SLBs were created and then imaged and analysed with AFM. This included single and mixed SLBs of dipalmitoylphosphatidylcholine (DPPC) and dioleoylphosphatidylcholine (DOPC), all of which contained microdomains. The Raman scattering of DPPC and DOPC was measured from multilayered structures of the lipids, identifying and assigning Raman bands. Following the assessment of materials to support lipid structures, a single SLB of DPPC was successfully deposited onto a sapphire substrate and imaged with AFM. However, the RMS setup was not sensitive enough to detect the Raman scattering of this SLB.

As a consequence of these findings, focus turned towards using SERS to investigate SLBs in Chapter 7. Silver nanosphere lithography (NSL) substrates constructed from 384 and 1002nm polystyrene spheres were developed and characterised for this purpose. These substrates were assessed for the distribution and magnitude of electric field enhancement that they could provide, using the combined AFM-Raman system to directly correlate physical and chemical information. SERS spectra and mappings of rhodamine 6G (R6G) and p-aminothiophenol (p-ATP) monolayers revealed the structure and variation in enhancement of the 1002nm substrates. Similarly, uniform enhancement was detected across the 384nm substrates. An enhancement factor common for this type of SERS substrate was calculated and FEM models were constructed to support this and the experiments. Arachidic acid (AA) lipid bilayers were then deposited onto the NSL substrates. Firstly, the Raman and SERS spectra of AA were compared in order to assign its SERS bands, which are not well established. Then SERS mappings of AA bilayers were recorded across the substrates, demonstrating their suitability for label-free imaging of lipid microdomains. Following on from the work discussed in the chapter before, an NSL substrate was constructed on sapphire and a single SLB of DPPC was successfully formed on it. However, it was not possible to detect the Raman scattering of this structure.

Chapter 8 of this thesis described the development of functionalised AFM probes for TERS. These probes were created within a conductive AFM setup, in which dielectrophoresis (DEP) was generated between the tip of a conductive AFM probe and a piece of graphite. Both force spectroscopy measurements and changes in imaging parameters indicated that nanoparticles were accumulating on the AFM tip. When high voltages and frequencies were applied to the system it appeared that a large amount of material had been deposited on the tip, whilst at lower voltages and frequencies images revealed nanoparticle clusters forming on the graphite surface as well as on the AFM probe. The probes were further investigated with scanning electron microscopy (SEM), which revealed structures arising from diffusion-limited aggregation (DLA), typical DEP growth of wire-like structures and a significant amount of material located on the tip apex of some probes. Energy-dispersive x-ray spectroscopy (EDX) analysis confirmed that this growth was a cluster of gold nanoparticles that could potentially activate TERS. This was realised when the

probes were placed into the combined AFM-Raman system and scanned across a monolayer of p-ATP. TERS was observed at one point in these mappings when the tip apex and laser were aligned.

9.2 Suggestions for further work

The work described in this thesis has begun to explore the use of Raman spectroscopy methods for studying SLBs. However, there is still further work required to realise the full potential of these techniques.

Despite the extensive development of the experimental setup used throughout this work, it could be further improved with optical fibres. Whilst most of the system could remain the same, these thin flexible fibres could be used to guide the light from the microscope into the spectrometer. This configuration would be much more stable than the setup described in this thesis, which required continuous alignment. A system with greater stability will result in better overall performance. Optical fibres would ensure a consistency in the signal intensity of measurements taken over long periods of time, enabling the collection of larger databases. In addition, the core of optical fibres acts as a pinhole, easing alignment by eliminating the need for a conventional confocal system.

Imaging SLBs with SERS has proved challenging, as within the scope of this work it was not possible to detect these nanoscale structures. Many steps were made towards achieving this, culminating in a DPPC bilayer supported on a sapphire-based SERS substrate. The presence of this SLB was confirmed by AFM; however, it was not possible to detect it with the Raman spectroscopy system. The ability to produce a chemical mapping of a bilayer of AA with good signal-to-noise ratio spectra suggests that this is achievable. Therefore, given more time and the fact that the sensitivity of the setup should increase with the introduction of optical fibres, it should be possible to detect a phospholipid SLB and image its microdomains with SERS.

The potential of DEP to create TERS-active functionalised AFM probes has been demonstrated in the final experimental chapter of this thesis. However, these results require further work to tune and regulate the technique. This includes being able to

determine growth rate, branching and thickness of TERS nanostructures by controlling the applied voltage and frequency, exposure time to DEP and nanoparticle size and concentration. In addition, the simultaneous growth of material on the surface underneath the tip apex that was observed during this work warrants further investigation. This technique could be developed to directly 'draw' two-dimensional (2D) and three-dimensional (3D) nanostructures to produce substrates for SERS.

Bibliography

[1] S. J. Singer and G. L. Nicolson, **The Fluid Mosaic Model of the Structure of Cell Membranes**, *Science* **1972**, *175*, 720-731.

[2] M. Edidin, **Lipid microdomains in cell surface membranes**, *Curr. Opin. Struc. Biol.* **1997**, *7* (4), 528-532.

[3] K. Simons and E. Ikonen, **Functional rafts in cell membranes**, *Nature* **1997**, *387*, 569-572.

[4] D. M. Engelman, **Membranes are more mosaic than fluid**, *Nature* **2005**, *438*, 578-580.

[5] S. Munro, **Lipid Rafts: Elusive or Illusive?** *Cell* **2003**, *115*, 377-388.

[6] K. El Kirat, S. Morandat and Y. F. Dufrêne, **Nanoscale analysis of supported lipid bilayers using atomic force microscopy**, *Biochim. et Biophys. Acta* **2010**, *1798*, 750-765.

[7] H. Schönherr, J. M. Johnson, P. Lenz, C. W. Frank and S. G. Boxer, **Vesicle Adsorption and Lipid Bilayer Formation on Glass Studied by Atomic Force Microscopy**, *Langmuir* **2004**, *20* (26), 11600-11606.

[8] S. S. Hui, R. Viswanathan, J. A. Zasadzinski and J. N. Israelachvili, **The Structure and Stability of Phospholipid Bilayers by Atomic Force Microscopy**, *Biophys. J.* **1995**, *68* (1), 171-178.

[9] S. Steltenkamp, M. M. Muller, M. Deserno, C. Hennesthal, C. Steinem and A. Janshoff, **Mechanical Properties of Pore-Spanning Lipid Bilayers Probed by Atomic Force Microscopy**, *Biophys. J.* **2006**, *91*, 217-226.

[10] D. Norouzi, M. M. Müller and M. Deserno, **How to determine local elastic properties of lipid bilayer membranes from atomic-force-microscope measurements: A theoretical analysis**, *Phys. Rev. E* **2006**, *74*, 061914.

[11] J. Schneider, Y. F. Dufrêne, W. R. Barger Jr. and G. U. Lee, **Atomic Force Microscope Image Contrast Mechanisms on Supported Lipid Bilayers**, *Biophys. J.* 2000, *79* (2), 1107-1118.

[12] L. J. C. Jeuken, **AFM Study on the Electric-Field Effects on Supported Bilayer Lipid Membranes**, *Biophys. J.* **2008**, *94* (12), 4711-4717.

[13] S. Kumano, M. Murakoshi, K. Iida, H. Hamana and H. Wada, **Atomic force microscopy imaging of the structure of the motor protein prestin reconstituted into an artificial lipid bilayer**, *FEBS Lett.* **2010**, *584*, 2872-2876.

[14] F. Dekkiche, M. C. Corneci, A.-M. Trunfio-Sfarghiu, B. Munteanu, Y. Berthier, W. Kaabar and J.-P. Rieu, **Stability and tribological performances of fluid phospholipid bilayers: Effect of buffer and ions**, *Coll. Surf. B* **2010**, *80* (2), 232-239.

[15] M.-C. Giocondi, D. Yamamoto, E. Lesniewska, P.-E. Milhiet, T. Ando and C. Le Grimellec, **Surface topography of membrane domains**, *Biochim. et Biophys. Acta* **2010**, *1798*, 703-718.

[16] D. K. Lee, K. W. Seo and Y. S. Kang, **Photoinduced electron transfer of chlorophyll in lipid bilayer system**, *Proc. Indian Acad. Sci.* (*Chem. Sci.*) **2002**, *114* (6), 533-538.

[17] I. Ruspantini, M. Diociaiuti, R. Ippoliti, E. Lendaro, M. C. Gaudiano, M. Cianfriglia, P. Chistolini, G. Arancia and A. Molinari, **Immunogold localisation of P-glycoprotein in supported lipid bilayers by transmission electron microscopy and atomic force microscopy**, *Histochem. J.* **2001**, *33* (5), 305-309.

[18] C. M. Hebling, C. R. Morgan, D. W. Stafford, J. W. Jorgenson, K. D. Rand and J. R. Engen, **Conformational Analysis of Membrane Proteins in Phospholipid Bilayer Nanodiscs by Hydrogen Exchange Mass Spectrometry**, *Anal. Chem.* **2010**, *82* (13), 5415-5419.

[19] A. Gunnarsson, F. Kollmer, S. Sohn, F. Hook and P. Sjovall, **Spatial-Resolution Limits in Mass Spectrometry Imaging of Supported Lipid Bilayers and Individual Lipid Vesicles**, *Anal. Chem.* **2010**, *82* (6), 2426-2433.

[20] D. Lee, K. F. A. Walter, A.-K. Brockner, C. Hilty, S. Becker and C. Griesinger, **Bilayer in Small Bicelles Revealed by Lipid-Protein Interactions Using NMR Spectroscopy**, *J. Am. Chem. Soc.* **2008**, *130* (42), 13822-13823.

[21] N. Kučerka, J. F. Nagle, J. N. Sachs, S. E. Feller, J. Pencer, A. Jackson and J. Katsaras, **Lipid Bilayer Structure Determined by the Simultaneous Analysis of Neutron and X-Ray Scattering Data**, *Biophys. J.* **2008**, *95* (5), 2356-2367.

[22] J. Yguerabide and L. Stryer, **Fluorescence Spectroscopy of an Oriented Model Membrane**, *Proc. Nat. Acad. Sci. USA* **1971**, *68* (6), 1217-1221.

[23] F. A. Heberle, J. T. Buboltz, D. Stringer and G. W. Feigenson, **Fluorescence methods to detect phase boundaries in lipid bilayer mixtures**, *Biochim. et Biophys. Acta.* **2005**, *1746* (3), 186-192.

[24] V. Tiriveedhi and P. A. Butko, **Fluorescence Spectroscopy Study on the Interactions of the TAT-PTD Peptide with Model Lipid Membranes**, *Biochem.* **2007**, *46*, 3888-3895.

[25] M. Przybyło, A. Olżyńska, S. Han, A. Ożyhar and M. Langner, **A fluorescence method for determining transport of charged compounds across lipid bilayer**, *Biophys. Chem.* **2007**, *129* (2-3), 120-125.

[26] A. E. McKiernan, T. V. Ratto and M. L. Longo, **Domain Growth, Shapes, and Topology in Cationic Lipid Bilayers on Mica by Fluorescence and Atomic Force Microscopy**, *Biophys. J.* **2000**, *79*, 2605-2615.

[27] J. R. Ferraro and K. Nakamoto, **Introductory Raman Spectroscopy**, *Academic Press Ltd* **1994**.

[28] R. L. McCreery, **Raman Spectroscopy for Chemical Analysis**, *Wiley-Interscience* **2000**.

[29] G. F. Bailey and R. J. Horvat, **Raman spectroscopic analysis of the cis/trans isomer composition of edible vegetable oils**, *J. Am. Oil Chem. Soc.* **1972**, *49*, 494-498.

[30] H. Sadeghi-Jorabchi, R. H. Wilson, P. S. Belton, J. D. Edwards-Webb, D. T. Coxon, **Quantitative analysis of oils and fats by Fourier transform Raman spectroscopy**, *Spectrochim. Acta A* **1991**, *47*, 1449-1458.

[31] B. Chmielarz, K. Bajdor, A. Labudzinska and Z. Klukowska-Majewska, **Studies on the double bond positional isomerisation process in linseed oil by UV, IR and Raman spectroscopy**, *J. Mol. Struct.* **1995**, *348*, 313-316.

[32] J. R. Beattie, S. E. J. Bell and B. W. Moss, **A critical evaluation of Raman spectroscopy for the analysis of lipids: Fatty acid methyl esters**, *Lipids* **2000**, *708*, 407-419.

[33] V. Baeten, **Raman spectroscopy in lipid analysis**, *Lipid Technol.* **2010**, *22* (2), 36-38.

[34] R. J. Meier, A. Csisza and E. Klumpp, **On the Interpretation of the 1100cm^{-1} Raman Band in Phospholipids and Other Alkyl-Containing Molecular Entities**, *J. Phys. Chem. B* **2006**, *110*, 5842-5844.

[35] J. D. Guo and T. W. Zerda, **Raman Study on Effects of High Pressure on the Structure of DPPC-Cholesterol Multilamellar Vesicles**, *J. Phys. Chem. B* **1997**, *101*, 5490-5496.

[36] M. S. Maier, D. L. A. de Faria, M. A. Boschín and S. D. Parera, **Characterisation of reference lipids and their degradation products by Raman spectroscopy, nuclear magnetic resonance and gas chromatography-mass spectrometry**, *ARKIVOC* **2005**, *12*, 311-318.

[37] E. E. Lawson, A. N. C. Anigbogu, A. C. Williams, B. W. Barry and H. G. M. Edwards, **Thermally induced molecular disorder in human stratum corneum lipids compared with a model phospholipid system; FT-Raman spectroscopy**, *Spectrochim. Acta A* **1998**, *54*, 543–558.

[38] D. P. Cherney, J. C. Conboy and J. M. Harris, **Optical-Trapping Raman Microscopy Detection of Single Unilamellar Lipid Vesicles**, *Anal. Chem.* **2003**, *75*, 6621-6628.

[39] D. P. Cherney, G. A. Myers, R. A. Horton and J. M. Harris, **Optically trapping confocal Raman microscopy of individual lipid vesicles: Kinetics of phospholipase A(2)-catalyzed hydrolysis of phospholipids in the membrane bilayer**, *Anal. Chem.* **2006**, *78* (19), 6928-6935.

[40] M. A. Kiselev, S. Wartewig, M. Janich, P. Lesieur, A. M. Kiselev, M. Ollivon and R. Neubert, **Does sucrose influence the properties of DMPC vesicles?** *Chem. Phys. Lipids* **2003**, *123*, 31-44.

[41] M. J. L. de Lange, M. Bonn and M. Muller, **Direct measurement of phase coexistence in DPPC/cholesterol vesicles using Raman spectroscopy**, *Chem. Phys. Lipids* **2007**, *146*, 76-84.

[42] C. S. Sweetenham and I. Notingher, **Raman spectroscopy methods for detecting and imaging supported lipid bilayers**, *Spectroscopy* **2010**, *24* (1-2), 113-117.

[43] A. Percot and M. Lafleur, **Direct Observation of Domains in Model Stratum Corneum Lipid Mixtures by Raman Microspectroscopy**, *Biophys. J.* **2001**, *81*, 2144-2153.

[44] C. Lee and C. D. Bain, **Raman spectra of planar supported lipid bilayers**, *Biochim. et Biophys. Acta* **2005**, *1711*, 59-71.

[45] C. B. Fox, R. H. Uibel and J. M. Harris, **Detecting Phase Transitions in Phosphatidylcholine Vesicles by Raman Microscopy and Self-Modelling Curve Resolution**, *J. Phys. Chem. B* **2007**, *111*, 11428-11436.

[46] C. B. Fox, R. A. Horton and J. M. Harris, **Detection of Drug-Membrane Interactions in Individual Phospholipid Vesicles by Confocal Raman Microscopy**, *Anal. Chem.* **2004**, *78*, 4918-4924.

[47] N. V. Surovtsev, E. S. Salnikov, V. K. Malinovsky, L. L. Sveshnikova and S. A. Dzuba, **On the low-temperature onset of molecular flexibility in lipid bilayers seen by Raman scattering**, *J. Phys. Chem. B* **2008**, *112* (39), 12361-12365.

[48] A. Downes, R. Mouras and A. Elfick, **A versatile CARS microscope for biological imaging**, *J. Raman Spectrosc.* **2009**, *40*, 757-762.

[49] L. Li, H. Wang and J.-X. Cheng, **Quantitative Coherent Anti-Stokes Raman Scattering Imaging of Lipid Distribution in Coexisting Domains**, *Biophys. J.* **2005**, *89*, 3480-3490.

[50] L. Li and J.-X. Cheng, **Label-Free Coherent Anti-Stokes Raman Scattering Imaging of Coexisting Lipid Domains in Single Bilayers**, *J. Phys. Chem. B* **2008**, *112* (6), 1576-1579.

[51] J.-X. Cheng, S. Pautot, D. A. Weitz and X. S. Xie, **Ordering of water molecules between phospholipid bilayers visualized by coherent anti-Stokes Raman scattering microscopy**, *PNAS* **2003**, *100*, 9826-9830.

[52] E. O. Potma and X. S. Xie, **Direct Visualization of Lipid Phase Segregation in Single Lipid Bilayers with Coherent Anti-Stokes Raman Scattering Microscopy**, *Chem. Phys. Chem.* **2005**, *6*, 77-79.

[53] G. W. H. Wurpel, J. M. Schins and M. Müller, **Direct Measurement of Chain Order in Single Phospholipid Mono- and Bilayers with Multiplex CARS**, *J. Phys. Chem. B* **2004**, *108*, 3400-3403.

[54] M. Fleischmann, P. J. Hendra and A. J. McQuillan, **Raman spectra of pyridine adsorbed at a silver electrode**, *Chem. Phys. Lett.* **1974**, *26*, 163-166.

[55] D. L. Jeanmaire and R. P. Van Duyne, **Surface Raman electrochemistry part I. Heterocyclic, aromatic, and aliphatic amines adsorbed on the anodized silver electrode**, *J. Electroanal. Chem.* **1977**, *84*, 1-20.

[56] C. W. Meuse, G. Niaura, M. L. Lewis and A. L. Plant, **Assessing the Molecular Structure of Alkanethiol Monolayers in Hybrid Bilayer Membranes with Vibrational Spectroscopies**, *Langmuir* **1998**, *14*, 1604-1611.

[57] C. L. Leverette and R. A. Dluhy, **Vibrational characterization of a planar-supported model bilayer system utilizing surface-enhanced Raman scattering (SERS) and infrared reflection–absorption spectroscopy (IRRAS)**, *Coll. Surf. A* **2004**, *243*, 157-167.

[58] P. Krysinski, E. Zebrowska, B. Pałys and Z. Łotowski, **Spectroscopic and Electrochemical Studies of Bilayer Lipid Membranes Tethered to the Surface of Gold**, *J. Electrochem. Soc.* **2002**, *149* (6), 189-194.

[59] M. K. Weldon, V. R. Zhelyaskov and M. D. Morris, **Surface-Enhanced Raman Spectroscopy of Lipids on Silver Microprobes**, *Appl. Spectrosc.* **1998**, *52*, 265-269.

[60] J. Kundu, C. S. Levin and N. J. Halas, **Real-time monitoring of lipid transfer between vesicles and hybrid bilayers on Au nanoshells using surface enhanced Raman scattering (SERS)**, *Nanoscale* **2009**, *1*, 114-117.

[61] J. Hrabakova, K. Ataka, J. Heberle, P. Hildebrandt and D. H. Murgida, **Long distance electron transfer in cytochrome c oxidase immobilised on electrodes: A surface enhanced resonance Raman spectroscopic study**, *Phys. Chem. Chem. Phys.* **2006**, *8*, 759-766.

[62] C. Heywang, M. Saint-Pierre Chazalet, M. Masson and J. Bolard, **Orientation of Anthracyclines in Lipid Monolayers and Planar Asymmetrical Bilayers: A Surface-Enhanced Resonance Raman Scattering Study**, *Biophys. J.* **1998**, *75*, 2368-2381.

[63] M. Saint-Pierre Chazalet, M. Masson, C. Bousquet, G. Bolbach, Y. Ridente and J. Bolard, **Surface-enhanced Raman scattering studies of lipid planar bilayers in water**, *Thin Solid Films* **1994**, *244* (1-2), 852-856.

[64] C. S. Sweetenham and I. Notingher, **Combined AFM-Raman mapping of electric field enhancement and SERS hot-spots for nanosphere lithography substrates**, *J. Nanophoton.* **2011**, *5*, 059504.

[65] E. C. le Ru and P. G. Etchegoin, **Vibrational pumping and heating under SERS conditions: fact or myth?** *Faraday Discuss.* **2006**, *132*, 63-75.

[66] R. C. Maher, L. F. Cohen, J. C. Gallop, E. C. le Ru and P. G. Etchegoin, **Temperature-Dependent Anti-Stokes/Stokes Ratios under Surface-Enhanced Raman Scattering Conditions**, *J. Phys. Chem. B* **2006**, *110*, 6797-6803.

[67] R. C Maher, M. Dalley, E. C. le Ru, L. F. Cohen, P. G. Etchegoin, H. Hartigan, R. J. C. Brown and M. J. T. Milton, **Physics of single molecule fluctuations in surface enhanced Raman spectroscopy active liquids**, *J. Chem. Phys.* **2004**, *121* (18), 8901-8910.

[68] K. W. Kho, Z. X. Shen, Z. Lei, F. Watt, K. C. Soo and M. Olivo, **Investigation into a Surface Plasmon Related Heating Effect in Surface Enhanced Raman Spectroscopy**, *Anal. Chem.* **2007**, *79*, 8870-8882.

[69] R. M. Stöckle, Y. D. Suh, V. Deckert and R. Zenobi, **Nanoscale chemical analysis by tip-enhanced Raman spectroscopy**, *Chem. Phys. Lett.* **2000**, *318*, 131–136.

[70] I. Notingher and A. Elfick, **Effect of Sample and Substrate Electric Properties on the Electric Field Enhancement at the Apex of SPM Nanotips**, *J. Phys. Chem. B* **2005**, *109*, 15699-15706.

[71] T. Schmid, A. Sebesta, J. Stadler, L. Opilik, R. M. Balabin and R. Zenobi, **Tip-enhanced Raman spectroscopy and related techniques in studies of biological materials**, *Proc. of SPIE* **2010**, *7586*, 758603.

[72] A. P. D. Elfick, A. R. Downes and R. Mouras, **Development of tip-enhanced optical spectroscopy for biological applications: a review**, *Anal. Bioanal. Chem.* **2010**, *396*, 45-52.

[73] B. Alberts, A. Johnson, J. Lewis, M. Raff, K. Roberts and P. Walter, **Molecular Biology of the Cell**, *Garland Science* **2002**.

[74] R. Koynova and M. Caffrey, **Phases and phase transitions of the phosphatidylcholines**, *Biochim. et Biophys. Acta* **1998**, *1376*, 91-145.

[75] R. Elliott, K. Katsov, M. Schick and I. Szleifer, **Phase Separation of Saturated and Mono-unsaturated Lipids as determined from a Microscopic Model**, *J. Chem. Phys.* **2005**, *122*, 044904.

[76] L. Rajendran and K. Simons, **Lipid rafts and membrane dynamics**, *J. Cell Sci.* **2005**, *118*, 1099-1102.

[77] E. Sackmann, **Supported Membranes: Scientific and Practical Applications**, *Science* **1996**, *271* (5245), 43-48.

[78] P. E. Milhiet, V. Vié, M.-C. Giocondi and C. Le Grimellec, **AFM Characterisation of Model Rafts and Supported Bilayers**, *Single Mol. 2* **2001**, *2*, 109-112.

[79] M.-C. Giocondi, V. Vie, E. Lesniewska, P.-E. Milhiet, M. Zinke-Allmang and C. Le Grimellec, **Phase Topology and Growth of Single Domains in Lipid Bilayers**, *Langmuir* **2001**, *17*, 1653-1659.

[80] Z. V. Leonenko, E. Finot, H. Ma, T. E. S. Dahms and D. T. Cramb, **Investigation of Temperature-Induced Phase Transitions in DOPC and DPPC Phospholipid Bilayers Using Temperature-Controlled Scanning Force Microscopy**, *Biophys. J.* **2004**, *86*, 3783-3793.

[81] M. L. Schmidt, L. Ziani, M. Boudreau and J. H. Davis, **Phase equilibria in DOPC/DPPC: Conversion from gel to subgel in two component mixtures**, *J. Chem. Phys.* **2009**, *131*, 175103.

[82] M. Kinoshita, K. Ito and S. Kato, **Kinetics for the subgel phase formation in DPPC/DOPC mixed bilayers**, *Chem. Phys. Lipids* **2010**, *163*, 712-719.

[83] L. D. Mayer, M. J. Hope and P. R. Cullis, **Vesicles of variable sizes produced by a rapid extrusion procedure**, *Biochim. et Biophys. Acta* **1986**, *858*, 161-168.

[84] R. C. MacDonald, R. I. MacDonald, B. P. Menco, K. Takeshita, N. K. Subbarao and L. R. Hu, **Small-volume extrusion apparatus for preparation of large, unilamellar vesicles**, *Biochim. et Biophys. Acta* **1991**, *1061*, 297-303.

[85] H. Egawa and K. Furusawa, **Liposome Adhesion on Mica Surface Studied by Atomic Force Microscopy**, *Langmuir* **1999**, *15*, 1660-1666.

[86] I. Langmuir, **The constitution and fundamental properties of solids and liquids. II. Liquids**, *J. Am. Chem. Soc.* **1917**, *39*, 1848-1906.

[87] K. B. Blodgett, **Films built by depositing successive monomolecular layers on a solid surface**, *J. Am. Chem. Soc.* **1935**, *57* (1), 1007-1022.

[88] G. Binnig and H. Rohrer, **Scanning tunnelling microscopy**, *Helv. Phys. Acta* **1982**, *55* (6), 726-735.

[89] R. Wiesendanger, **Scanning Probe Microscopy and Spectroscopy: Methods and Applications**, *Cambridge University Press* **1994**.

[90] G. Binnig, C. F. Quate and C. Gerber, **Atomic force microscope**, *Phys. Rev. Lett.* **1986**, *56* (9) 930-933.

[91] Q. Zhong, D. Inniss, K. Kjoller and V. B. Elings, **Fractured polymer silica fiber surface studied by tapping mode atomic-force microscopy**, *Surf. Sci.* **1993**, *290* (1-2), 688-692.

[92] S. Basak and A. Ramana, **Dynamics of tapping mode atomic force microscopy in liquids: Theory and experiments**, *Appl. Phys. Lett.* **2007**, *91*, 064107.

[93] F. Kuhner, L. T. Costa, P. M. Bisch, S. Thalhammer, W. M. Heckl and H. E. Gaub, **LexA-DNA Bond Strength by Single Molecule Force Spectroscopy**, *Biophys. J.* **2004**, *87*, 2683-2690.

[94] T. V. Ratto, K. C. Langry, R. E. Rudd, R. L. Balhorn, M. J. Allen and M. W. McElfresh, **Force Spectroscopy of the Double-Tethered Concanavalin-A Mannose Bond**, *Biophys. J.* **2004**, *86*, 2430-2437.

[95] R. Merkel, P. Nassoy, A. Leung, K. Ritchie and E. Evans, **Energy landscapes of receptor-ligand bonds explored with dynamic force spectroscopy**, *Nature* **1999**, *397*, 50-53.

[96] M. Benoit, D. Gabriel, G. Gerisch and H. E. Gaub, **Discrete interactions in cell adhesion measured by single-molecule force spectroscopy**, *Nat. Cell Biol.* **2000**, *2*, 313-317.

[97] M. Rief, J. Pascual, M. Saraste and H. E. Gaub, **Single Molecule Force Spectroscopy of Spectrin Repeats: Low Unfolding Forces in Helix Bundles**, *J. Mol. Biol.* **1999**, *286*, 553-561.

[98] M. Rief, F. Oesterhelt, B. Heymann and H. E. Gaub, **Single Molecule Force Spectroscopy on Polysaccharides by Atomic Force Microscopy**, *Science* **1997**, *275*, 1295-1297.

[99] C. V. Raman, **The Colour of the Sea**, *Nature* **1921**, *108*, 367.

[100] C. V. Raman and K. S. Krishnan, **A new type of secondary radiation**, *Nature* **1928**, *121*, 501-502.

[101] D. Maniu, V. Chis, M. Baia, F. Toderas and S. Astilean, **Density functional theory investigation of p-aminothiophenol molecules adsorbed on gold nanoparticles**, *J. Optoelectron. Adv. Mater.* **2007**, *9* (3), 733-736.

[102] M. Moskovits and J. S. Suh, **Surface Selection Rules for Surface-Enhanced Raman Spectroscopy: Calculations and Application to the Surface-Enhanced Raman Spectrum of Phthalazine on Silver**, *J. Phys. Chem.* **1984**, *88* (23), 5526-5530.

[103] T. Deckert-Gaudig, E. Rauls and V. Deckert, **Aromatic Amino Acid Monolayers Sandwiched between Gold and Silver: A Combined Tip-Enhanced Raman and Theoretical Approach**, *J. Phys. Chem. C* **2010**, *114*, 7412-7420.

[104] W. Zhang, T. Schmid, B. S. Yeo, and R. Zenobi, **Tip-enhanced Raman Spectroscopy Reveals Rich Nanoscale Adsorption Chemistry of 2-Mercaptopyridine on Ag**, *Isr. J. Chem.* **2007**, *47*, 177-184.

[105] S. Berweger and M. B. Raschke, **Polar phononmode selection rules in tip-enhanced Raman scattering**, *J. Raman Spectrosc.* **2009**, *40*, 1413-1419.

[106] J. J. Laserna, **Modern Techniques in Raman Spectroscopy**, *Wiley* **1996**.

[107] I. Notingher and L. L. Hench, **Raman microspectroscopy: a non-invasive tool for studies of individual living cells in vitro**, *Expert Rev. Med. Devic.* **2006**, *3* (2), 1-20.

[108] E. B. Hanlon, R. Manoharan, T.-W. Koo, K. E. Shafer, J. T. Motz, M. Fitzmaurice, J. R. Kramer, I. Itzkan, R. R. Dasari and M. S. Feld, **Prospects for in vivo Raman spectroscopy**, *Phys. Med. Biol.* **2000**, *45*, 1-59.

[109] M. G. Albrecht and J. A. Creighton, **Anomalously Intense Raman Spectra of Pyridine at a Silver Electrode**, *J. Am. Chem. Soc.* **1977**, *99* (15), 5215-5217.

[110] P. C. Lee and D. J. Meisel, **Adsorption and surface-enhanced Raman of dyes on silver and gold sols**, *Phys. Chem.* **1982**, *86*, 3391-3395.

[111] C. J. Murphy, T. K. Sau, A. M. Gole, C. J. Orendorff, J. Gao, L. Gou, S. E. Hunyadi and T. Li, **Anisotropic Metal Nanoparticles: Synthesis, Assembly, and Optical Applications**, *J. Phys. Chem. B* **2005**, *109*, 13857-13870.

[112] C. L. Haynes and R. P. Van Duyne, **Nanosphere Lithography: A Versatile Nanofabrication Tool for Studies of Size-Dependent Nanoparticle Optics**, *J. Phys. Chem. B* **2001**, *105*, 5599-5611.

[113] A. J. Haes, C. L. Haynes, A. D. McFarland, G. C. Schatz, R. P. Van Duyne and S. Zou, **Plasmonic Materials for Surface-Enhanced Sensing and Spectroscopy**, *MRS Bulletin* **2005**, *30*, 368-375.

[114] K. L. Kelly, E. Coronado, L. L. Zhao and G. C. Schatz, **The Optical Properties of Metal Nanoparticles: The Influence of Size, Shape, and Dielectric Environment**, *J. Phys. Chem. B* **2003**, *107*, 668-677.

[115] V. M. Shalaev and A. K. Sarychev, **Non-linear optics of random metal-dielectric films**, *Phys. Rev. B* **1998**, *57*, 13265-13288.

[116] M. Moskovits and D. H. Jeong, **Engineering nanostructures for giant optical fields**, *Chem. Phys. Lett.* **2004**, *397*, 91-95.

[117] C. Farcau and S. Astilean, **Mapping the SERS Efficiency and Hot-Spots Localization on Gold Film over Nanospheres Substrates**, *J. Phys. Chem. C* **2010**, *114*, 11717-11722.

[118] K. Kneipp, Y. Wang, H. Kneipp, I. Itzkan, R. R. Dasari and M. S. Feld, **Population pumping of excited vibrational states by spontaneous surface-enhanced Raman scattering**, *Phys. Rev. Lett.* **1996**, *76*, 2444-2447.

[119] S. Nie and S. R. Emory, **Probing Single Molecules and Single Nanoparticles by Surface-Enhanced Raman Scattering**, *Science* **1997**, *275* (5303), 1102-1106.

[120] K. Kneipp, Y. Wang, H. Kneipp, L. T. Perelman, I. Itzkan, R. R. Dasari and M. S. Feld, **Single molecule detection using surface-enhanced Raman scattering (SERS)**, *Phys. Rev. Lett.* **1997**, *78*, 1667-1670.

[121] K. Kneipp, H. Kneipp, P. Corio, S. D. M. Brown, K. Shafer, J. Motz, L. T. Perelman, E. B. Hanlon, A. Marucci, G. Dresselhaus and M. S. Dresselhaus, **Surface-Enhanced and Normal Stokes and Anti-Stokes Raman Spectroscopy of Single-Walled Carbon Nanotubes**, *Phys. Rev. Lett.* **2000**, *84* (15), 3470-3473.

[122] V. P. Safonov, V. M. Shalaev, V. A. Markel, Yu. E. Danilova, N. N. Lepeshkin, W. Kim, S. G. Rautian and R. L. Armstrong, **Spectral Dependence of Selective Photomodification in Fractal Aggregates of Colloidal Particles**, *Phys. Rev. Lett.* **1998**, *80* (5), 1102-1105.

[123] K. Kneipp, H. Kneipp and M. Moskovits, **Surface-Enhanced Raman Scattering: Physics and Applications**, *Springer-Verlag* **2006**.

[124] M. Moskovits, **Surface enhanced Raman spectroscopy: a brief retrospective**, *J. Raman Spectrosc.* **2005**, *36*, 485-496.

[125] A. Otto, I. Mrozek, H. Grabhorn and W. Akemann, **Surface enhanced Raman scattering**, *J. Phys. Condens. Matt.* **1992**, *4*, 1143-1212.

[126] P. Kambhampati, C. M. Child, M. C. Foster and A. Campion, **On the chemical mechanism of surface enhanced Raman scattering: Experiments and theory**, *J. Chem. Phys.* **1998**, *108* (12), 5013-5026.

[127] J. Wessel, **Surface-enhanced optical microscopy**, *J. Opt. Soc. Am. B* **1985**, *2*, 1538-1541.

[128] B. Pettinger, B. Ren, G. Picardi, R. Schuster and G. Ertl, **Nanoscale Probing of Adsorbed Species by Tip-Enhanced Raman Spectroscopy**, *Phys. Rev. Lett.* **2004**, *92* (9), 096101.

[129] B A Tozer, **The Calculation of Maximum Permissible Exposure Levels for Laser Radiation**, *J. Phys. E: Sci. Instrum.* **1979**, *12*, 922-924.

[130] E. Abbe, **Beitrage zur Theorie des Mikroskops und der Mikroskop ischen Wahrnehmung (Contributions to the theory of microscopes and microscopic perception)**, *Arch. Mikroskop. Anat.* **1873**, *9*, 413-468.

[131] N. Everall, J. Lapham, F. Adar, A. Whitley, E. Lee and S. Mamedov, **Optimizing Depth Resolution in Confocal Raman Microscopy: A Comparison of Metallurgical, Dry Corrected, and Oil Immersion Objectives**, *Appl. Spectrosc.* **2007**, *61* (3), 251-259.

[132] K. J. Baldwin and D. N. Batchelder, **Confocal Raman Microspectroscopy through a Planar Interface**, *Appl. Spectrosc.* **2001**, *55* (5), 517-524.

[133] P. J. Caspers, G. W. Lucassen, E. A. Carter, H. A. Bruining and G. J. Puppels, **In Vivo Confocal Raman Microspectroscopy of the Skin: Noninvasive Determination of Molecular Concentration Profiles**, *J. Invest. Dermatol.* **2001**, *116* (3), 434-442.

[134] R. Tabaksblat, R. J. Meier and B. J. Kip, **Confocal Raman Microspectroscopy: Theory and Application to Thin Polymer Samples**, *Appl. Spectrosc.* **1992**, *46* (1), 60-68.

[135] G. J. Puppels, F. F. M. De Mul, C. Otto, J. Greve, M. Robert-Nicoud, D. J. Arndt-Jovin and T. M. Jovin, **Studying single living cells and chromosomes by confocal Raman microspectroscopy**, *Nature* **1990**, *347*, 301-303.

[136] N. M. Sijtsema, C. Otto, G. M. J. Segers-Nolten, A. J. Verhoeven and J. Greve, **Resonance Raman Microspectroscopy of Myeloperoxidase and Cytochrome b_{558} in Human Neutrophilic Granulocytes**, *Biophys. J.* **1998**, *74*, 3250-3255.

[137] C. Matthaus, T. Chernenko, J. A. Newmark, C. M. Warner and M. Diem, **Label-Free Detection of Mitochondrial Distribution in Cells by Nonresonant Raman Microspectroscopy**, *Biophys. J.* **2007**, *93*, 668-673.

[138] K. P. J. Williams, G. D. Pitt, D. N. Batchelder and B. J. Kip, **Confocal Raman Microspectroscopy Using a Stigmatic Spectrograph and CCD Detector**, *Appl. Spectrosc.* **1994**, *48* (2), 232-235.

[139] E. T. Castellana and P. S. Cremer, **Solid supported lipid bilayers: From biophysical studies to sensor design**, *Surf. Sci. Rep.* **2006**, *61*, 429-444.

[140] J. Marra, **Controlled Deposition of Lipid Monolayers and Bilayers onto Mica and Direct Force Measurements between Galactolipid Bilayers in Aqueous Solutions**, *J. Coll. Int. Sci.* **1985**, *107* (2), 446-458.

[141] S. Singh and D. J. Keller, **Atomic force microscopy of supported planar membrane bilayers**, *Biophys. J.* **1991**, *60* (6), 1401-1410.

[142] F. Cuccureddu, S. Murphy, I. V. Shvets, M. Porcu, H. W. Zandbergen, N. S. Sidorov and S. I. Bozhko, **Surface morphology of c-plane sapphire (α-alumina) produced by high temperature anneal**, *Surf. Sci.* **2010**, *604*, 1294-1299.

[143] G. H. Golub and C. F. van Loan, **Matrix Computations**, *North Oxford Academic Publishing* **1983**.

[144] N. Uzunbajakava, A. Lenferink, Y. Kraan, B. Willekens, G. Vrensen, J. Greve and C. Otto, **Nonresonant Raman Imaging of Protein Distribution in Single Human Cells**, *Biopolymers* **2002**, *72* (1), 1-9.

[145] N. Uzunbajakava, A. Lenferink, Y. Kraan, E. Volokhina, G. Vrensen, J. Greve and C. Otto, **Nonresonant Confocal Raman Imaging of DNA and Protein Distribution in Apoptotic Cells**, *Biophys. J.* **2003**, *84*, 3968-3981.

[146] R. B. Cattell, **The Scree Test for the Number of Factors**, *Multivar. Behav. Res.* **1966**, *1* (2), 245-276.

[147] A. Ottova-Leitmannova, **Advances in Planar Lipid Bilayers and Liposomes**, *Academic Press* **2006**.

[148] F. D. Gunstone, J. L. Harwood and F. B. Padley, **The Lipid Handbook**, *Chapman & Hall* **1994**.

[149] T. Isono, T. Ikeda and T. Ogino, **Evolution of Supported Planar Lipid Bilayers on Step-Controlled Sapphire Surfaces**, *Langmuir* **2010**, *26* (12), 9607-9611.

[150] H. Ko, S. Singamaneni and V. V. Tsukruk, **Nanostructured Surfaces and Assemblies as SERS Media**, *Small* **2008**, *4* (10), 1576-1599.

[151] R. J. C. Brown and M. J. T. Milton, **Nanostructures and nanostructured substrates for surface-enhanced Raman scattering (SERS)**, *J. Raman Spectrosc.* **2008**, *39*, 1313-1326.

[152] J. Rybczynski, U. Ebels and M. Giersig, **Large-scale, 2D arrays of magnetic nanoparticles**, *Coll. Surf. A* **2003**, *219*, 1-6.

[153] L. Baia, M. Baia, J. Popp and S. Astilean, **Gold Films Deposited over Regular Arrays of Polystyrene Nanospheres as Highly Effective SERS Substrates from Visible to NIR**, *J. Phys. Chem. B* **2006**, *110* (47), 23982-23986.

[154] J. C. Hulteen, D. A. Treichel, M. T. Smith, M. L. Duval, T. R. Jensen and R. P. Van Duyne, **Nanosphere Lithography: Size-Tunable Silver Nanoparticle and Surface Cluster Arrays**, *J. Phys. Chem. B* **1999**, *103*, 3854-3863.

[155] J. P. Schmidt, S. E. Cross and S. K. Buratto, **Surface-enhanced Raman scattering from ordered Ag nanocluster arrays**, *J. Chem. Phys.* **2004**, *121* (21), 10657-10659.

[156] J. Zhao, L. Jensen, J. Sung, S. Zou, G. C. Schatz and R. P. Van Duyne, **Interaction of Plasmon and Molecular Resonances for Rhodamine 6G Adsorbed on Silver Nanoparticles**, *J. Am. Chem. Soc.* **2007**, *129*, 7647-7656.

[157] C. Farcau and S. Astilean, **Probing the unusual optical transmission of silver films deposited on two-dimensional regular arrays of polystyrene microspheres**, *J. Opt. A: Pure Appl. Opt.* **2007**, *9*, 345-349.

[158] E. C. Le Ru, E. Blackie, M. Meyer and P. G. Etchegoin, **Surface Enhanced Raman Scattering Enhancement Factors: A Comprehensive Study**, *J. Phys. Chem. C* **2007**, *111* (37), 13794-13803.

[159] J. C. Hulteen and R. P. Van Duyne, **Nanosphere lithography: A materials general fabrication process for periodic particle array surfaces**, *J. Vac. Sci. Technol. A* **1995**, *13*, 1553-1558.

[160] C. L. Haynes and R. P. Van Duyne, **Plasmon-Sampled Surface-Enhanced Raman Excitation Spectroscopy**, *J. Phys. Chem. B* **2003**, *107*, 7426-7433.

[161] N. Mohri, M. Inoue, Y. Arai and K Yoshikawa, **Kinetic Study on Monolayer Formation with 4-Aminobenzenethiol on a Gold Surface**, *Langmuir* **1995**, *11*, 1612-1616.

[162] G. C. Schatz, M. A. Young and R. P. Van Duyne, **Electromagnetic Mechanism of SERS**, *Top. Appl. Phys.* **2006**, *103*, 19-45.

[163] E. D. Palik, **Handbook of Optical Constants of Solids**, *Academic Press* **1998**.

[164] J. Jin, **The Finite Element Method in Electromagnetics**, *New York: Wiley* **2002**.

[165] T.-H. Lin, N. C. Linn, L. Tarajano, B. Jiang and P. Jiang, **Electrochemical SERS at Periodic Metallic Nanopyramid Arrays**, *J. Phys. Chem. C* **2009**, *113*, 1367-1372.

[166] A. J. Haes, S. Zou, G. C. Schatz and R. P. Van Duyne, **Nanoscale Optical Biosensor: Short Range Distance Dependence of the Localized Surface Plasmon Resonance of Noble Metal Nanoparticles**, *J. Phys. Chem. B* **2004**, *108*, 6961-6968.

[167] R. E. Oakes, J. Renwick Beattie, B. W. Moss and S. E. J. Bell, **DFT studies of long-chain FAMEs: theoretical justification for determining chain length and unsaturation from experimental Raman spectra**, *J. Mol. Struct.* **2003**, *626*, 27–45.

[168] Y. Roiter, M. Ornatska, A. R. Rammohan, J. Balakrishnan, D. R. Heine and S. Minko, **Interaction of Nanoparticles with Lipid Membrane**, *Nano Lett.* **2008**, *8* (3), 941-944.

[169] B.-S. Yeo, J. Stadler, T. Schmid, R. Zenobi and W. Zhang, **Tip-enhanced Raman Spectroscopy – Its status, challenges and future directions**, *Chem. Phys. Lett.* **2009**, *472*, 1-13.

[170] D. M. Eigler and E. K. Schweizer, **Positioning single atoms with a scanning tunnelling microscope**, *Nature* **1990**, *344*, 524-526.

[171] J. A. Theobald, N. S. Oxtoby, M. A. Phillips, N. R. Champness and P. H. Beton, **Controlling molecular deposition and layer structure with supramolecular surface assemblies**, *Nature* **2003**, *424*, 1029-1031.

[172] H. A. Pohl, **The motion and precipitation of suspensoids in divergent electric fields**, *J. Appl. Phys.* **1951**, *22* (7), 869-871.

[173] S. Fiedler, S. G. Shirley, T. Schnelle and G. Fuhr, **Dielectrophoretic Sorting of Particles and Cells in a Microsystem**, *Anal. Chem.* **1998**, *70* (9), 1909-1915.

[174] H. Morgan, M. P. Hughes and N. G. Green, **Separation of Submicron Bioparticles by Dielectrophoresis**, *Biophys. J.* **1999**, *77*, 516-525.

[175] J. Yang, Y. Huang, X.-B. Wang, F. F. Becker and P. R. C. Gascoyne, **Cell Separation on Microfabricated Electrodes Using Dielectrophoretic/ Gravitational Field-Flow Fractionation**, *Anal. Chem.* **1999**, *71* (5), 911-918.

[176] O. D. Velev and E. W. Kaler, **In Situ Assembly of Colloidal Particles into Miniaturized Biosensors**, *Langmuir* **1999**, *15* (11), 3693-3698.

[177] K. D. Hermanson, S. O. Lumsdon, J. P. Williams, E. W. Kaler and O. D. Velev, **Dielectrophoretic Assembly of Electrically Functional Microwires from Nanoparticle Suspensions**, *Science* **2001**, *294* (5544), 1082-1086.

[178] H. A. Pohl, **Dielectrophoresis: The Behavior of Neutral Matter in Nonuniform Electric Fields**, *Cambridge University Press* **1978**.

[179] T. B. Jones, **Electromechanics of Particles**, *Cambridge University Press* **1995**.

[180] H. Morgan and N. Green, **AC Electrokinetics: Colloids and Nanoparticles**, *Research Studies Press* **2001**.

[181] A. S. Bahaj and A. G. Bailey, **Dielectrophoresis of microscopic particles**, *J. Phys. D: Appl. Phys.* **1979**, *12* (10), L109-L112.

[182] T. A. Witten, Jr. and L. M. Sander, **Diffusion-Limited Aggregation, a Kinetic Critical Phenomenon**, *Phys. Rev. Lett.* **1981**, *47* (19), 1400-1403.

[183] N. Ranjan, H. Vinzelberg and M. Mertig, **Growing One-Dimensional Metallic Nanowires by Dielectrophoresis**, *Small* **2006**, *2* (12), 1490-1496.

[184] A. M. Sweetman, **Forces at the nanoscale: interactions in atomic force microscopy and dielectrophoresis**, *PhD Thesis* **2009**.

[185] P. Bahukudumbi, W. N. Everett, A. Beskok, M. A. Bevan, G. H. Hu, D. Lagoudas and Z. Ounaies, **Colloidal microstructures, transport, and impedance properties within interfacial microelectrodes**, *Appl. Phys. Lett.* **2007**, *90* (22), 224102.

[186] B. C. Gierhart, D. G. Howitt, S. J. Chen, R. L. Smith and S. D. Collins, **Frequency Dependence of Gold Nanoparticle Superassembly by Dielectrophoresis**, *Langmuir* **2007**, *23* (24), 12450-12456.

[187] W. Zhang, X. Cui, B.-S. Yeo, T. Schmid, C. Hafner and R. Zenobi, **Nanoscale Roughness on Metal Surfaces Can Increase Tip-Enhanced Raman Scattering by an Order of Magnitude**, *Nano Lett.* **2007**, *7* (5), 1401-1405.

List of figures

List of tables